

Nanosecond level time synchronization of distributed radio detectors

Master's thesis
by

Yan Seyffert

At the Department of Physics
Institute for Astroparticle Physics

Reviewer: Prof. Dr. Ralph Engel
Second reviewer: Prof. Dr. Tim Huege

Karlsruhe, 13.09.2023

This thesis has been accepted by the first reviewer of the master's thesis.

Karlsruhe, 13.09.2023

.....
(Prof. Dr. Ralph Engel)

I declare that I have developed and written the enclosed thesis completely by myself, and have not used any sources or means other than those specified. I have properly identified any directly quoted or paraphrased passages and have adhered to the current version of the KIT's regulations for ensuring good scientific practice.

Karlsruhe, 13.09.2023

.....
(Yan Seyffert)

Contents

1	Introduction	1
2	Cosmic ray air showers and radio interferometry	3
2.1	History of cosmic ray research	3
2.2	Cosmic ray energy spectrum	4
2.3	Structure of an Extensive Air Shower	5
2.3.1	Hadronic component	5
2.3.2	Electromagnetic component	5
2.3.3	Muonic component	6
2.3.4	Radio emissions from cosmic rays	6
2.4	Detection methods for cosmic rays	7
2.4.1	Surface detectors	8
2.4.2	Fluorescence detectors	9
2.4.3	Radio detectors	10
2.4.4	Radio interferometry	11
3	Synchronization of distributed detectors	15
3.1	Background on Global Navigation Satellite Systems	16
3.1.1	General information and functionality of GNSS	16
3.1.2	Examples of GNSS: GPS Navstar and Galileo	16
3.1.3	GPS time	17
3.1.4	Accuracy limitations of GNSS and their causes	18
3.1.5	Techniques to mitigate GNSS inaccuracies	18
3.2	The AERA beacon reference transmitter	20
4	Evaluation of the timing accuracy of RTK GNSS modules	23
4.1	Description on the used hardware	23
4.2	Evaluation of the GNSS boards	24
4.3	Relative time accuracy tests	26
4.3.1	Hardware setup	26
4.3.2	Software setup	28
4.3.3	Survey-in of base and measurement methodology	29
4.3.4	Time pulse measurement campaign results	31
4.4	Further discussion and discarded testing possibilities	35
5	Data analysis of the AERA Reference Beacon Transmitter	37
5.1	Description of the data and software	37
5.2	Analysis of the signal attenuation as a function of distance	38
5.2.1	Pre-processing in <i>Offline</i>	38
5.2.2	Station positions and distance calculation	39
5.2.3	Event spectra and average spectra	42
5.2.4	Amplitude plots	42

5.2.5	Fit methodologies	46
5.2.6	Observed angle dependence of the signal amplitudes	49
5.2.7	Temporal variability of the spectral index	51
5.3	Estimation of required RD beacon distance to array edge	52
5.4	Discussion and outlook on the beacon analysis	54
6	Summary	57
	Appendix	61
A	table of all time pulse measurement runs	61
B	all time pulse measurement plots	62
C	additional beacon analysis plots	69
	Acronyms	75
	Bibliography	79

List of Figures

2.1	Cosmic ray energy spectrum	4
2.2	Structure of an EAS	6
2.3	Visualization of geomagnetic and charge excess emissions from cosmic rays	7
2.4	Detector map of the Pierre Auger Observatory	8
2.5	Photo of a SD station at the Pierre Auger Observatory	9
2.6	AERA stations with LPDA and Butterfly antenna	10
2.7	AERA stations deployment map	10
2.8	The radio interferometric technique applied to a simulation of an extensive air shower	12
2.9	Interferometric reconstruction of an air shower axis and X_{\max}	13
2.10	Reconstruction resolution of X_{\max} shown for different time jitter scenarios	13
3.1	Examples of GNSS constellations	17
3.2	Schematic illustration of RTK	19
3.3	Photo of the Coihueco communications tower	21
3.4	Schematic of AERA and its radio beacon reference transmitter	21
4.1	The <i>simpleRTK2B Starter Kit LR</i> from ARDUSIMPLE	23
4.2	Screenshot of the <i>u-center</i> software	25
4.3	Photographs of the setup evaluating the GNSS boards	26
4.4	Location of the GNSS antennas	27
4.5	Pictures of the time-pulse measurement setup	27
4.6	Detailed pictures of the measurement setup	27
4.7	Screenshot of PICOSCOPE software displaying the pps signal of one of the ARDUSIMPLE boards	28
4.8	JUPYTER NOTEBOOK real-time visualization of the data acquisition displaying the latest pulses	29
4.9	An exemplary final plot of the obtained time measurement data	30
4.10	Time pulse measurement results for the first 95h run	32
4.11	Time pulse measurement results for the 129h run	33
4.12	Time pulse measurement results for the 27h run	33
4.13	Time pulse measurement results for the second 95h run	34
5.1	AERA station map annotating station IDs	40
5.2	AERA station map annotating the antenna angles ϕ to the beacon transmitter	40
5.3	AERA elevation map relative to the beacon height	41
5.4	ROOT plot showing an example event spectrum of station 164	43
5.5	ROOT plot showing an example average spectrum of station 164	43
5.6	Intensity maps for the frequency of 58.887 MHz in channel 1 on May 8th of 2014, 2017 and 2018	44
5.7	Averaged spectra at station 161 in channel 1 on May 8th of 2014, 2017 and 2018	45

5.8	Power Law fits on the mean amplitude data for 9 stations, day 2018-05-08.	47
5.9	Power Law fits on the mean amplitude data for all stations, day 2018-05-08.	47
5.10	Power Law fits on the mean amplitude data/ $\cos\phi$ and a $ \phi $ cut of $< 20^\circ$, day 2018-05-08	48
5.11	Visual compilation of all the fit results of the different methodologies tried so far. The spectral index b varies between -1.7 to -2.7.	48
5.12	AERA Station Map illustrating the angle α	50
5.13	Power Law fit with $\alpha = -3^\circ$ and a $ \phi < 5^\circ$ cut on the 2018-05-08	50
5.14	Spectral index b 's behavior depending on the ϕ position of the antennas. For these fits, the cosine correction was disabled	50
5.15	Evolution of the spectral index b over the course of June 2018	51
5.16	Evolution of the spectral index b over the course of December 2018	51
5.17	Illustration showing r_0 and r_1 for a specific FD beacon scenario	52
5.18	Visualization of Eq. 5.3, showing to required RD beacon distance r_0 from the array edge for different b 's and contrast scenarios.	53
5.19	Visualization of Eq. 5.4, showing to required contrast c for different distances r_0 and b 's.	53
5.20	Plots of the angular elevation at which a beacon antenna appears above the horizon, as viewed from a radio station at varying distances.	55
A.1	Handwritten table with the results of the time pulse measurement campaign	61
B.2	Time pulse measurement results for the 2h test run.	62
B.3	Time pulse measurement results for the 4h test run.	62
B.4	Time pulse measurement results for the 83h run.	63
B.5	Time pulse measurement results for the 55h run.	63
B.6	Time pulse measurement results for first 95h run.	64
B.7	Time pulse measurement results for the 27h run.	64
B.8	Time pulse measurement results for the 38h run.	65
B.9	Time pulse measurement results for the 91h run.	65
B.10	Time pulse measurement results for the 169h run.	66
B.11	Time pulse measurement results for the 129h run.	66
B.12	Time pulse measurement results for the second 95h run.	67
B.13	Time pulse measurement results for the second 95h run, with two fits.	67
B.14	Time pulse measurement results for the 45h run.	68
C.15	Scatter plot of the pre-processed data for path channel 1 and 2, day 2015-10-01	69
C.16	Scatter plot of the pre-processed data for path channel 1 and 2 with outliers marked red, day 2017-05-08	70
C.17	Power Law fit with $\alpha = -3^\circ$ on all stations	71
C.18	Power Law fit with $\alpha = 0^\circ$ on all stations	71
C.19	Fit plot of the anomalously high b value on the 2018-12-04.	72
C.20	Average spectrum of station 161 on the 2018-12-04, when the anomalously high b value occurred.	72
C.21	Evolution of the spectral index b over the course of June 2018, no stations cut based on ϕ	73
C.22	Evolution of the spectral index b over the course of December 2018, no stations cut based on ϕ	73
C.23	Intensity maps of the TV station carrier frequency	74

1 Introduction

The study of cosmic rays – charged particles that traverse the universe at nearly the speed of light – is an important domain within astrophysics. This particular research field is not only fascinating because it bridges the gap from the tiniest to the grandest entities of the cosmos, but also because it benefits from a multi-messenger approach that incorporates data from neutrinos and other astronomical signals. Particularly intriguing is the examination of Ultra High Energy Cosmic Rays (UHECRs), a topic that remains shrouded in many unresolved mysteries. Key among these are the composition of UHECRs, the identification of their sources, and the understanding of their acceleration mechanisms[1].

When a cosmic ray particle interacts with an air nucleus in the Earth’s upper atmosphere, it induces a so called Extensive Air Shower (EAS), as discovered by PIERRE AUGER in the 1930s[2]. The precise measurement of these air showers is crucial to advancing our understanding of high-energy astrophysics. In large ground-based astrophysical experiments, such as the Pierre Auger Observatory[3] in Argentina, vast areas of thousands of square kilometers are instrumented for this purpose. This is only practical by using a distributed network of smaller autonomously operating detector stations working together.

Naturally, the need arises to synchronize the clocks of each station with one another. Current synchronization methods rely on Global Navigation Satellite Systems (GNSS) like the Global Positioning System (GPS), providing a standardized reference system for accurate position and time measurements on Earth. With off-the-shelf mass market GNSS receivers an absolute positional accuracy of about 2 to 3 m is achieved; and a relative time synchronization accuracy of 10 to 15 ns is typically observed[4].

However, time synchronization with 1 ns or even sub-ns accuracy between these detector stations is a very challenging technological problem. Such time synchronization technology would offer exciting possibilities for advancing the precision of cosmic ray air shower measurements. This extends to various applications within the field, including the utilization of radio-interferometric analysis techniques[5][6].

In this thesis, we investigate the capabilities of the latest multi-band GNSS receivers which implement correction techniques to combat the challenges ordinary GNSS receivers are faced with, therefore improving positional accuracy significantly and timing accuracy as well (see Sections 3.1 and 4). Additionally, we study another timing synchronization correction technique, employing a so-called radio beacon reference transmitter[7][8], designed for the synchronization of radio detectors (see Sec. 3.2 and 5).

2 Cosmic ray air showers and radio interferometry

2.1 History of cosmic ray research

The discovery history of cosmic rays began in the early 20th century when scientists started using electroscopes to measure the ionization of air. At the time, it was believed that the observed ionization was caused by radiation emanating from the ground. However, this hypothesis was called into question by THEODOR WULF's experiment in 1910[9]. WULF measured the ionization rate at the top of the Eiffel Tower (at a height of about 300 m) and found that the decrease in ionization rate at this height was much less significant than anticipated.

To further investigate WULF's findings, Austrian physicist VICTOR FRANZ HESS conducted balloon flights in 1911 and 1912. During these flights, he measured ionization at various altitudes, reaching up to 5300 m during a near-total solar eclipse. HESS found that the amount of radiation did not significantly differ from ground-level measurements, nor did it change significantly during the solar eclipse[10]. He reasoned that the source of the radiation must be from beyond Earth's atmosphere and could not be the Sun; it had to be coming from further out in space. By 1929 further experimental methods were devised by German physicists WALTHER BOTHE and WERNER KOLHÖRSTER[11] that confirmed HESS' findings. These methods also determined that the radiation was composed of charged particles, which pervaded the atmosphere. For his discovery of cosmic rays, HESS received the Nobel Prize in Physics in 1936.

However, it was not until 1939 that PIERRE AUGER, a French physicist, discovered the Extensive Air Shower (EAS)[2]. AUGER conducted a series of measurements using multiple Geiger counters located on the Jungfrauoch in the Swiss Alps. He noticed that the radiation detected by his instruments was not constant but came in bursts. By comparing data from the two Geiger counters located at different positions up to 300 m apart, he was able to detect coincidences in the arrival times of cosmic ray particles, indicating that they originated from a single primary particle. He found that these primary particles have very large energies of up to 10^{15} eV. He also concluded that these particles, which make up primary cosmic radiation, must acquire their energy from extensive electric fields[2]. Otherwise, it would be difficult to conceive of a process capable of imparting such high energy to individual particles.

Today, we know that cosmic rays are charged atomic nuclei. They have various proposed origins. While supernova remnants (SNRs) are established sources[12], other phenomena such as gamma-ray bursts and active galactic nuclei are still candidates under investigation[13]. Identifying the exact sources is challenging, mainly because directional information is lost as cosmic rays travel through galactic and extra-galactic magnetic fields. Moreover, the precise mechanisms and processes that accelerate these particles to such high energies, as well as how they propagate across the Universe, remain elusive and not fully understood[1].

2.2 Cosmic ray energy spectrum

The cosmic ray energy spectrum describes the rate of cosmic rays detected as a function of their energy. It is an important tool for understanding their properties and origins of these particles.

Figure 2.1 presents the spectrum using a double-logarithmic plot, a choice that effectively captures the dramatic decrease in particle flux density – defined as the number of particles per unit time, area, solid angle, and energy – as energy levels increase. In such a depiction the curve exhibits an almost linear appearance, closely adhering to a power-law pattern characterized by approximately E^{-3} . This means that as the energy of a cosmic ray increases by a factor of 10, the rate diminishes by approximately 1000-fold. To get a feeling for the dramatic decrease in particle flux, here are some examples: Primary particles with 10^{11} eV, like HESS observed, have rates of about 1 event/ m^2/s ; particles with 10^{15} eV, like AUGER observed, have rates of about 1 event/ m^2/a ; while particles with 10^{19} eV have rates of about 1 event/ km^2/a .

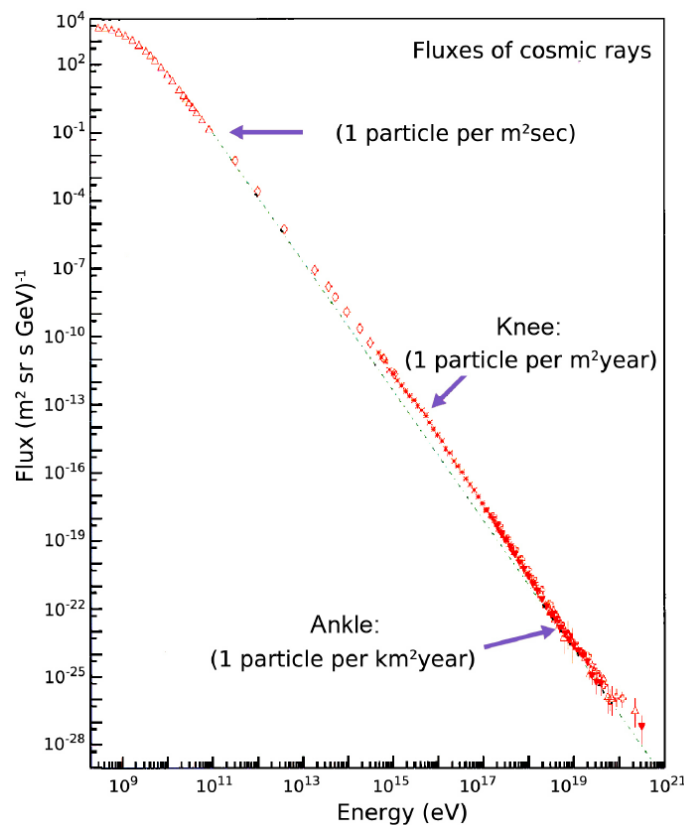


Figure 2.1: Cosmic ray energy spectrum. As can be seen, the flux of cosmic rays detected as a function of their energy largely follows a power-law. Adapted from [14].

Particles with lower energies can be readily detected through modest experiments such as high-altitude balloons or satellite experiments. However, UHECRs – defined as cosmic rays exceeding energies of 1 EeV (10^{18} eV) – pose a substantial challenge for contemporary research. Their detection demands the deployment of extensive experiments spanning thousands of square kilometers. Only through these large-scale setups, like the Pierre Auger Observatory, can UHECRs be captured at rates suitable for in-depth analysis.

The cosmic ray energy spectrum exhibits additional prominent features, like the so-called "knee" and "ankle"[15]. These bends in the spectrum likely mark transitions in the behavior and origins of the particles. For instance, the "knee" is understood to correspond with the energy range where SNRs become less efficient at accelerating lighter particles like protons and helium nuclei, causing the spectrum to steepen. The "ankle", on the other hand, is characterized by a flattening of the spectrum and is speculated to result from the appearance of a new component, primarily composed of protons, of extra-galactic origin. Various theories and models provide different perspectives on these and other features of the cosmic ray energy spectrum. Yet a comprehensive understanding remains elusive, particularly for UHECRs. The GZK cutoff[16][17] imposes an upper limit on their energies due to relativistic interactions with Cosmic Microwave Background (CMB) radiation, while the Hillas criterion[18] offers a framework for identifying potential astrophysical sources capable of accelerating these cosmic rays to such extreme energies.

2.3 Structure of an Extensive Air Shower

An Extensive Air Shower (EAS), depicted in Fig. 2.2, typically originates from high-energy atomic nuclei like protons interacting in the Earth's atmosphere. These primary particles impart their kinetic energy to atmospheric nucleons through high energy hadronic interactions, giving rise to a cascade of secondary particles. Or put another way the primary particles dissipate the energy in the form of newly formed particles. The shower's complexity is captured through its hadronic, electromagnetic, and muonic components, discussed in Sections 2.3.1 to 2.3.3. Additionally, Section 2.3.4 discusses the phenomena of radio emissions originating predominantly from the electromagnetic component of an EAS.

2.3.1 Hadronic component

The hadronic component of an EAS is composed of mesons (like pions and kaons) and baryons (like protons and neutrons). The hadronic cascade is concentrated around the shower axis, since the hadronic particles are heavy and not easily deflected. The majority of these secondary particles are unstable and quickly decay into other types of particles. For example, charged pions π^\pm decay into muons and muon neutrinos. Owing to their large mass and interaction cross-sections, hadronic particles often reach deeper into the atmosphere, initiating sub-showers and contributing to the overall shower structure.

2.3.2 Electromagnetic component

The electromagnetic component includes electrons, positrons, and photons. These particles are generally the result of decays from the hadronic component or are generated via processes like pair production and bremsstrahlung. As these particles travel through the atmosphere, they initiate further cascades by emitting photons or creating electron-positron pairs, increasing the particle count. Eventually, as the available energy for subsequent interactions diminishes, the electrons and positrons reach the "critical energy" threshold. Below this level, ionization processes start to dominate over bremsstrahlung, leading to a reduction in the number of particles within the cascade. The evolution of this cascade

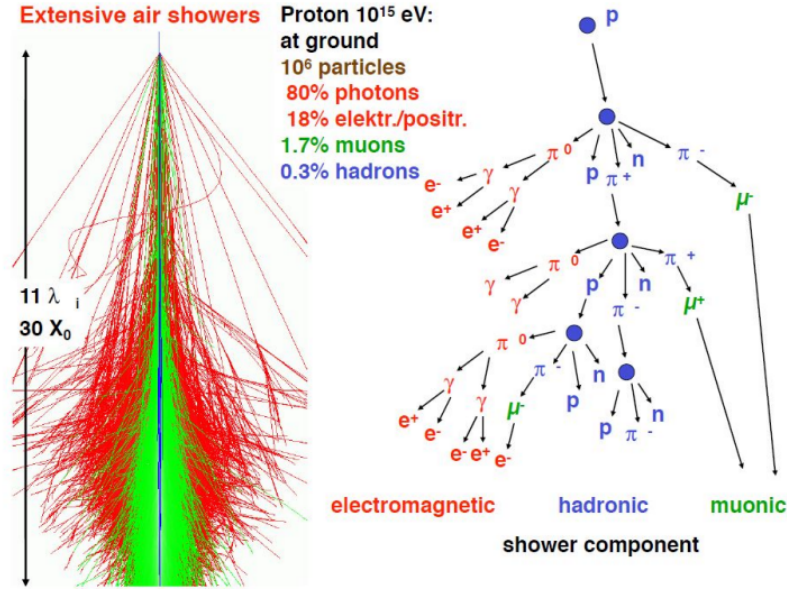


Figure 2.2: *Left*: Simulated Extensive Air Shower (EAS) cascade. λ denotes the hadronic interaction length and X_0 the radiation length. *Right*: Schematic illustration detailing the various components of the shower, together with their possible decay pathways[19].

is a key insight for calculating the mass of the primary particle. The atmospheric depth at which the cascade reaches its maximum number of particles (typically 10^5 to 10^{11} particles) is called X_{\max} . It is dependent on the energy E_0 and mass A of the primary particle: $X_{\max} \propto \log(E_0/A)$. As the Earth's atmosphere is acting as a massive absorber, only showers with primary energies above 10^{13} eV are able to reach ground level.

2.3.3 Muonic component

Muons in an EAS arise from the decay of charged mesons, particularly pions and kaons. Compared to the electromagnetic and hadronic components, muons are less likely to interact with atmospheric particles due to their minimum ionizing particle nature – stemming from their higher mass compared to electrons. Therefore, they can reach ground level relatively unhindered. And even though muons are unstable particles with a half-life $t_{1/2} = 2.2 \mu\text{s}$, they can reach the Earth's surface before they decay, because of the time dilation they experience as they travel at relativistic speeds. They are often detected in ground-based experiments. Their presence and abundance, together with the electromagnetic component, provide the necessary clues for calculating the energy of the shower's primary particle.

2.3.4 Radio emissions from cosmic rays

In an EAS impulsive radio signals are predominantly emitted by the electromagnetic component. These radio emissions are mainly driven by two physical mechanisms: the geomagnetic emission and the charge-excess emission. These mechanisms are discussed in more detail below. Emissions from different regions in the EAS add up coherently, with the intensity depending on the observers location. Meanwhile, the refractive atmosphere leads to a Cherenkov-like time compression, resulting in short radio pulses. Analysis strategies for these radio signals have been developed to extract primary cosmic ray parameters, such as energy, arrival direction, and estimators for their mass. For a more detailed discussion on radio detection and its development in the field of cosmic ray physics, please refer to [20] and [21].

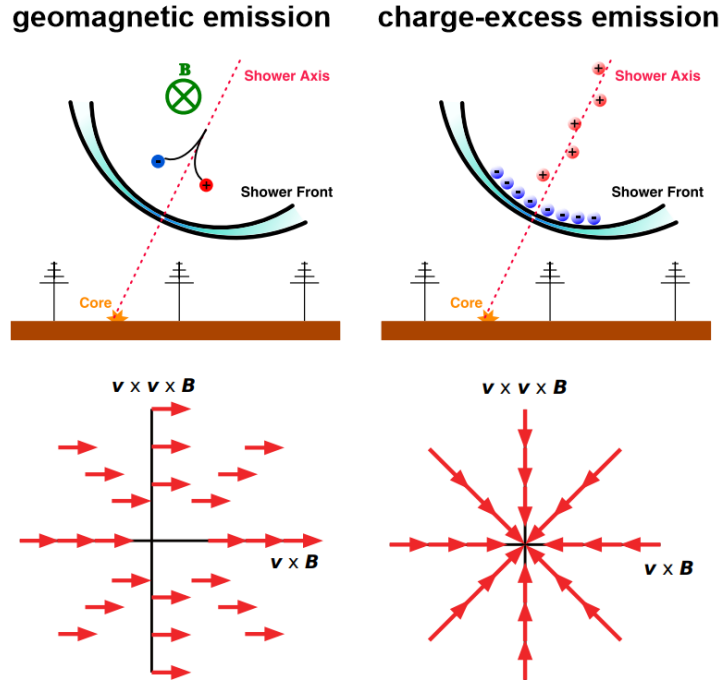


Figure 2.3: *Top*: geomagnetic emission and charge excess emissions visualized. *Bottom*: the respective polarization directions. Adapted from [20]

Geomagnetic emission

This is the primary mechanism for impulsive radio emissions from air showers. The geomagnetic emission is produced due to the acceleration of electrons and positrons in the Earth's magnetic field. The Lorentz force $\vec{F} = q\vec{v} \times \vec{B}$ acting on these charged particles, in combination with deceleration through interactions with atmospheric molecules, causes them to emit radiation polarized perpendicular to their velocity and the magnetic field, see Fig. 2.3 (left). As the shower evolves, reaches a maximum, and dies out again, there is a time-variation of the associated transverse currents. This directly leads to electromagnetic radiation, as per Maxwell's Equations. Because of the relativistic speed of the emitting particles, the emission is forward-beamed, pulsed, and has broad-band frequency spectra.

Charge-excess emission

The charge-excess radio emission arises due to the imbalance of electrons and positrons in the shower, stemming from ionization electrons being swept with the cascade while the heavy ionized nuclei stay behind. As the electromagnetic cascade develops, an excess of negatively charged electrons over positively charged positrons grows to a maximum and dies down again. So, there is a time-variation of charges, again leading to electromagnetic pulses. The charge-excess emission is radially polarized toward the shower axis, as illustrated in Fig. 2.3 (right).

2.4 Detection methods for cosmic rays

At the Pierre Auger Observatory[2] in particular, a diverse array of detectors is utilized, offering a unique opportunity for the direct cross-validation of cosmic ray shower parameters. This is achieved through the simultaneous observation and measurement of various physical phenomena with different types of detectors.

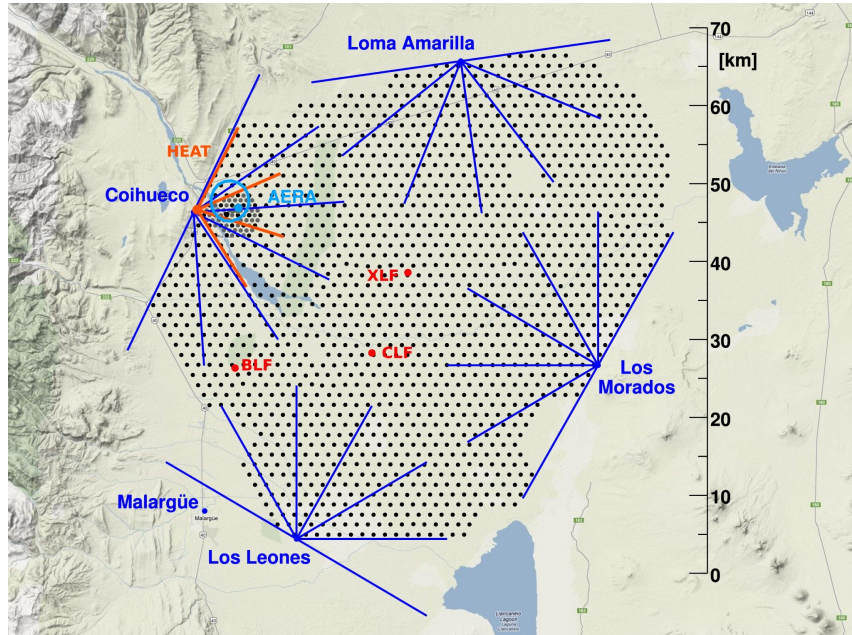


Figure 2.4: Detector map of the Pierre Auger Observatory located in Argentina[26]

As depicted in Fig. 2.4, the majority of the observatory’s enormous area of 3000 km^2 is covered by about 1600 Surface Detector (SD) stations[22]. On the perimeter of the array, there are four sites with Fluorescence Detectors (FDs)[23], each oriented toward the array’s center. Notably, one of these sites hosts an additional specialized FD, called HEAT[24]. It has the capability to adjust its vertical viewing angle by tilting 30 degrees, enabling measurement of lower energy cosmic rays higher in the atmosphere, when operated in the tilted position.

Furthermore, within the area known as the *infill*, the Auger Engineering Radio Array (AERA)[25] is deployed. This sub-array is explicitly designed to test and validate techniques and detector designs for cosmic ray research with the radio-detection technique. For more details, see Sec. 2.4.3 and Fig. 2.7.

Supporting facilities at the Pierre Auger Observatory include the Central Radio Station within AERA, the Central Laser Facility (CLF), the eXtreme Laser Facility (XLF), and the Balloon Launching Station (BLS). The Control Room and Central Data Acquisition System (CDAS) are situated in a dedicated observatory building located in the town of Malargüe. This facility maintains communication with all four FD sites via dedicated wireless communication towers, while the individual detectors in the array are configured to wirelessly connect to their nearest FD location.

2.4.1 Surface detectors

The primary component of each SD station is a water Cherenkov tank – also called water Cherenkov detector (WCD) – designed to detect the muonic and electromagnetic components of a cosmic ray shower, see Fig. 2.5. They are filled with 12 tons of purified water. These detector stations are spaced approximately 1.5 km apart. They operate by detecting Cherenkov radiation, which is emitted when a charged particle exceeds the speed of light in a medium, creating a shockwave in the electromagnetic spectrum. This is observable as the aforementioned Cherenkov light[27]. Photomultiplier tubes (PMTs) are used to detect this light; each tank contains three PMTs mounted within the tank. The PMTs and communication antennas are solar-powered. These detectors measure the



Figure 2.5: Photo of a Surface Detector (SD) station featuring a solar panel, communications antenna and surface scintillator detector (SSD) panel on top of the water Cherenkov detector (WCD). The electronics are encapsulated in the dome.

footprint of the shower, providing valuable insights into the energy deposited. Additionally, the precise arrival times at each detector within the footprint indicate the arrival direction of the primary cosmic ray particle.

As part of an upgrade of the Pierre Auger Observatory, dubbed AugerPrime[28], these detectors are receiving significant improvements. These include new plastic surface scintillator detectors (SSDs) mounted on top of the water Cherenkov detector (WCD), an additional PMT for extending the dynamic range and updated electronics. Furthermore, underground muon detectors are deployed beside each WCD in the *infill* region to provide direct muon measurements, while radio antennas are also added to almost all WCDs. These enhancements are crucial for gathering a high statistics sample of ultra-high energy events and providing new data on hadronic interactions in energy ranges not accessible by man-made accelerators[28].

2.4.2 Fluorescence detectors

Each Fluorescence Detector (FD) site consists of a building housing six fluorescence telescopes each. This collectively provides for a horizontal field of view (FOV) that spans 180 degrees, as each telescope offers a of 30×30 degree FOV[23]. The electromagnetic cascade of an EAS is exciting the nitrogen molecules in the atmosphere, resulting in fluorescent light in the ultra-violet range. This light can be detected by very sensitive instruments. Each fluorescence telescope is comprised of an aperture, an corrector ring, an spherical mirror, and a PMT camera. The camera assembly incorporates 440 PMTs as light sensors, running at a digitization rate of 10 MHz[23]. Due to their extreme sensitivity, they are only safely operational during moonless dark nights, resulting in a duty cycle of no more than 15%. The FDs allow for an accurate geometric reconstruction of the shower, if an event was observed by at least two FD sites, or one FD and one SD. This crucially enables measurement of X_{\max} , in addition to the arrival direction of the primary cosmic ray particle.

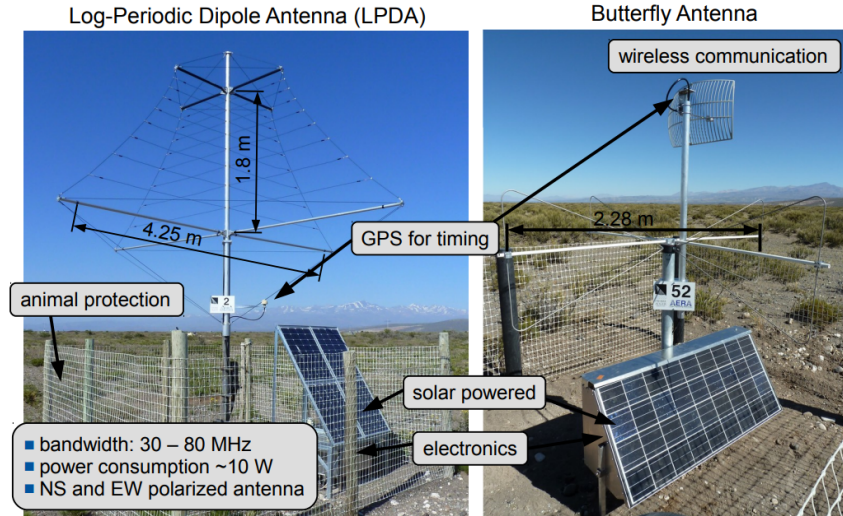


Figure 2.6: AERA stations with LPDA (left) and Butterfly antenna (right)[29]

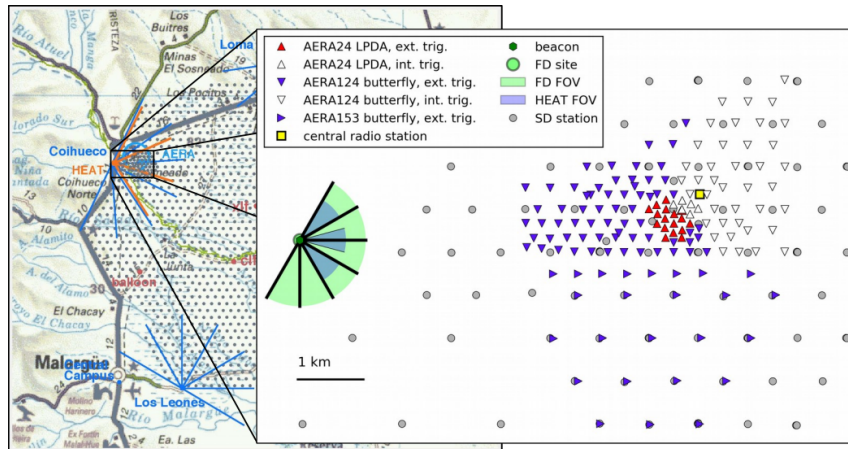


Figure 2.7: AERA stations deployment map[29]

2.4.3 Radio detectors

The Auger Engineering Radio Array (AERA) aims to evaluate the strengths and limitations of radio detection for UHECRs and to contribute data for studying the transition from galactic to extra-galactic cosmic ray sources. A map of the deployed stations can be viewed in Fig. 2.7. The deployment of AERA was staggered in phases. Initially, in 2011, 24 stations featuring dual-polarization Logarithmic Periodic Dipole Antennas (LPDAs)[30], see Fig. 2.6 (left), were established on a 144 m triangular grid. In a subsequent phase in 2013, an additional 100 stations with Butterfly antennas[30], see Fig. 2.6 (right), were deployed on grids ranging from 250 to 375 m. These incorporated more diverse electronics, with some stations including small scintillators for localized triggering. A third phase in spring 2015 added 25 more stations with a grid spacing up to 750 m, thereby covering an area of approximately 17 km² in total. AERA stations operate within the 30 to 80 MHz frequency band. The majority of the stations have a deep buffer and read out the radio data upon receiving triggers from the Surface Detector (SD) array.

As part of the AugerPrime upgrade[28], nearly 1600 Short Aperiodic Loaded Loop (SALLA) antennas, sensitive as well in the 30 to 80 MHz band, are currently being deployed across the entire Pierre Auger Observatory field, on top of the existing SD stations. This array of radio antennas will form the Auger Radio Detector (RD). It enables energy

measurement of the electromagnetic cascade in inclined air showers with zenith angles greater than approximately 65° . For such geometries the WCD mainly measures the muon component of these showers, as the electromagnetic cascade of an EAS is largely absorbed by the atmosphere. The combination of RD and WCD extends the Observatory's mass-composition sensitivity to high zenith angles and thus expands the sky coverage at the highest energies[31].

While the radio measurements at AERA are conducted by autonomous stations with their own power supply and GPS-based time reference, the RD utilizes the infrastructure and GPS time reference provided by the SD.

2.4.4 Radio interferometry

Radio interferometry, leveraging the phase information in radio signals, is a potent and extensively used technique in all of astronomy, for the study of distant cosmic sources. In these astronomical settings, sources are typically situated at effectively infinite distances from detectors. Thus incoming signals are often approximated as planar waves or parallel rays. However, the scenario in cosmic ray physics is quite different. The source of the radio emission is both spatially extended and relatively close to the detectors. Therefore, the far-field approximation and the parallel-ray approach do not apply, requiring a unique set of analytical and computational strategies. However, this difference is actually what enables the 3D reconstruction of the shower properties.

Radio interferometric measurements were already demonstrated in 2005, as noted by the LOPES experiment[32]. Subsequent simulation studies have indicated that radio interferometric techniques (RITs) show great promise for achieving highly accurate measurements of X_{\max} [5][6]. However, excellent time synchronization of the detectors is essential for obtaining these promising results[33].

As mentioned in Sec. 2.3.4 the radio signals from an EAS are impulsive and time-compressed due to the refractivity of the atmosphere. Consequently the detectors measure pulses with durations on the order of nanoseconds, while a Cherenkov-like-cone feature is observed in the radiation pattern on the ground, where the radiation is maximally coherent. The radio interferometric technique (RIT) leverages these properties, by capturing the emission waveforms $S_i(t)$ at multiple receiver locations i and summing them after correcting for the light-propagation time $\Delta_{i,j}$ [5]:

$$S_j(t) = \sum_i^n S_i(t - \Delta_{i,j}) \quad (2.1)$$

Thus, the coherent and curved wavefront $S_j(t)$ can be mapped back to various locations j . The actual light travel time $\Delta_{i,j}$ is crucial, as we are interested in impulsive signals, and is approximated as

$$\Delta_{i,j} \approx \frac{d_{i,j} \bar{n}_{i,j}}{c}, \quad (2.2)$$

where $d_{i,j}$ is the distance between locations i and j , \bar{n} the average atmospheric refractive index along the path between i and j , and c the speed of light in vacuum. Deviations from regular atmospheric variations have been found to have minimal impact on the method.

The reconstruction approach used to identify the shower axis generally works as follows[5]: In the first step a initial horizontal plane is defined at an average altitude of an expected shower maximum. An iterative search for the maximum power position is performed in this plane, with the resolution being adjusted in each iteration to converge on the "hottest" pixel. Using this initial maximum power location new horizontal planes are defined. In each

plane, another maximum power search is conducted. These steps are nicely visualized in Fig. 2.8 from [5]. A track fitted to these maxima yields initial estimates for a ground-level impact point, and the azimuth and zenith angles of the shower axis. Using these initial axis parameter estimates, the integrated power along a predefined track length is maximized by varying the parameters, which allows to locate and estimate the atmospheric depth at which the coherent emission is maximal, which in turn can be related to the depth at which the particle number is highest, X_{\max} . This was also recently visualized in Fig. 2.9 from [33], where the importance of an accurate time synchronization – through a reference beacon – is also highlighted.

In particular the simulation studies[5][6] showed that a direction resolution of $< 0.2^\circ$ and a resolution on X_{\max} of $< 10 \text{ g/cm}^2$ are in principle attainable through radio measurements alone. As seen in Fig. 2.10 from [6] this accuracy is dependent on a sufficiently large numbers of antennas per event, and crucially the time synchronization accuracy of the detectors. As per [6], to achieve an X_{\max} resolution of $\sigma_{X_{\max}} \leq 20 \text{ g/cm}^2$, more than 50 antennas are required when data is time-synchronized to within 1 ns in the 30 to 80 MHz frequency band. If the time synchronization accuracy is reduced to 2 ns, then approximately 200 or more antennas are needed for the same X_{\max} resolution. With such accuracy RIT has the potential to play a crucial role in unraveling the mass-composition of UHECRs.

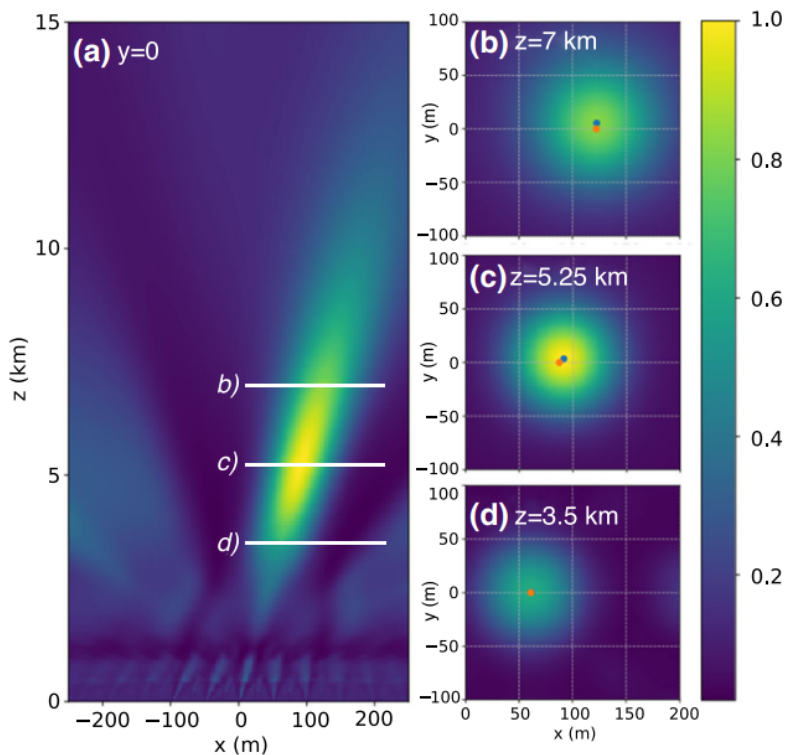


Figure 2.8: The radio interferometric technique (RIT) applied to a simulation of an EAS. Panel $a)$ shows the normalized power of $S_j(t)$ in Eq. 2.1 in the vertical shower axis plane. Panels $b)$ $c)$ and $d)$ show planes perpendicular to the shower axis, with the orange dots marking the true shower axis and the blue dots marking the maximum in the power map[5].

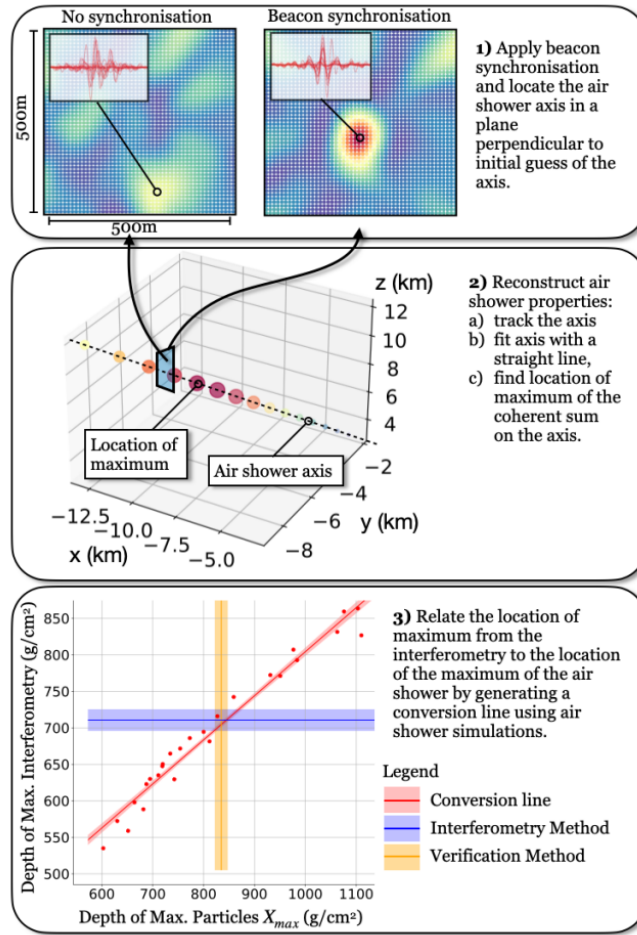


Figure 2.9: Interferometric reconstruction of an air shower axis and X_{\max} [33].

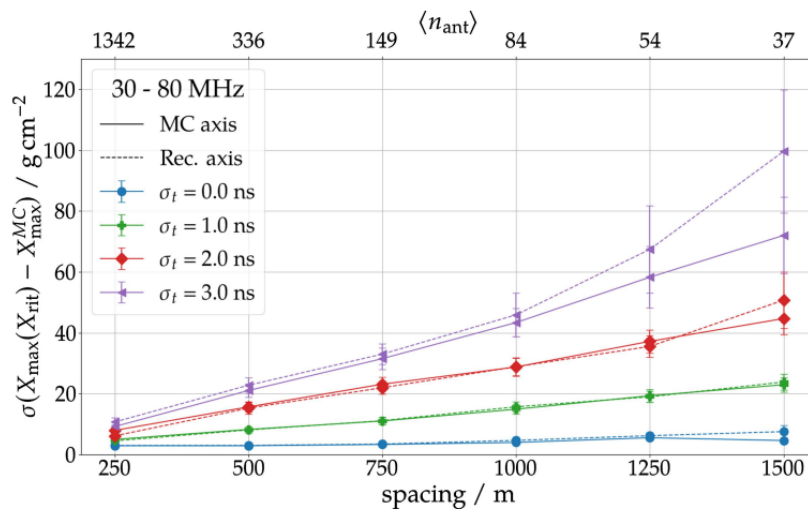


Figure 2.10: Reconstruction resolution of X_{\max} shown for different time jitter scenarios and depending on different antenna spacings[6]

3 Synchronization of distributed detectors

This section aims to provide a comprehensive overview of time synchronization methods for devices, with further details and background relevant for this thesis discussed in Sec. 3.1 and 3.2.

In general, wired connections are preferred for synchronizing clocks, as they are more stable and predictable than wireless connection methods. A favored option in this context is the White Rabbit Precision Time Protocol (WR PTP), which has been developed and established by the European Organization for Nuclear Research (CERN). This protocol extends the capabilities of the PTP standard, enabling synchronization with sub-nanosecond accuracy and picosecond precision on package-based wired networks[34][35].

However, in cases like the Pierre Auger Observatory, where detectors are kilometers apart and need to operate autonomously, a wired connection is not viable. This is due to hardware requirements, installation costs, and maintenance concerns. In such scenarios, it is common to use commercially available GNSS (Global Navigation Satellite System) receivers – more commonly referred to as GPS (Global Positioning System) receivers, named after the first GNSS constellation. These receivers conveniently provide a reference time signal that is synchronized with Coordinated Universal Time (UTC).

Typical GNSS receivers achieve an absolute timing accuracy on the order of 10 to 100 ns and a relative time synchronization of better than 20 ns [4]. However, such accuracy is insufficient for high-precision scientific endeavors, such as radio interferometric analysis techniques, which require 1 ns of relative time synchronization (see Sec. 2.4.4). That said, there are several methods and ideas that enhance the accuracy of GNSS-based measurements (see Sec. 3.1.5).

Another technique, already used at Pierre Auger Observatory’s AERA, employs a so-called radio beacon reference transmitter, see Sec. 3.2. It is shown to correct small timing drifts to within 2 ns or better for radio measurements. This beacon, whose signals are recorded within the standard event data stream, emits sine waves at four distinct radio frequencies. The relative phase information received at the detectors with known position can be used to correct GNSS clock drifts on a per-event basis[8].

Efforts are in progress to develop a wireless version of the White Rabbit Protocol, with latest published results from 2020 achieving time jitter on the order of 10 ps over a 500 m 71 to 76 GHz wireless link[36]. However, the cost of deploying such a system is likely to be quite high.

3.1 Background on Global Navigation Satellite Systems

Global Navigation Satellite Systems (GNSS) have revolutionized modern navigation, positioning, and timing applications since their inception. This section will provide an overview on GNSS, their functionality and technological implementation (see 3.1.1, 3.1.2, 3.1.3). Additionally, this chapter will discuss the accuracy limitations of these systems, the reasons behind them, as well as techniques to mitigate these limitations (see Sec. 3.1.4, 3.1.5).

3.1.1 General information and functionality of GNSS

GNSS refers to constellations of satellites in Medium Earth Orbit (MEO) that constantly broadcast signals to receivers on Earth, allowing for precise positioning, navigation, and timing calculations by these very receivers. No further network connections are required. These satellite constellations are managed by different countries or groups of countries. The main GNSS currently in operation are the United States' GPS, Europe's Galileo, Russia's GLONASS, and China's BeiDou. See Fig. 3.1 for an illustration of some constellations.

The underlying principle by which these systems enable positioning in space and time is by means of trilateration: In geometric terms, the location of the receiver is where spheres centered around three satellites intersect. But since this is only true if the receiver's clock and the satellites' clocks are perfectly synchronized, a fourth satellite is needed to correct for the time discrepancy between them. Mathematically, the receiver must solve for four unknown variables: the three spatial coordinates of the receiver and the time offset between the receiver's clock and the satellite clocks. To uniquely determine these variables, four independent equations are required. These are provided with the precise position and time information of four satellites at the time of their respective signal transmission. This enables receiver to calculate the travel time of each satellite's signal, corresponding to the sphere radii. Additional satellites improve the statistics of the solution.

All satellites within GNSS constellations like GPS or Galileo broadcast at the same frequencies. So that receivers can distinguish individual satellite data-streams from each other, the network employs the code-division multiple access (CDMA) spread-spectrum technique. In this setup, low-bitrate message data is encoded with a high-rate pseudo-random noise (PRN) code unique to each satellite. Receivers must be aware of each satellite's code to accurately separate and reconstruct their corresponding message data.

In case of the GPS signals, a full navigation message consists of multiple 1500 bit and 30 s long data-frames, each made out of 5 sub-frames. Each data-frame is transmitted exactly on the minute and half-minute, as indicated by the atomic clock on each satellite. Each sub-frame begins with telemetry and handover words. The first sub-frame of each data-frame contains the satellite board time, expressed as a week number and a time of week count. The second and third sub-frames provide the precise orbit parameters (called ephemeris data) of the satellite. The fourth and fifth sub-frames hold the so-called almanac data, which is distributed over 25 data-frames. It contains coarse orbit and status information for the another satellites in the constellation and various error correction data. It also provides information that relates the GPS time to UTC, see Sec. 3.1.3.

3.1.2 Examples of GNSS: GPS Navstar and Galileo

GPS Navstar

The United States' Global Positioning System (GPS), originally known as Navstar GPS, is the first and best-known GNSS. Today, the abbreviation GPS is colloquially used and sometimes even technically used, as a generic term for GNSS. Initially developed

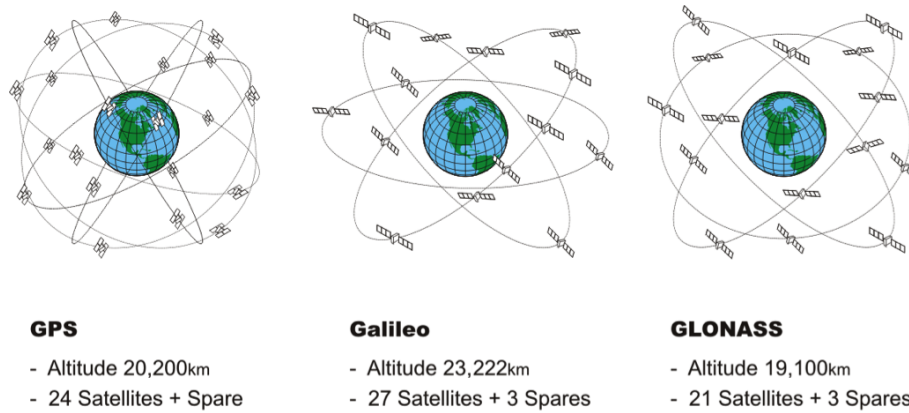


Figure 3.1: Examples of different GNSS constellations. Adapted from [38]

for military purposes in the 1970s by the United States Department of Defense (DoD), GPS became available for civilian use in the 1980s – following the Korean Air Lines Flight 007 disaster, where the plane mistakenly flew into Soviet prohibited airspace and was consequently shot down. The system became fully operational in 1993. However, until 2000, the publicly available navigation signals were intentionally degraded by a feature called Selective Availability (SA), which resulted in errors of up to 100 m. Selective Availability intended to deny an adversary the use of civilian GPS receivers for misuses such as precise weapon guidance. After the deactivation of this program, GPS had an accuracy of about 5 m. Today’s consumer devices, like smartphones, can also be as accurate as 5 m – provided good signal conditions.

The GPS currently consists of 31 operational satellites of which eight are used as spares, ensuring global coverage and redundancy. The GPS Navstar system is divided into three segments: the space segment, the control segment, and the user segment. The space segment is comprised of 24 to 32 GPS satellites, which are arranged in six orbital planes with four satellites each, at an altitude of approximately 20 200 km, plus spares. This ensures that at least six satellites are always within line-of-sight from everywhere on Earth. The control segment consists of a global network of ground stations responsible for tracking and adjusting the satellites, while the user segment refers to the receivers on Earth that process the signals transmitted by the GPS satellites locally.

Galileo

Galileo is the European Union’s GNSS, designed to provide an independent global navigation solution. Launched in the 2010s, the system became partially operational in 2016, and nearly fully operational around 2021. The constellation is meant to consist of 24 to 30 satellites arranged in three orbital planes with eight satellites each at an altitude of approximately 23 222 km, plus spares. However, only 23 satellites are active[37], with further satellite launches planned in 2024 and onwards. As will be discussed below in Sec. 3.1.5, Galileo offers positioning accuracy that surpasses the other available GNSS.

3.1.3 GPS time

A globally uniform time system is provided with each GNSS system, with each satellite equipped with one or more atomic clocks. In the case of the GPS system, the time received by a GPS receiver is initially GPS time, an atomic timescale without leap seconds. The satellite message contains the current difference between GPS time and UTC. As of November 2022, GPS time is 18 s ahead of UTC. This allows the receiver to calculate the

exact UTC. Given that the travel time of the GPS signal is determined accurately, the GPS system guarantees a deviation from UTC of $\leq 10^{-6}$ s. With a specialized time transfer receiver at a fixed, known location an absolute time accuracy relative to UTC of ≤ 30 ns is promised for 95% of the time[39].

3.1.4 Accuracy limitations of GNSS and their causes

Despite its widespread use and success, GNSS has certain accuracy limitations due to various factors. These include the following:

- **Atmospheric effects:** The speed of GNSS radio signals, as they pass through the ionosphere, depends on the degree of its ionization. As a result, the signal travel time is not only dependent on the distance to the satellite but also on the ionospheric conditions, resulting in trilateration calculation errors.
- **Multipath errors:** Multipath errors occur when a GNSS signal reflects off buildings or other structures before reaching the receiver, causing the signal to travel a longer distance than intended. This results in an incorrect measurement of the distance between the satellite and the receiver, also leading to calculation errors.
- **Satellite geometry:** The accuracy of GNSS also depends on the geometric configuration of the satellites in view, known as the Geometric Dilution of Precision (GDOP). A poor GDOP occurs when satellites are too closely clustered in the sky, making the trilateration process less precise.

Additionally, the quality and capabilities of the GNSS receiver play a significant role in determining the overall positioning accuracy. Also, horizontal accuracy is typically twice as good as vertical accuracy. This is due to satellites being visible in all horizontal directions, while half of the vertical view is obstructed by the Earth's surface.

3.1.5 Techniques to mitigate GNSS inaccuracies

Several techniques have been developed to mitigate the accuracy limitations experienced by GNSS receivers. These include the following:

- **Differential GPS (DGPS)** is a technique that utilizes fixed reference GNSS antennas with precisely surveyed locations. From the discrepancy between the calculated position and the known position, the actual signal transit times from each satellite are determined. The corrections on the theoretical transit times are then broadcast to nearby receivers, resulting in an improved positional accuracy for them.
- **Satellite-Based Augmentation Systems (SBAS)** are regional systems that use geostationary satellites to transmit correction information to GNSS receivers. These systems provide real-time corrections for satellite orbit and clock errors, as well as atmospheric delays. Examples of SBAS include the United States' Wide Area Augmentation System (WAAS), Europe's European Geostationary Navigation Overlay Service (EGNOS), and Japan's Multi-functional Satellite Augmentation System (MSAS).
- **Multi-Band** measurements can be used to estimate the ionospheric delay by comparing travel times across two or more GNSS frequencies. This is possible because the effect of the ionosphere is dispersive, meaning it affects signals of different frequencies by different amounts. Civilian navigation devices typically received GNSS satellite signals on a single frequency. The first mass-market dual-frequency receiver, the *Broadcom BCM 47755* chip, was introduced in 2018. Meanwhile, the GPS' encrypted military code has utilized multiple frequency bands from the start.

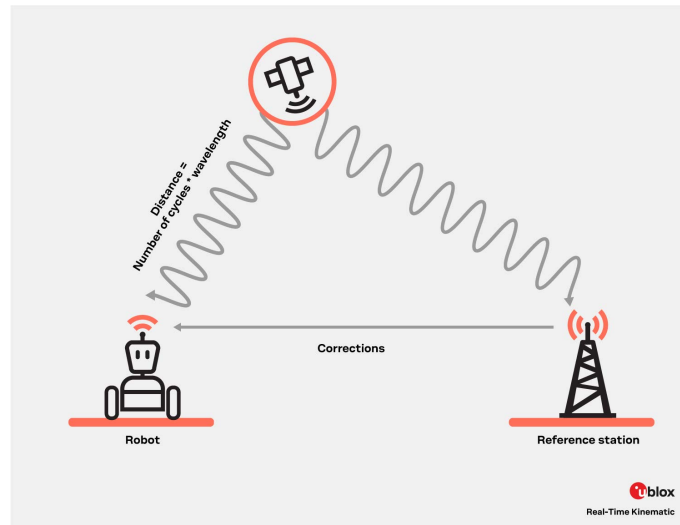


Figure 3.2: Infographic on RTK from ublox [40], which schematically illustrates how the base and rover communicate with the GPS/GNSS satellites. The arrows indicate the direction of communication.

- Real-Time Kinematic positioning (RTK)** is an advanced technique that utilizes carrier-phase measurements from multiple satellite signals to achieve centimeter-level positioning accuracy. The radio carrier waves of GPS signals have wavelengths in the 20 cm range¹. A distance with centimeter accuracy to the satellites can be calculated from the known radio wavelength, number of wave cycles, and phase. Without the carrier phase information, the calculations will be less precise. RTK requires a base station with a known position and a rover receiver, which receives real-time information from the base receiver to calculate a precise relative position (refer to Fig. 3.2). As long as the rover receiver tracks the same satellites as the base, a single base receiver is sufficient. This is typically possible within a radius of about 30 km around the base. The correction data can also be received through an internet connection using the Networked Transport of RTCM via Internet Protocol (NTRIP). Specialized service providers offer this service, allowing for greater range and flexibility without direct radio links between the receivers and without the need to deploy a self-operated base station.

Modern GPS receivers using the L5 frequency band can achieve high positioning accuracy, with an accuracy of up to 30 cm. High-end users, such as those in engineering and land surveying applications, can achieve even higher accuracy using the above mitigation techniques like RTK. They can achieve accuracies within 2 cm or even sub-millimeter accuracy for long-term measurements.

It is worth noting that Galileo offers enhanced positioning accuracy compared to other GNSS. The originally fee-based and encrypted Commercial Service (CS) was repurposed as the public, first of its kind, Galileo High Accuracy Service (HAS)[41]. Since January 2023, all users have free access to three frequency bands and correction data, enabling global accuracy on the decimeter scale. This enhancement offers global users correction data for satellite orbits, clock timing, and both code and phase biases. Additionally, for those within the European Coverage Area, ionospheric corrections and potentially other bias adjustments are available. Rather than relying on geostationary satellites to disseminate the correction data (like the discussed SBAS), each satellite in the Galileo constellation

¹GPS' so-called L1 band operates at 1575.42 MHz, L2C at 1227.60 MHz, and L5 at 1176.45 MHz

transmits it directly. Optionally the HAS corrections can also be received via NTRIP. For early observations, please refer to [42], where positional precision to within 10 cm was observed. However, until HAS is in full service in 2024 convergence times remain high on the order of one hour, rather than minutes.

The accuracy of absolute positional measurements is also linked to the reference frame being utilized. For instance, GPS employs the World Geodetic System 1984 (WGS84) as its reference coordinate frame, which is regularly aligned to latest realizations of the International Terrestrial Reference Frame (ITRF)[43]. The latter serves as the fundamental and global reference frame used in geodesy. These coordinate frames are subject to change, due to factors such as seismic activity and plate tectonics, with different regions on Earth experiencing position changes of up to several centimeters per year. While the underlying reference systems are defined once, their corresponding frames are subject to recalculation at irregular intervals. In Europe, the European Terrestrial Reference System 1989 (ETRS89) is regarded as the most accurate coordinate system and serves as the exclusive reference frame for mapping and surveying activities across the continent. It utilizes fixed anchor and reference points connected to the bedrock of the stable part of the Eurasian plate. Maps and coordinates based on ETRS89 are not subject to change. So, the compatibility between the WGS84 and ETRS89 reference frames can typically only be ensured up to decimeter accuracy, depending on the specific realizations that are aligned with the ITRF at different points in time.

Another relevant aspect to consider in the context of this thesis is that the mentioned mitigation methods are commonly employed in real-time applications within commercial settings. Implementing these methods often requires the utilization of specialized GNSS hardware designed specifically for these purposes. However, for scientific measurement campaigns, it is conceivable to use these methods offline², eliminating the need for long-range wireless connections for real-time clock synchronization. The only requirement is the availability of additional correction information, which can be recorded and stored alongside the data. However, at present, this correction information is not readily accessible everywhere and needs to be generated by the end-users or third-party services.

3.2 The AERA beacon reference transmitter

A beacon reference transmitter is a specialized hardware setup designed to address time synchronization deficiencies in an existing radio detector array[7][8]. The AERA beacon transmitter, is operated in the vicinity of the Auger Engineering Radio Array (AERA) and is stationed on the Coihueco FD Site's communications tower (see. Fig. 3.3 and 3.4).

The hardware consists of a signal generator, complete with an amplifier, which is connected to a passive, horizontally-aligned dipole antenna through a coaxial cable. This system mixes signals from four Temperature Compensated Crystal Oscillators, offering a high-frequency stability of a few parts per million. The dipole antenna emits signals in a horizontal polarization, roughly parallel to the North-South axis of the AERA stations' antennas. As a result, the beacon signal is primarily registered in the North-South channel of each station, with only marginal visibility in the East-West channel.

The signal from this transmitter is recorded within AERA's standard data stream whenever a trigger occurs. This could be when an air shower event is detected, or a periodic trigger is issued for background monitoring purposes. Since the signals are very narrow-band, and the radio pulses from EAS are broad-band, the analysis of the event can be performed with

²meaning measurements can be corrected later during data analysis



Figure 3.3: Photo of the Coihueco communications tower as viewed from the roof of the local FD building. Picture taken on 2022-08-30. Beacon dipole antenna visible below the white dish. For the mount location also refer to Fig. 3.4.

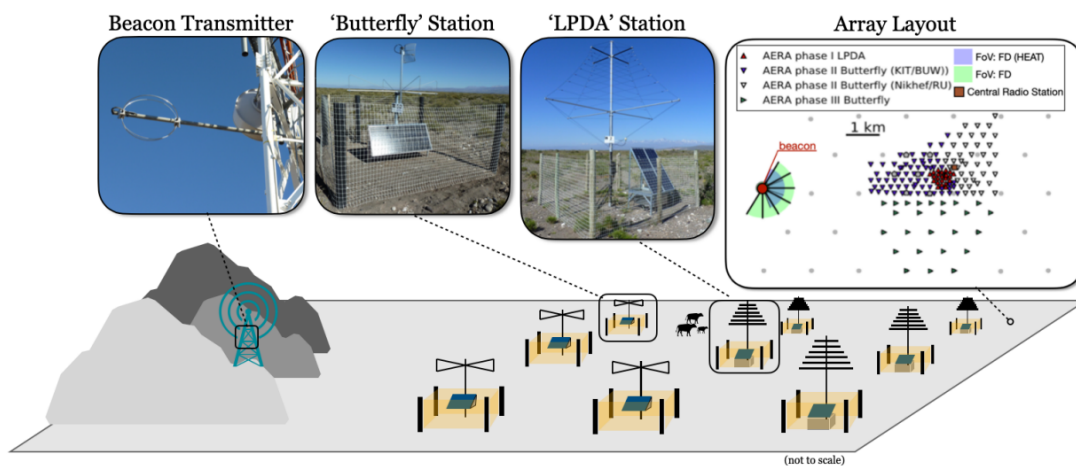


Figure 3.4: Schematic of AERA and its radio beacon reference transmitter for time synchronization[33]. However, the pictured SALLA beacon transmitter antenna has been replaced with a dipole antenna.

minimal loss of data quality, once the beacon signals are suppressed after exploiting them for timing calibration.

The beacon is emitting continuous sine waves at four predetermined frequencies: 58.887 MHz, 61.523 MHz, 68.555 MHz, and 71.191 MHz. They fall within AERA's detection band of 30 to 80 MHz. The four frequencies are chosen in such a way that their resulting superposed signal repeats about every 1.13 μ s, which is called its beat. Thus GNSS time-offsets of up to about 1 μ s can be corrected for, which is more than would be possible for wave cycles of a single sine transmitter. Also the frequencies are adapted to align closely with the Fourier transform frequency bins of recorded AERA time traces. They are also particularly accommodating the AERA station's sampling rates of 180 and 200 MHz and a recorded trace length of at least 2048 samples. This adaptation minimizes aliasing and other signal artifacts, allowing for cleaner data analysis.

The timing calibration is performed by analysis of the phasing information of the beacon signals. The precise positions of the radio antennas and the beacon transmitter are prerequisite knowledge. These have been determined by differential GNSS surveys with a relative accuracy of a few cm. With the distances and an arbitrary choice of a reference radio station, the expected phases of the beacon frequencies at the other stations can be calculated. Comparing the expected phase information with the measured phase information reveals phase offsets, indicating unexpected signal travel time. These are mainly caused by the GNSS clock drift and can thus be corrected for.

The beacon system and its time correction process were independently verified to be working with an accuracy of at least 2 ns by analyzing radio pulses emitted by commercial aircraft with known positions broadcasted in real-time by their ADS-B transponders [8]. To establish the true accuracy and capability of the system would, however, require a time reference which is at least as precise as the beacon method. However, based on preliminary results from interferometric analyses of AERA data[33] we expect the accuracy to even be in the sub-ns range.

4 Evaluation of the timing accuracy of RTK GNSS modules

The main goal of this section is to evaluate the relative time accuracy achievable using a modern, commercially available high-precision multi-band GNSS solution that implements Real-Time Kinematic positioning (RTK).

Section 4.1 provides a detailed description of the hardware used. This is followed by evaluation tests of the GNSS kit in Sec. 4.2. The time accuracy tests are then presented in Sec. 4.3. This section concludes with closing remarks in Sec. 4.4.

4.1 Description on the used hardware

The GNSS kit being evaluated is the *simpleRTK2B Starter Kit LR* from ARDU SIMPLE [44] (see Fig. 4.1). At the core of this kit are two *ZED-F9P-02B* high-precision GNSS modules from the company U-BLOX. They are embedded on two separate ARDU SIMPLE development boards. One module is pre-configured as a base and the other as a rover as the kit aims to be an independent plug-and-play RTK solution (see Sec. 3.1.5 for details on RTK). The development boards serve as an accessible hardware interface between the pinouts of the module and any external components.



Figure 4.1: The *simpleRTK2B Starter Kit LR* from ARDU SIMPLE [44], which is comprised of two GNSS development boards (top left), dual-band GNSS antennas (top right), XBEE radio modules (bottom right), and radio antennas (bottom).

The kit also includes two U-BLOX *ANN-MB-00 GNSS dual-band antennas* and two *XBee* long-range radio modules with radio antennas manufactured by DIGI. This allows the base receiver to transmit RTK corrections to the rover. Under ideal conditions, the wireless radio link is stated to function for up to 10 km [45].

The boards are designed to be compatible with ARDUINO and RASPBERRY PI computers, serving as modular expansions. During the initial experimentation with the kit, RASPBERRY PI computers were tested in conjunction with the GNSS boards. However, they were ultimately not incorporated into the data acquisition pipeline (see Sec. 4.2 for further details).

Additionally, the *PicoScope 6403* PC-oscilloscope is employed for the tests in Sec. 4.3 along with *TA133* 10:1 500 MHz oscilloscope probes. This high-resolution, high-speed PC-oscilloscope features a 350 MHz bandwidth (-3 dB), an up to 5 GS/s (Giga Samples per second) sampling rate in single-channel mode, and a 1 GS buffer memory. Maximum streaming data rates are 1 MS/s using the PICO SCOPE software and >10 MS/s using the supplied Software Development Kit (SDK). The device offers advanced functionalities, such as waveform generation, advanced triggering options, and spectrum analysis. Of particular importance for this study are the availability of advanced triggering options and the time resolution in the 2-channel mode for simultaneously recording data from the two GNSS devices with 2.5 GS/s. This corresponds to a time resolution of 0.4 ns for each channel.

Lastly, a *Windows* laptop is used for the final data acquisition, running the U-BLOX *u-center v22.02* (GNSS evaluation software) and the necessary *PicoScope* software (*PicoScope 6.14.61* and *Pico SDK 10.7.22.241*) to interface with the oscilloscope. The *Pico SDK* C library is used together with `picosdk-python-wrappers` [46], enabling its utilization within a `python 3.7 Jupyter Notebook` environment.

4.2 Evaluation of the GNSS boards

Before beginning with the primary timing measurements, we conduct basic tests to become familiar with the RTK kit and test its capabilities.

Initially, we switch on the boards inside the Institute of Astroparticle Physics at KIT Campus Nord with the antennas near the windows. Although these conditions are non-ideal, as the system is designed for direct line-of-sight with GNSS satellites, the modules manage to establish contact. They obtain a rough position measurement, also called position fix, with an accuracy of several meters (see Fig. 4.2) within one hour.

During this testing phase, we attempt to integrate the RASPBERRY PI computers with the GNSS module and are met with varying degrees of success. While so-called NMEA messages from the GNSS module can be intercepted, further functionality requires the proprietary software from U-BLOX. The NMEA-0183 standard, established by the National Marine Electronics Association (NMEA), defines a serial communications protocol between marine electronics. It defines how these communications are formatted. In the context of GPS equipment, these NMEA messages can include information like current position and time, speed and heading, satellites in view, GDOP values, and more. Our focus shifts from using a *Linux*-based Operating System (such as the *Raspberry Pi OS*) to using *MICROSOFT Windows* for its compatibility with the U-BLOX software. The U-BLOX *u-center* provides easy and detailed control as well as a readout of the *ZED-F9P* modules.

In the next phase, we test outside the institute building (see Fig. 4.3), making efforts to find a spot with the least possible sky obstruction. The conditions remain sub-optimal due to the building blocking a portion of the sky on one side and trees on the other. We

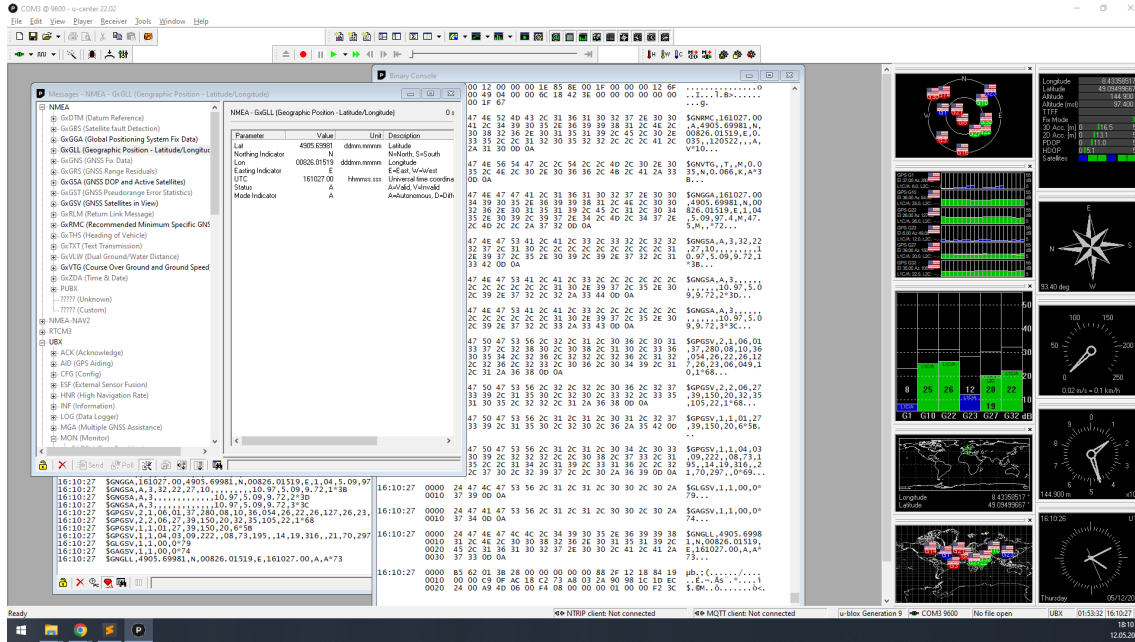


Figure 4.2: Screenshot of the *u-center* software while the antennas were located inside, displaying GNSS message windows and the dashboard on the right. It reports a position fix with a 3D accuracy of 16.5 m. The geographic coordinates are visually confirmed using the GOOGLE MAPS satellite map.

employ portable power banks to power the boards. This allows for greater flexibility while arranging the boards and antennas outside. As expected, reception improves significantly, with a first position fix obtained within seconds after turning the device on. This duration is also called time to first fix (TTFF).

For the RTK to function, the base receiver must first perform a process called survey-in. Assuming the base antenna's position remains unchanged between measurements, this process takes multiple position fixes over a period of time and takes the average. By default, the survey-in concludes when the software determines a position accuracy of 2.5 m. However, the survey-in parameters can be user-adjusted, allowing for completion with a different accuracy or after a specified duration.

Once the base completes its survey-in, it sends the RTK correction via the radio link to the rover receiver. With this information and its own GNSS antenna, the rover calculates the relative position of its antenna with respect to the base antenna. The *u-center* dashboard reports a relative 3D position accuracy of 2 cm and a horizontal 2D position accuracy of 1 cm. It does not directly report the distance between both devices but provides their respective geographic coordinates and elevation. We need to utilize an external tool to calculate the antenna distance in centimeters. We employ a freely available online tool implementing *Vincenty's inverse formula* [47], an iterative algorithm, to calculate ellipsoidal distances on the WGS84 ellipsoid. We cross-check the calculated horizontal distance by using a measuring tape. In these tests, the numbers are accurate within 1 cm. Alternatively, we also validate the horizontal position by moving the rover receiver a set distance. We cross-check this with the subsequent GPS position measurement change which also yields consistent results with less than 1 cm deviation. Additionally, we test the vertical distance by lifting the rover's antenna from the ground to approximately 1.8 m. By checking the reported elevation position change, we verify the vertical positional accuracy on the order of 10 cm, since the elevation display in *u-center* does not provide more digits.



Figure 4.3: Photographs of the setup evaluating the GNSS boards. *Left*: Close-up of the base receiver while it is obtaining a position fix. *Right*: Laptop running the *u-center* software, monitoring the rover receiver and antenna placed on the ground outside the institute building.

4.3 Relative time accuracy tests

The basic operation of the RTK kit has been explored and validated to be functioning as advertised. The next step is to prepare and execute the envisaged time accuracy tests.

This section includes a description of the hardware setup, the software setup, and the testing methodology (Sec. 4.3.1 to 4.3.3 respectively) before the results are presented in Sec. 4.3.4.

4.3.1 Hardware setup

To be able to conduct the time accuracy tests under the best possible conditions, we select a location for the antennas on top of the institute building (see Fig. 4.4). This location provides an uninterrupted line-of-sight to all GNSS satellites above the horizon. This ensures that the GNSS signals are strong and reliable. As ARDUINSIMPLE recommends [48], we mount the GNSS antennas on custom-made 15×15 cm metal plates in order to improve the signal strength. These plates were cut out of 2 mm-thick aluminium. This also has the additional benefit of mitigating unwanted movement of the antennas due to weather.

Instead of using power banks, in this setup, all devices are powered by an electrical power outlet inside the building (see Fig. 4.5). All components except for the antennas are located in the room below the roof location and are sheltered from weather. Both of these aspects enable multi-day measurement runs with minimal need for supervision.

The ARDUINSIMPLE boards have an electrical contact or pin that allows measurement of a pulse-per-second (pps) signal (see Fig. 4.6 Right, 4.7). This pps signal is in sync with the calculated GPS time. These time pulse pins are read out with the oscilloscope probes. The oscilloscope in turn is connected to the laptop, as are the two ARDUINSIMPLE boards (see Fig. 4.6 Left).



Figure 4.4: *Left*: The GNSS antennas are placed next to each other on the selected roof location. *Right*: Close-up of the GNSS antennas, mounted on custom 15×15 cm aluminium plates.



Figure 4.5: Pictures of the time-pulse measurement setup in the room below the roof location. Antenna cables are routed through the windows and the devices are powered by a power outlet.



Figure 4.6: *Left*: Top-down view of the measurement setup. On the left are both GNSS boards, connected to the laptop in the lower center. The oscilloscope is visible on the right and also connected to the laptop. The oscilloscope probes are in the top center, connected to the boards and the oscilloscope. *Right*: Close-up of an oscilloscope probe making contact with the time pulse pin of the ARDUSIMPLE board.

4.3.2 Software setup

As described in the previous sections, the oscilloscope is connected to measure the pps signals from both boards. The measurement has a time resolution of 0.4 ns since the oscilloscope is operating in 2-channel mode. The objective is to find the relative time accuracy. To achieve this, the rising edge of the base receiver's pps signal is utilized as a trigger for data acquisition of the rising edges of both receivers. These rising edges do not occur simultaneously and exhibit a slight temporal shift.

To calculate the relative distance in nanoseconds between the two edges, we develop custom python code. The shift at a signal strength of 100 mV is calculated. At this signal strength, the edges exhibit the steepest slopes, allowing for the local approximation of linearity. Additionally, the code's output displays the measurements in real-time, while the data acquisition (DAQ) is in progress. For python to control the oscilloscope and read out the data, we adapt example code from the `picosdk-python-wrappers` repository [46]. During each measurement run, the relative time shift is calculated and saved every second. We assess the accuracy of the time synchronization using the histogram of the calculated time shifts, as shown in Fig. 4.8.

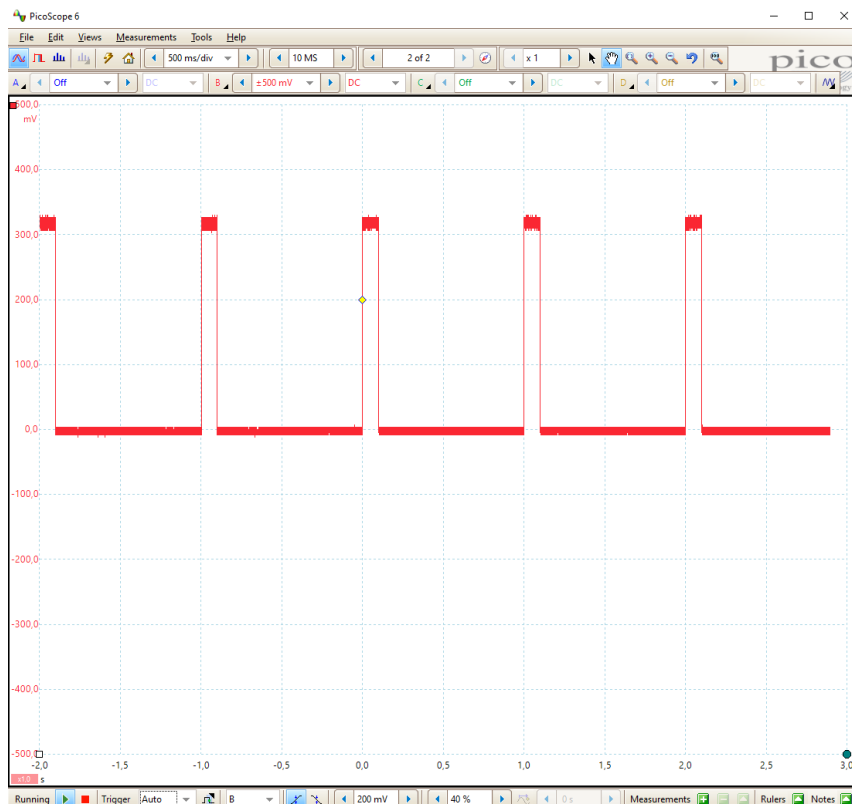


Figure 4.7: Screenshot of PICO SCOPE software displaying the pps signal of one of the ARDU SIMPLE boards. Every second, the measured voltage periodically jumps from 0 mV to about 300 mV for about 100 ms.

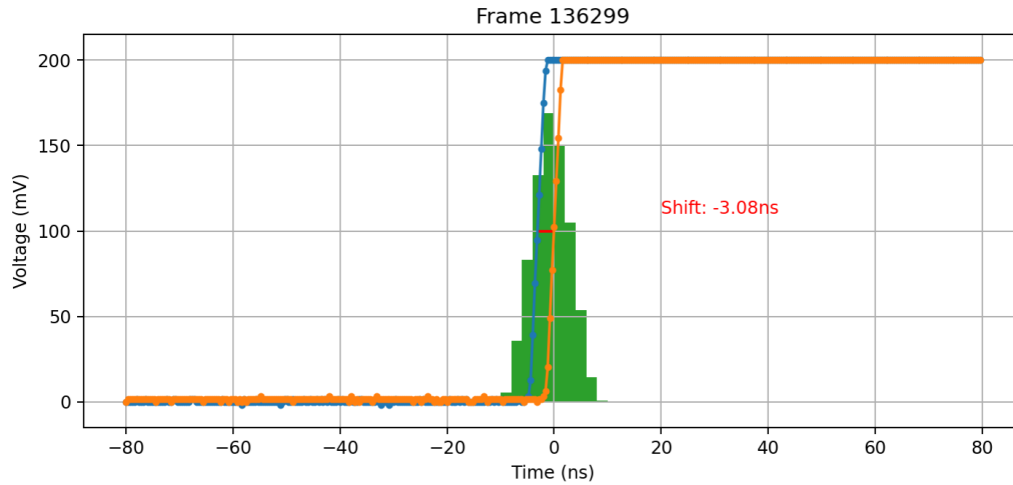


Figure 4.8: JUPYTER NOTEBOOK real-time visualization of the data acquisition displaying the latest pulses. The orange line corresponds to the base pps signal, which is used as a trigger. The blue line corresponds to the rovers' pps signal. The current calculated time-shift is displayed as red text and also as a red line between both curves at the height of 100 mV. A histogram of the time shifts of the current DAQ run is shown in green.

4.3.3 Survey-in of base and measurement methodology

Before executing the measurement runs, a good survey-in of the base antenna is essential. The default survey-in accuracy target is 2.5 m and is achieved within seconds. Since there are no significant constraints in terms of time or power supply, a longer and more precise survey-in process is preferable. This helps minimize potential errors and uncertainties in the crucial base location. We found that setting single-digit centimeter accuracy goals does not converge within a reasonable timeframe. Multi-day survey-ins do not yield significant improvements beyond 10 cm. Most of the accuracy is achieved during the first 24 hours. A relatively simple averaging process is likely responsible for this behavior. Consequently, a 24-hour survey-in setting is chosen for this study.

We place the base antenna at an easily identifiable location, by referencing markings on the roof's surface. It remains stationary throughout the measurement runs. The survey-in, conducted on October 4, 2022, under clear skies with only a few high-altitude cirrus clouds utilized the GPS and Galileo constellations. The survey process achieved a location solution for the base with a 3D mean standard deviation of 11 cm and a 2D accuracy of 9 cm. We inspect the antenna roof location in between the forthcoming measurement runs to ensure the antenna position remains unchanged. We do this by referencing the aforementioned markings on the roof's surface.

A measurement run should last at least two days to yield conclusive results with sufficient statistical significance. Longer durations provide additional data, while shorter durations still offer a useful indication. After conducting a measurement run with default settings, subsequent measurement runs involve adjusting and evaluating various aspects. These aspects include the selection of GNSS constellations utilized, variations in the distance between the GNSS antennas, adjustments to the rover's position-mode (either real-time or fixed position-mode), and notably the utilization of the Real-Time Kinematic positioning (RTK) feature.

Following each run, the saved time shifts between the two pps signals are plotted over time, and a frequency distribution of the measured time offsets between both receivers is created

by binning the data. The resulting distribution is visualized as a histogram and fit with a Gaussian curve to obtain the mean μ and standard deviation σ of the data. The σ -value corresponds to the relative timing accuracy. As a representative example of a final plot, refer to Fig. 4.9.

This approach to the measurement campaign enables a detailed analysis of the different factors that impact the accuracy of the time synchronization.

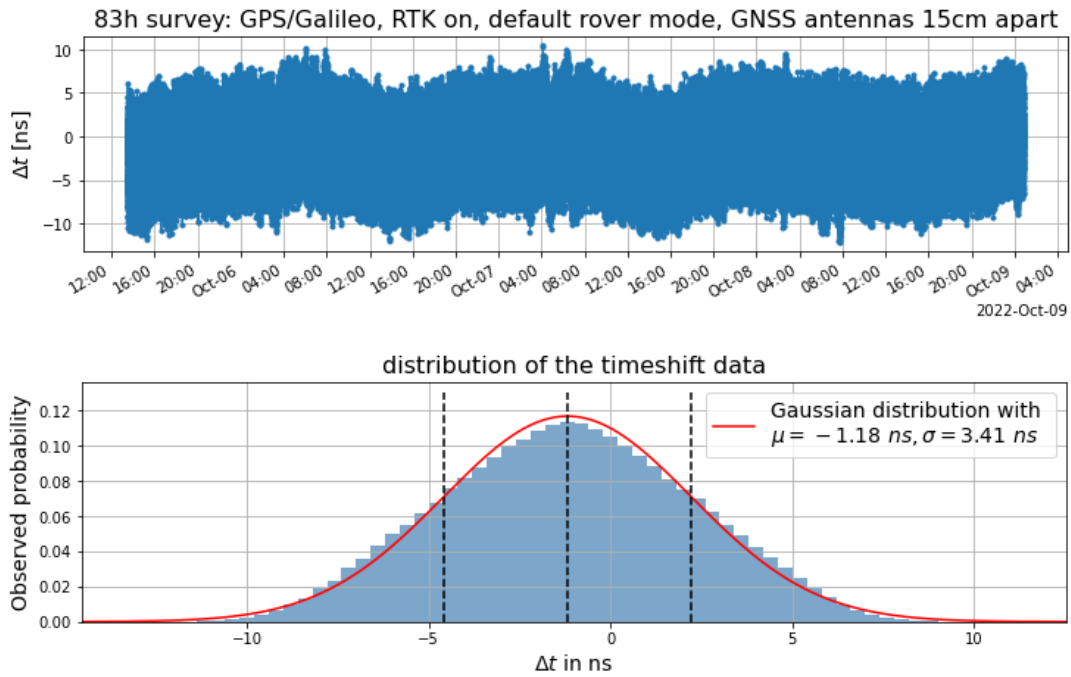


Figure 4.9: *Top:* The relative time-shift between the two pps signals is plotted over time. The periodic drifts of the time shift are likely due the changing geometric configuration of the satellites in view, called GDOP, as mentioned in Sec. 3.1.4. *Bottom:* A frequency distribution is created by binning the data from the top. The resulting distribution is visualized as a histogram and fit with a Gaussian curve to obtain the mean μ and standard deviation σ of the relative time shift. This example shows the 83h run as shown in Table 4.1, configured to only utilize the GPS and Galileo systems, and RTK enabled. An average time-shift of $\mu = -1.18$ ns with a standard deviation or time-pulse accuracy of $\sigma = 3.41$ ns is observed.

4.3.4 Time pulse measurement campaign results

The time pulse data acquisition (DAQ) runs are conducted as outlined in Sec. 4.3.3. For an overview on the long-duration runs conducted, refer to Table 4.1. For the first couple of runs, the utilized constellations were limited to the GPS and Galileo networks. This decision was made in order to achieve the best possible position and time fix since it is generally understood that both of these networks work very well together. The run as seen in Fig. 4.9 and in the first row of Table 4.1 has a DAQ duration of 83h. The GNSS antennas with the metal base plates are located next to each other and therefore have a center-to-center distance of 15 cm. The rover is operated in the default real-time position-mode and RTK corrections are received and utilized by the rover. A time accuracy of $\sigma = 3.4$ ns is observed, way better than the manufacturer-specified time pulse accuracy of 30 ns [49].

The subsequent 55h run changes the rover position-mode to fixed, meaning the rover's position is fixed to the previously established cm accurate position. Both base and rover are now software-configured with static positions. This adjustment could improve the timing result since it eliminates the real-time position ambiguity that would otherwise be incorporated into the position calculation by the GNSS module. However, no significant impact on the σ value is observed. A clear impact would be identified with a σ change of at least 0.1 ns, judging from the typically observed variation of σ on a 0.01 ns scale.

To test if the RTK feature does have an impact on the timing capability, it is deactivated¹ for the next run lasting 95h (see Fig. 4.10). Both rover and base remain with their static position values. Surprisingly, this does not have the expected negative impact. A subsequent short run of about 1h duration is conducted, where the rover is reconfigured to real-time positioning while keeping RTK off. This short run concludes with a time pulse accuracy of 3.3 ns. Shorter runs tend to have better σ values since large-scale fluctuations of the time shift do not contribute. Therefore this short run also confirms that RTK does not seem to impact the timing result, even with the position ambiguity of the rover.

The subsequent runs involve relocating the rover's GNSS antennas as far away from the base antenna as the cable length would allow. We could achieve an antenna distance of about 4.2 m. An impact would be expected if the base and rover receivers would have different GNSS satellites in view, due to different horizons. However, this is not anticipated for base-rover-distances well below 30 km. As predicted the time accuracy of $\sigma = 3.4$ ns remains the same (compare the 55h with the 27h or 45h runs in Table 4.1).

All previous runs have concluded with a σ value close to 3.4 ns. To push the system to its limits, the fixed position-mode of the rover is exploited by deliberately providing it with incorrect position coordinates that do not correspond to the actual location of the rover antenna. This is called spoofing of the position data. As the deviation from the true position increases, it significantly impacts the GNSS modules' position and time calculation and deteriorates the time pulse measurements. The constellations being utilized are also expanded with Russia's GLONASS and China's BeiDou system, which ultimately have minimal impact on the time pulses (refer to the 91h and 45h runs in Table 4.1). Regarding the spoofed positions, we found that horizontal deviations of approximately 2 m have no impact (see 38h run in Table 4.1). However, larger horizontal deviations of around 10 m significantly impact on the σ value (see second 95h run in Table 4.1 and Fig. 4.13). In contrast, vertical deviations primarily influence the mean μ of the time-shift and only for larger values significantly affect the time-shift scatter (refer to the 169h and 129h runs in Table 4.1). These observations are consistent with findings from other studies [50].

¹successful communication of the RTK corrections were impeded by *u-center* software settings

Duration	Constellations	Distance	Rover position-mode	RTK used	μ (ns)	σ (ns)
83h	GPS/Galileo	15 cm	real-time	yes	-1.18	3.41
55h	GPS/Galileo	15 cm	fixed	yes	-0.67	3.38
95h	GPS/Galileo	15 cm	fixed	no	-2.70	3.45
27h	GPS/Galileo	4.17 m	real-time	yes	-2.01	3.35
38h	GPS/Galileo	4.17 m	fixed (1.9m wrong)	yes	-2.64	3.37
91h	all 4	4.17 m	real-time	yes	-0.53	3.50
169h	all 4	4.17 m	fixed (10m too high)	yes	26.07	3.68
129h	all 4	4.17 m	fixed (20m too high)	yes	45.14	7.26
95h	all 4	4.20 m	fixed (10m too east)	yes	4.82	13.42
45h	all 4	4.20 m	fixed	yes	-0.70	3.41

Table 4.1: Table listing the time pulse measurement campaign runs in chronological order. The columns display the corresponding duration, configuration, and Gaussian fit results for each data acquisition run.

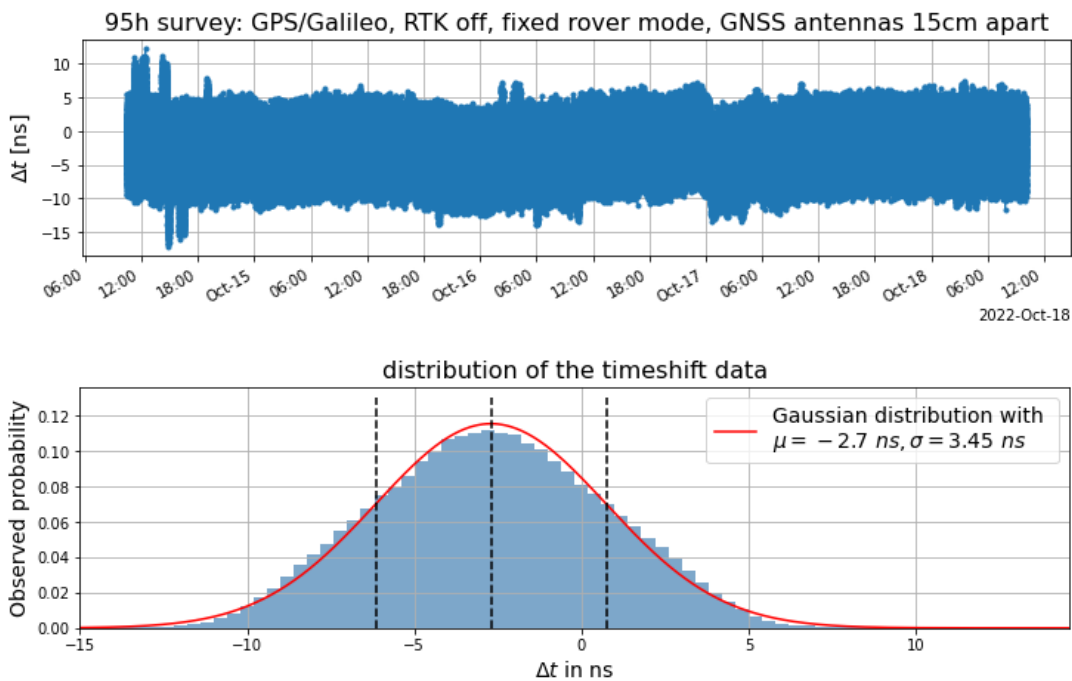


Figure 4.10: Displayed is the first 95h run as shown in Table 4.1, configured to utilize the GPS and Galileo systems, the rover receiver in fixed position-mode, and RTK disabled. An average time-shift of $\mu = -2.7$ ns with a standard deviation or time-pulse accuracy of $\sigma = 3.45$ ns is observed. The RTK feature seems to have no impact on the time pulse accuracy.

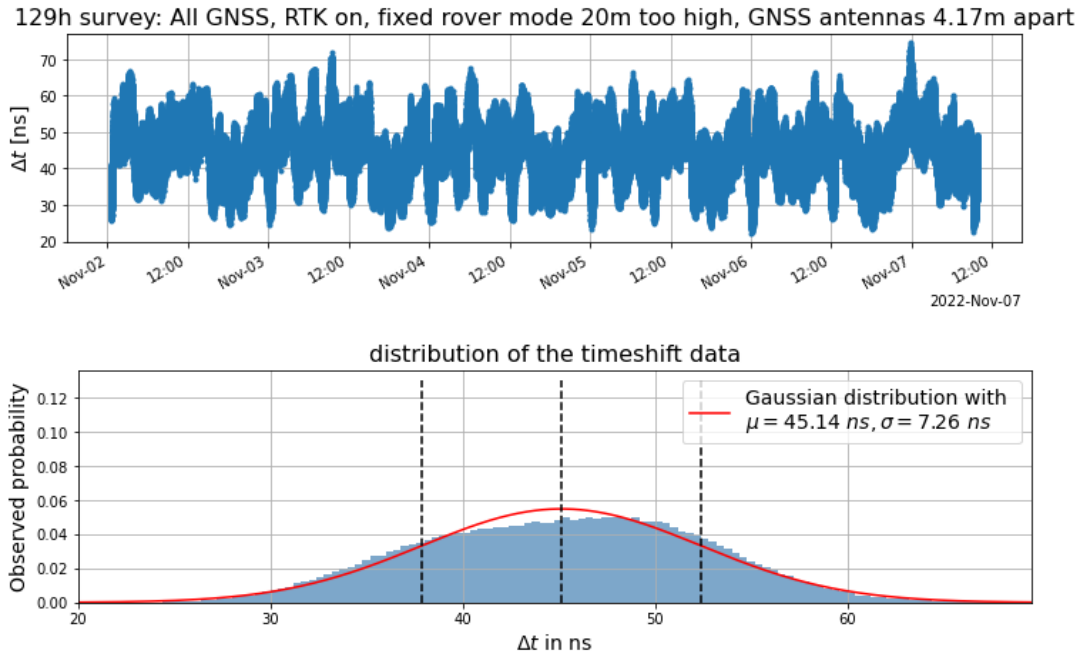


Figure 4.11: Displayed is the 129h run as shown in Table 4.1. It is configured to utilize the GPS, Galileo, GLONASS, and BeiDou systems, and the rover in the exploited fixed position-mode. Deliberate spoofing of the rover position by 20m above the true location. An average time-shift of $\mu = 45.1 \text{ ns}$ with a standard deviation or time-pulse accuracy of $\sigma = 7.3 \text{ ns}$ is observed.

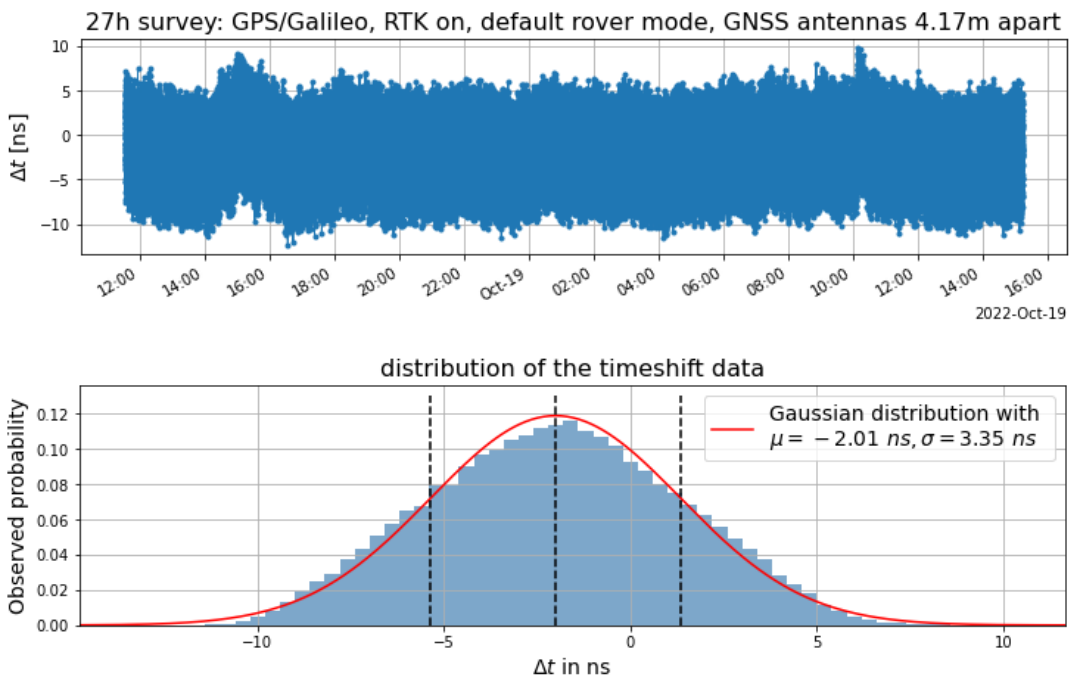


Figure 4.12: Displayed is the 27h run as shown in Table 4.1, configured to utilize the GPS and Galileo systems, the rover receiver in the default real-time position-mode, and RTK enabled. An average time-shift of $\mu = -2.01 \text{ ns}$ with a standard deviation or time-pulse accuracy of $\sigma = 3.35 \text{ ns}$ is observed. This is the best time-pulse accuracy observed during the long-term runs.

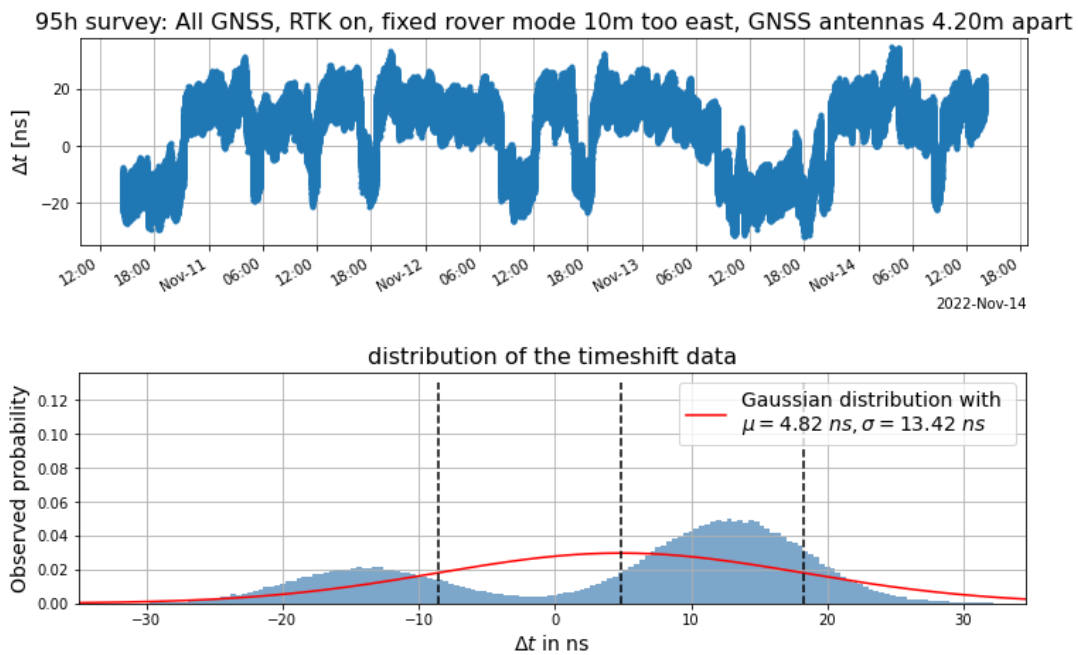


Figure 4.13: Displayed is the second 95h run as shown in Table 4.1. It is configured to utilize the GPS, Galileo, GLONASS, and BeiDou systems, and the rover in the exploited fixed position-mode. Deliberate spoofing of the rover position 10m to the east of the true location. An average time-shift of $\mu = 4.8$ ns with a standard deviation or time-pulse accuracy of $\sigma = 13.4$ ns is observed. However, the Gaussian fit is questionable here since the underlying distribution seems to consist of two normal distributions. The left distribution can be fit with $\mu = -13.7$ ns and $\sigma = 5.5$ ns. The right distribution can be fit with $\mu = 12.9$ ns and $\sigma = 5.5$ ns, see Appendix Fig. B.13. We speculate there were two competing position solutions, given our spoofed position.

4.4 Further discussion and discarded testing possibilities

The previous Sec. 4.3.4 presented that despite achieving centimeter-level relative location accuracy, the obtained relative time accuracy did not surpass 3.4 ns. There seemed to be potential for a much better time accuracy since a cm-level accuracy would require about 0.1 ns of time synchronization, based on the speed of light. Conversely, a relative time accuracy of 3.4 ns implies a positional accuracy of only 1 m, rather than the observed 2 cm. In this section, potential explanations for this finding are discussed, as well as alternative approaches and ideas that we considered to improve the timing measurements.

One possible explanation for the observed discrepancy assumes limitations in the RTK algorithm: For example, it may prioritize positional accuracy on human time-scales over sub-ns time synchronization. This notion aligns with our observation that there is little mention of temporal accuracy in the RTK literature. Nonetheless, we find this explanation unlikely given the fundamental need to synchronize the receivers to the GPS time on a sub-ns-level to achieve cm-level accuracy. However, to adequately investigate this possibility, a deeper understanding of the RTK algorithm and its handling of temporal accuracy would be necessary.

Another explanation posits incomplete communication of timing information: The accurate timing obtained by the RTK algorithm might not be conveyed error-free to the end interface. Specifically, we speculate that the observed time scatter might be dominated by the clock jitter from the on-chip timing oscillator. Consequently, the time pulse observations may not reflect the precise calculations of the rover receiver in RTK mode but instead represent the oscillator's jitter. This leads to the measured time accuracy being worse than the true capabilities of the algorithm. We consider this or a similar limitation to be the most likely explanation. However, to confirm this explanation, or to determine if other factors are at play, further investigation and analysis would be necessary.

An optimization we considered in order to enhance the timing accuracy involves conducting a more accurate survey-in for the base station's absolute position. This is because errors in the base station's position impact RTK corrections and, subsequently, the accuracy of the rover's relative position and time solution. The base survey-in utilized in this study has a software-reported accuracy of 11 cm, which leaves a bit of room for improvement. Ideally, so-called control points established and maintained by geodetic surveying agencies and organizations offer cm-level accuracy and are used to achieve the best accuracy and to validate GNSS equipment. Such a control point, located approximately 9 km from the KIT Campus Nord office building, was identified[51]. A radio connection from Campus Nord to that location for the RTK system used in this study seems feasible, enabling the establishment of an equally accurate control point at Campus Nord. However, as the last measurement runs in the previous section revealed, the 3.4 ns timing accuracy was not substantially affected by spoofed rover positions within a few meters of deviation. Therefore, it is reasonable to assume that this cm-optimization would not affect the timing result. Besides, when chasing sub-dm-accuracy using control points, the compatibility and details between the WGS84 and ETRS89 coordinate systems might limit the accuracy to the decimeter-scale anyway (see Sec. 3.1.5).

Another potential optimization we considered involved replacing the *ZED-F9P* modules, which specialize in positioning (as indicated by the 'P' in the product name), with the *ZED-F9T* version, tailored for timing applications (as suggested by the 'T' in the name). Whereas the P-chip has a rated time pulse accuracy of 30 ns the T-chip is rated for 5 ns in absolute and 2.5 ns in differential mode[52]. This possibility was discussed with colleagues from the University of Siegen[53], who have access to the *ZED-F9T* module and conducted a similar study[54]. We did not go with the T-chip from the start, because it was not

available as part of a ready-made RTK kit. After consultation with ARDUSIMPLE, the board sockets are compatible with both versions of the U-BLOX module. Therefore, in principle, de-soldering the P-chip and soldering the T-version onto the RTK board should work. However, given that the limiting factor for timing accuracy might be the aforementioned clock stability, rather than the RTK feature, we speculate that the T-version might not enhance the current results. This conclusion is also motivated by the fact that the timing accuracy results from Siegen, where the T-version was deployed, are consistent with our results. And according to the T-chips' data sheet a time pulse jitter of ± 4 ns is in fact expected. Moreover, the soldering process poses a risk of damaging the boards or chips, further discouraging this option.

In the Siegen study[54], a standalone *ZED-F9T* timing module was used, mounted on a custom motherboard developed by the Electronics Development Laboratory within the Department of Physics at the University of Siegen. This motherboard supplied power, facilitated USB connectivity, provided RF-clock amplification, and therefore served as a solid interface for both a PC and an oscilloscope. Although our own setup may seem more rudimentary in comparison, lacking a time pulse amplifier, our results closely matched those of our colleagues. One notable advantage we had was our location: we had an unobstructed rooftop location with a permanent power source. In contrast, the University of Siegen team initially had to study their system's positioning performance and accuracy at a less-than-ideal antenna location before relocating to a more suitable remote setting for the precise time pulse measurement. Although there, they were time limited to 6 hours by a portable power source. Our final findings, which show a time pulse accuracy of 3.4 ns, are in close alignment with their final measurement of 3.3 ns. But recalling the remarks in Sec. 4.3.4 we actually also measure 3.3 ns for runs of similar duration, so our results are in fact fully compatible.

Given that a sub-nanosecond timing accuracy with GNSS methods seems to be currently out of reach, our focus has shifted towards exploring a more promising approach for nanosecond-level time synchronization. Namely, the use of a radio beacon transmitter for cosmic-ray radio measurements. This approach more closely aligns with our overarching goal of making radio interferometry more viable, particularly in achieving the necessary 1 ns of relative time accuracy. Additionally, the beacon system offers the benefit of requiring no modifications to the electronics that read and tag the GPS timestamps to the recorded event traces. This makes it an especially attractive option for experiments like the Pierre Auger Observatory and its upcoming Radio Detector array.

5 Data analysis of the AERA Reference Beacon Transmitter

This section discusses the data analysis we conducted on the AERA reference beacon transmitter signals. The motivation behind the analysis is two-fold: to acquire an understanding of the system’s current performance and to explore the feasibility of a potential future expansion. Sec. 5.1 outlines the dataset and the software tools used in this study. Sec. 5.2 investigates the real-world dependence of the beacon’s signal strength on receiver distance, an important piece of information for assessing a larger-scale beacon transmitter installation. The subsequent Sec. 5.2.1 to 5.2.7 delve into specific aspects of the analysis, including pre-processing steps, dataset exploration, and data fitting. In Sec.5.3, we estimate the required distances for potential beacons in Auger’s Radio Detector (RD). We conclude by summarizing and discussing our findings, with directions given for future research in Sec. 5.4.

5.1 Description of the data and software

The dataset under investigation is archived in `.root` files, conforming specifically to the Radio AERA root data structure. ROOT[55] is an open-source object-oriented data analysis C++ framework developed by CERN in the 1990s. It continues to serve as an integral part of collaborative analysis software used by physicists, particularly in the domains of particle research and large-scale statistical data analysis. The dataset we have access to is comprised of periodic radio measurements taken between April 2013 and December 2019. AERAs data acquisition initially involved periodic triggering every 10 s before July 2014. Afterwards, this interval has then been changed to 100 s. Each `.root` file in the dataset contains the event data of one day. Every event object contains the data from all AERA stations, which have two measurement channels each (for the North-South and East-West polarization of their antenna).

For the raw data read-out and pre-processing, we utilize the Pierre Auger Observatory’s *Offline* C++ framework[56][57]. The *Offline* framework’s general architecture is built around three principal parts: a collection of processing modules that can be flexibly configured and sequenced through instructions specified in XML files, an event data model through which the modules can communicate data to one another, and a detector description which informs the modules of the observatory’s (possibly time-dependent) configuration and performance as well as atmospheric conditions[56].

The post-processing and main data analysis steps of this thesis are done using `python 3.10`, employing the `numpy`, `scipy`, `uproot` and `matplotlib` libraries for computational and visualization tasks.

5.2 Analysis of the signal attenuation as a function of distance

This section aims to investigate how the beacon signal strength decreases as a function of distance from the AERA beacon transmitter. In an ideal situation involving an isotropic signal propagation, power P decreases with the square of the distance ($P \propto 1/r^2$), known as the inverse square law. Since power is proportional to amplitude squared ($P \propto A^2$), a linear decrease in amplitude ($A \propto 1/r$) would be expected. However, real-world factors such as ground attenuation may cause a faster decline in signal strength. The goal is to quantify this relationship, as understanding it is crucial for assessing the feasibility of extending such a signal system to the entire Pierre Auger array. This extension would go beyond the scope of the AERA field to include the currently being deployed RD.

The data selected for this analysis is mostly from May 8th, within each of the years 2014 to 2019. Some other dates were tested during trials. The months of June 2018 and December 2018 are also primarily processed. There are up to 860 events per day to provide a statistically robust representation of the beacon's signal performance.

5.2.1 Pre-processing in *Offline*

In this section, we discuss the module sequence we use for pre-processing the data. Our application is largely based on the Example Application `RdCalcBeaconRefPhases` found in the `doc` folder of our *Offline* installation¹. The content of our `ModuleSequence.xml` file, defining the sequence with which the modules are run, is the following:

```
<sequenceFile>
  <enableTiming/>
  <moduleControl>
    <loop numTimes="unbounded">
      <module> EventFileReaderOG           </module>
      <module> RdStationRejector           </module>
      <module> RdEventPreSelector           </module>
      <!-- Modified version to ensure a minimal time separation of events -->

      <module> RdChannelADCToVoltageConverter </module>
      <module> RdChannelSelector           </module>
      <module> RdChannelPedestalRemover     </module>
      <module> RdChannelResponseIncorporator </module>
      <module> RdChannelUpsampler           </module>

      <module> RdStationPositions           </module>
      <!-- own module to write out positions and distances -->
      <module> RdChannelBeaconSignalExtractor </module>
      <!-- Modified version to write out amplitudes -->
      <module> RdChannelDebugWriter         </module>
      <!-- Modified version to write out averaged spectrum -->
    </loop>
  </moduleControl>
</sequenceFile>
```

¹version v3r99p99, GIT revision number: bc88f7bbf, as of 22/08/2023

The first standard module reads the event file. Then data is pre-selected according to standard exclusion options. For instance, we set that only events of the type *periodic trigger* are accepted. Problematic stations known for producing faulty data are also excluded using the `RdStationRejector` module. This includes in particular stations with NIKHEF digitizers which exhibited illegal ADC values in their time traces. Additionally, a `BadPeriodDatabase` is consulted to exclude AERA stations for known time periods where they exhibit malfunctions or poor data quality. We made modifications to the `RdEventPreSelector` module to enforce a minimum time gap between processed events. This gap was set to 98 seconds, allowing us to skip 9 out of 10 events triggered every 10s in data collected before July 2014. This ensures that the remaining events are spaced 100s apart, consistent with data from all other years. The time gap can be adjusted as needed via the XML configuration files.

The subsequent five modules, starting with `RdChannelADCToVoltageConverter`, are standard components required for the `RdChannelBeaconSignalExtractor` module to accurately process the data. The remaining modules, which will be discussed in detail in the following sections, were mainly modified to export data in simple text-based `.dat` files for further analysis using `python`.

5.2.2 Station positions and distance calculation

We wrote the user module `RdStationPosition`, inspired by the `RdTimeCalibration` module found in the aforementioned Example Application `RdCalcBeaconRefPhases`. Its purpose is to fetch the station positions as well as to calculate the respective distance to the beacon transmitter and write the obtained values to a file. This is done once while processing the first event of a run. The distance calculation utilizes the coordinate system libraries and geometry tools of *Offline*, ensuring accurate distance calculations. The coordinates are saved in the Universal Transverse Mercator (UTM) coordinates. The UTM coordinate system is a widely used method of geospatial mapping that divides the Earth into longitudinal zones and latitudinal bands. Within each zone/band combination, coordinates are expressed in meters, making the system highly intuitive and practical for local and regional mapping. This is due to its zone individual favorable map projection, which allows for an almost Euclidean coordinate system locally. This means that within each zone, distances and angles can be calculated using simple Cartesian mathematics, as opposed to the more complex trigonometry required by the global latitude and longitude system.

The spatial arrangement of the stations and the beacon is illustrated in a scatter plot that serves as a map, as shown in Fig. 5.1. This visual representation aids in understanding the beacon's location at the Coihueco site relative to the AERA stations. The map also helps to identify station IDs that closely share the beacon's Northing value, as indicated by the horizontal red dashed line in Fig. 5.1. Given that each station's channel 1 is North-South polarized, channel 1 antennas are expected to best capture signals from the beacon, as mentioned in Sec. 3.2. This is consistent with our data findings (see Fig. C.15). Additionally, these stations are positioned directly behind one another when viewed from the beacon's perspective, which makes them prime candidates for initial amplitude over distance fits.

The map also allows for the annotation of station information beyond just their IDs. For instance, it can display the calculated distance of each station to the beacon, or the estimated angle between channel 1 antennas and the beacon, see Fig. 5.2. Such annotations are valuable for cross-checking calculations.

To provide other comprehensive visualizations, the map can be augmented with a color dimension. This allows for the representation of additional data, such as the relative elevation of each station to the beacon, as illustrated in Fig. 5.3, or the average signal amplitude at each location, as detailed in Fig. 5.6 of Sec. 5.2.4.

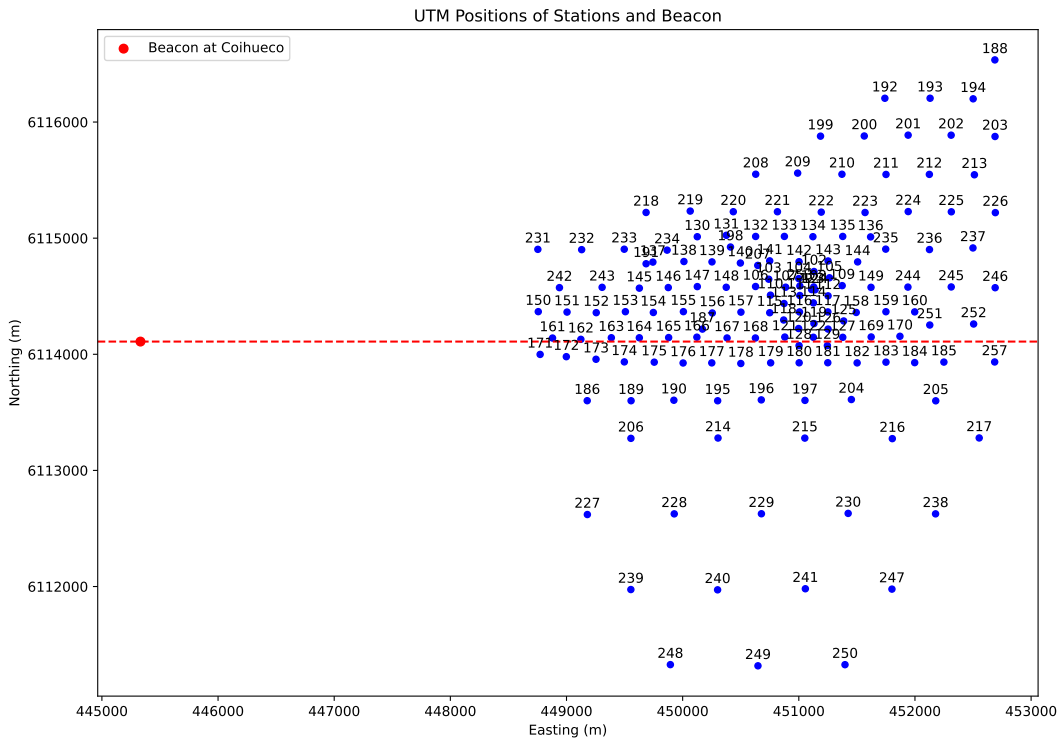


Figure 5.1: AERA station map, annotating station IDs. UTM coordinates are of Zone 19 Band H.

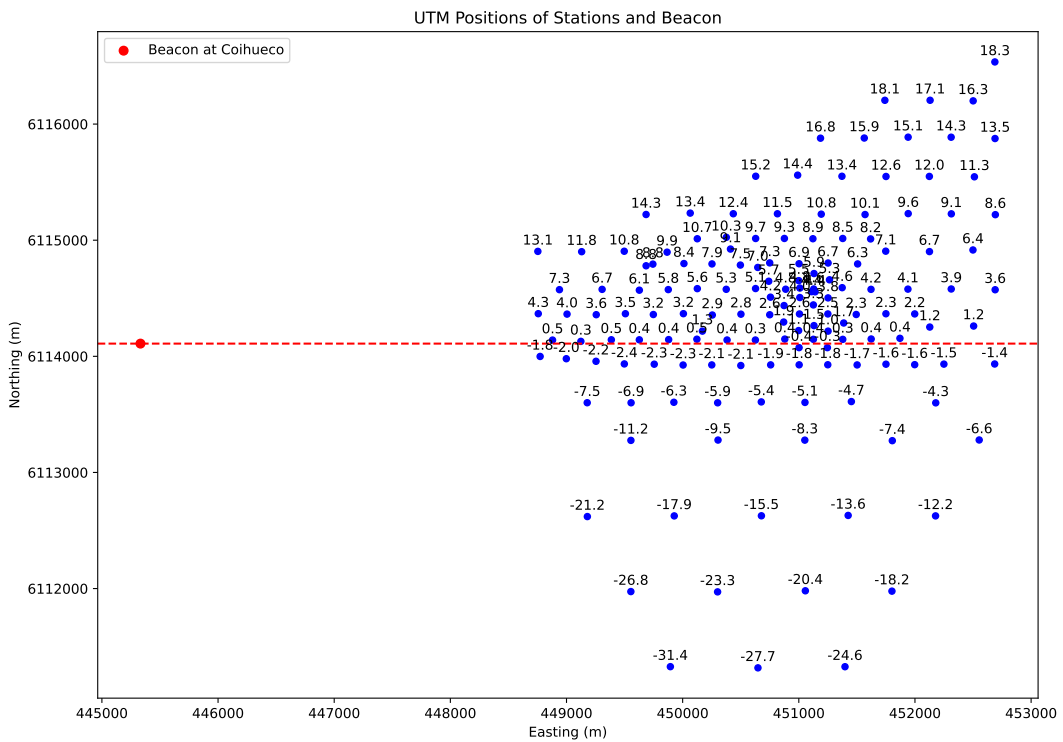


Figure 5.2: AERA station map, annotating the antenna angles ϕ in degrees to the beacon transmitter. UTM coordinates are of Zone 19 Band H

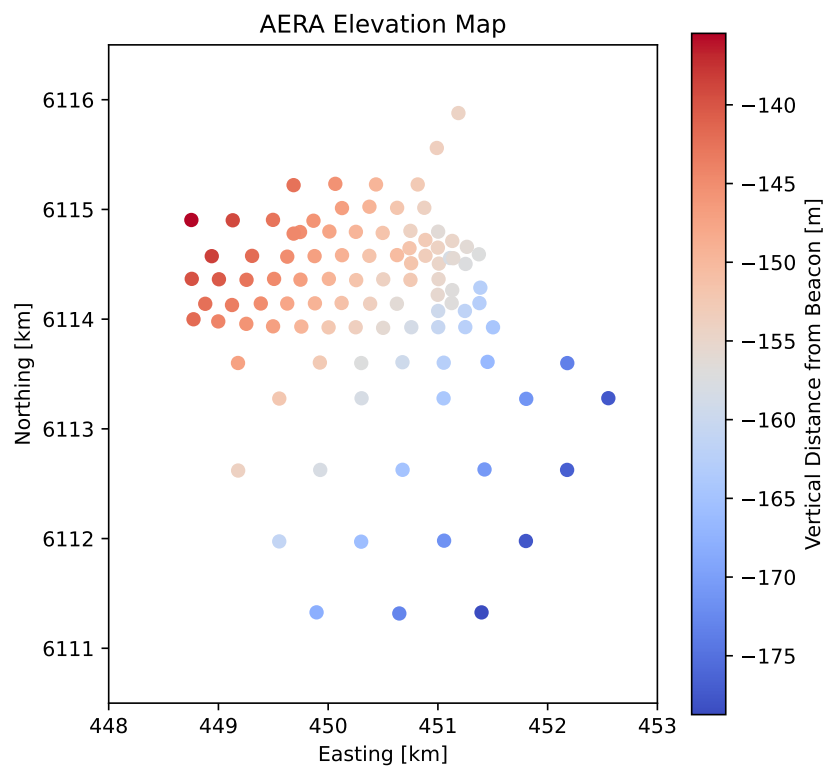


Figure 5.3: AERA elevation map relative to the beacon height. We see that the stations are located on a slope. The stations are positioned at elevations ranging from about 135 m to 180 m below that of the beacon.

5.2.3 Event spectra and average spectra

During the pre-processing using *Offline* a frequency spectrum for each event, in each station and each channel is generated from the recorded event traces, as seen in Fig. 5.4. In these spectra, the amplitude values at a beacon frequency are looked up and written out to the .dat file. This value corresponds to the amplitude of this frequency. This procedure is done by the modified `RdBeaconSignalExtractor` module. Later in `python`, we take the mean of the amplitudes across all events of a day and also calculate the associated standard deviation. We do this for each station, beacon frequency and channel contained in the .dat file.

Additionally, we also modified the `RdChannelDebugWriter` module so that it takes the mean of the whole spectrum, and writes it out to a .root file. It contains all stations with 2 channels each, with their respective average spectrum of the day, see Fig. 5.5. We use this data for consistency checks and debugging.

5.2.4 Amplitude plots

To gain initial insights into the amplitude data, we visualize it for multiple sample days on a detector map, as shown in Fig. 5.6. We first notice the apparent inactivity of the beacon on May 8th, 2017. The data for this date shows uniformly low magnitudes across the AERA array, compared to the other days. This observation is further corroborated when we examine the average spectrum of that day in Fig. 5.7, with the absence of the four distinct beacon frequency peaks. Private communications confirmed that the beacon was indeed non-operational for four months in 2017, a fact observed by colleagues Diego Correia and Rogerio de Almeida who are currently preparing their Average Spectral Density report for an upcoming GAP Note publication.

Furthermore, we also notice that the LPDA stations have lower amplitude values compared to those with Butterfly antennas. This is also visible in amplitude over distance plots, see Appendix Fig. C.16. The deployment locations of these LPDA stations can be recalled from Fig. 2.7. This amplitude difference is expected to arise due to different detector responses, which have not been accounted for in our current pre-processing pipeline. For the time being, these LPDA stations will be excluded from further analysis. However, it should be feasible to determine the offset factor by analyzing multiple days of data. As this factor is expected to be consistent across all measurements. Once identified, it can be applied universally to all measurements of this detector type.

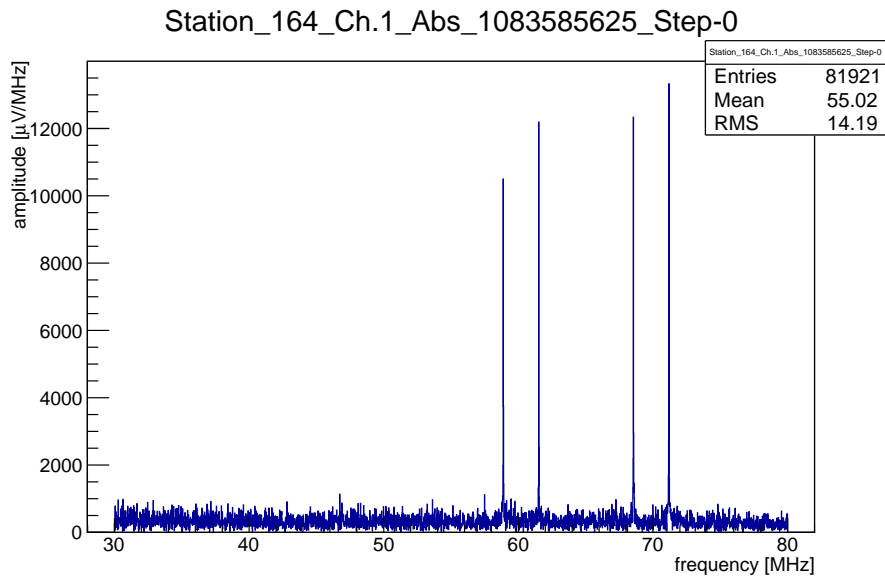


Figure 5.4: ROOT plot showing an example spectrum of station 164 from a periodic trigger event from May 8th, 2014

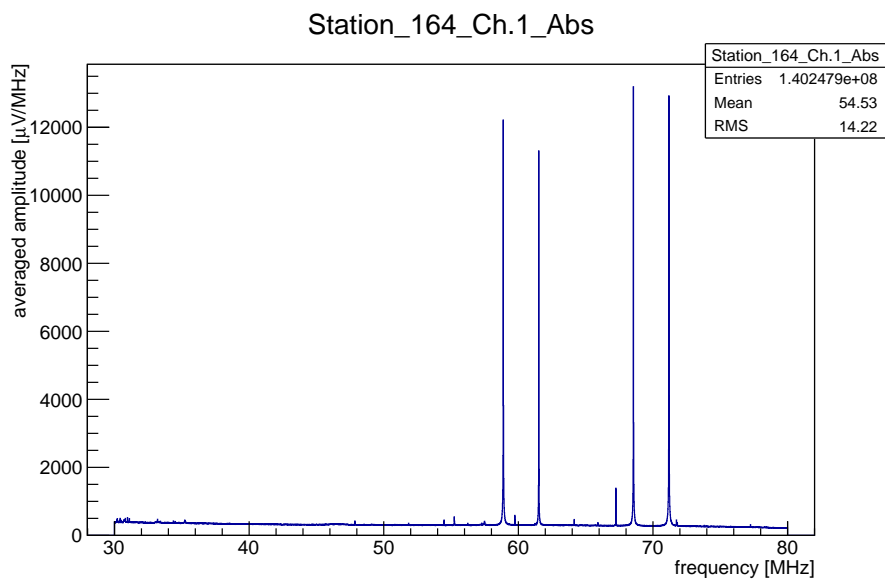


Figure 5.5: ROOT plot showing an example average spectrum of station 164 from the 856 periodic triggered events on May 8th, 2014

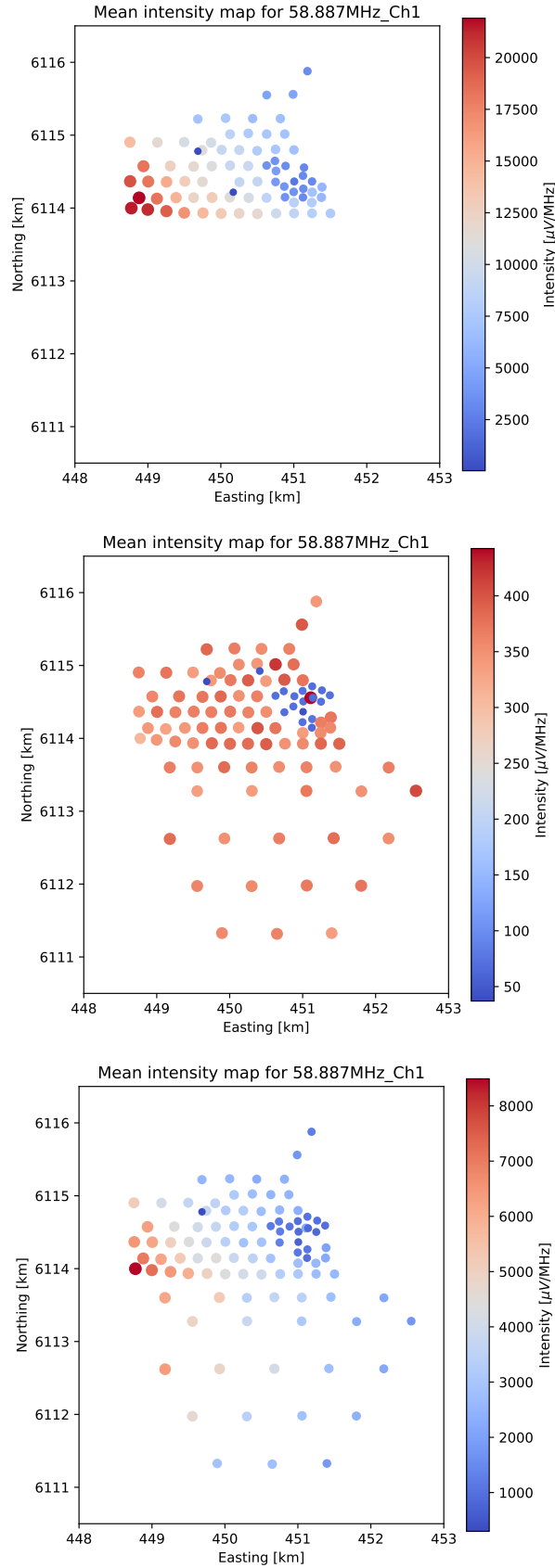


Figure 5.6: Intensity maps for the frequency of 58.887 MHz in channel 1 on May 8th of 2014 (top), 2017 (middle) and 2018 (bottom). Notice the changed color scale in the middle plot.

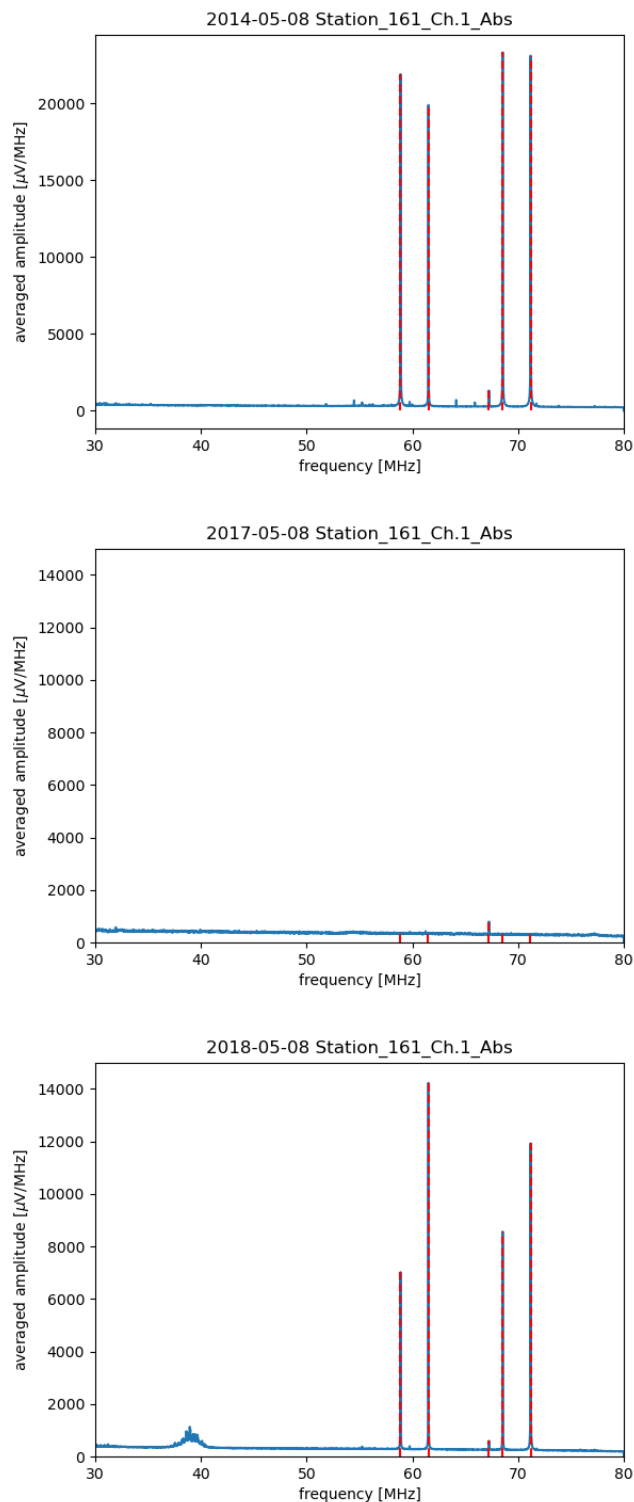


Figure 5.7: Averaged spectra at station 161 in channel 1 on May 8th of 2014 (top), 2017 (center) and 2018 (bottom). The four beacon frequencies and the carrier frequency of a local TV station are marked with vertical red lines.

5.2.5 Fit methodologies

To find the relationship between amplitude and distance to the beacon, we assume the Power Law function $y = a \cdot x^b$. We fit this function to the data points, using their standard deviations as the error term. This fitting is conducted on the amplitude data for each beacon frequency reading from the .dat files, as outlined in Sec. 5.2.3. The parameter of interest is b , which we will also refer to as the spectral index.

Our analysis targets channel 1 data, where the beacon signal is most pronounced. Although a straightforward fit to the channel 1 data provides initial insights, additional data processing and filtering could potentially refine the fit. For this purpose, we continue our analysis using data from May 8th, 2018, as a representative sample to explore alternative fitting methodologies. Example fit plots are shown in Figures 5.8 to 5.10, and a comprehensive visualization of the b parameter fit results across the different fitting methodologies is presented in Fig. 5.11.

Fits using channel 1 data directly

First, we only use the stations that closely share the beacon's Northing value as data points for this initial fit, with results displayed in Fig. 5.8. Across all four frequencies we obtain a value of $b = 2.11$ with an maximal statistical error of ± 0.19 in case of the 58.887 MHz frequency. In an effort to enhance the statistical robustness of our analysis, we now lift this restriction and fit all eligible stations, with fit results as seen in Fig. 5.9. The b parameter values now range from -1.73 to -2.19 , even though each fit's statistical errors on b got smaller, compared to the previous fits.

Fits adjusting channel 1 with angle ϕ to the beacon location

Given the relative positions of the stations to the beacon, it is expected that stations located further off-axis would record lower amplitudes of the beacon signals since the North-South polarized channel 1 antenna is no longer oriented perpendicular to the line-of-sight to the source. To account for this, we adjust the data points by dividing them with the $\cos \phi$, where ϕ represents the angle to the beacon position. We calculate this angle for each station based on their UTM coordinates relative to the beacon. For reference, these calculation results are annotated in Fig. 5.2. After making this adjustment, the range of b values now spans from -1.70 to -2.17 . So no significant effect on the fit results was observed with just this one adjustment.

Fits adjusting channels 1 with channel 2 data

We also explored the idea of integrating data from channel 2 into our analysis. This consideration is based on the notion that the beacon's power would spill over into channel 2 if the antennas are not perfectly perpendicular to the line of sight. To account for this, we square the amplitude values from both channels, sum them together to arrive at the total power, and then take the square root to obtain an amplitude value for comparable fitting. However, we observe no significant changes in the results. This suggests that channel 2, which is largely devoid of the beacon signal, has minimal impact on the overall outcome.

Fits after cutting antennas based on angle ϕ to beacon

For upcoming fits we keep using the cosine correction (unless stated otherwise), but additionally impose restrictions on the stations participating in the fit, by filtering out stations or rather antennas that are too far off axis off the beacon direction. While

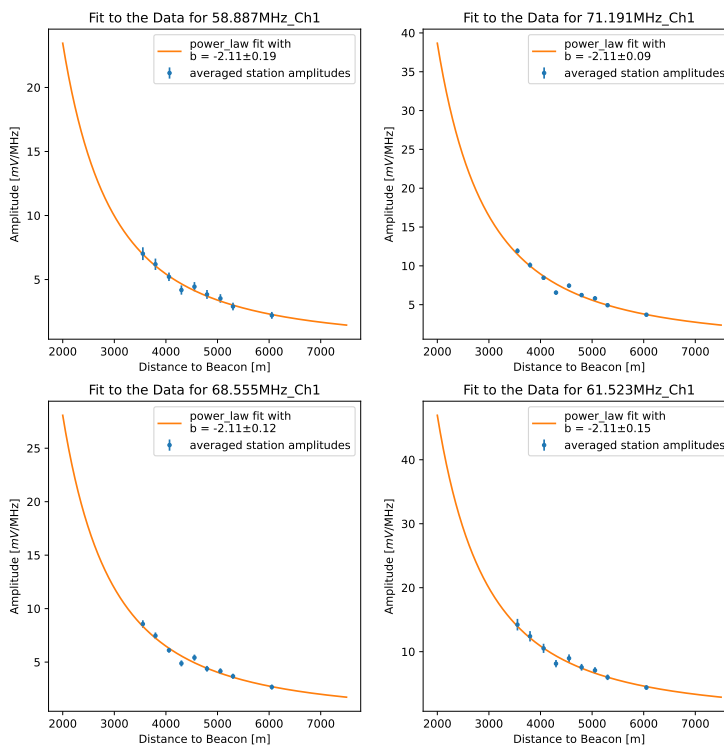


Figure 5.8: Power Law fits for all four beacon frequencies of the unadjusted channel 1 data, with only stations that closely share the beacon’s Northing coordinate, day 2018-05-08.

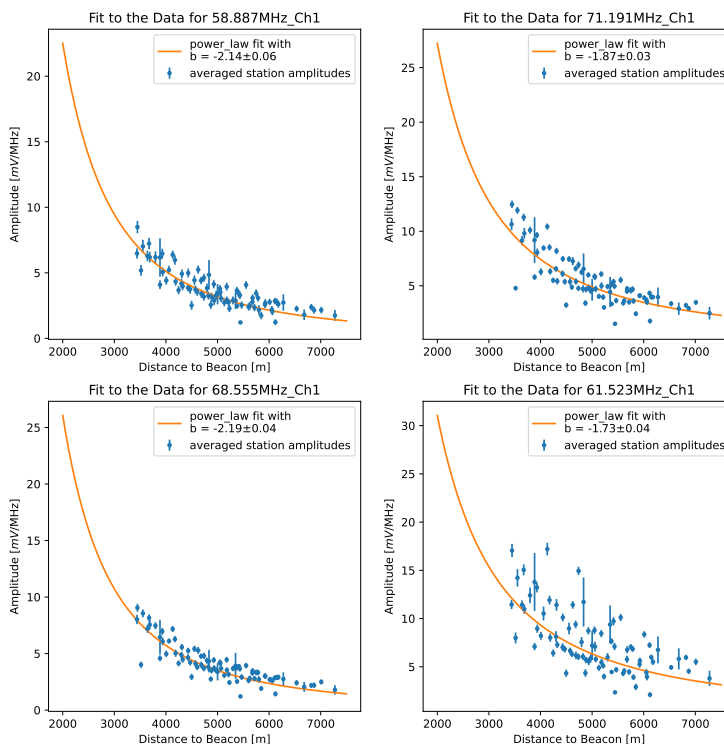


Figure 5.9: Power Law fits for all four beacon frequencies of the unadjusted channel 1 data, day 2018-05-08. The antennas are located 3.5 to 7.5 km away from the beacon.

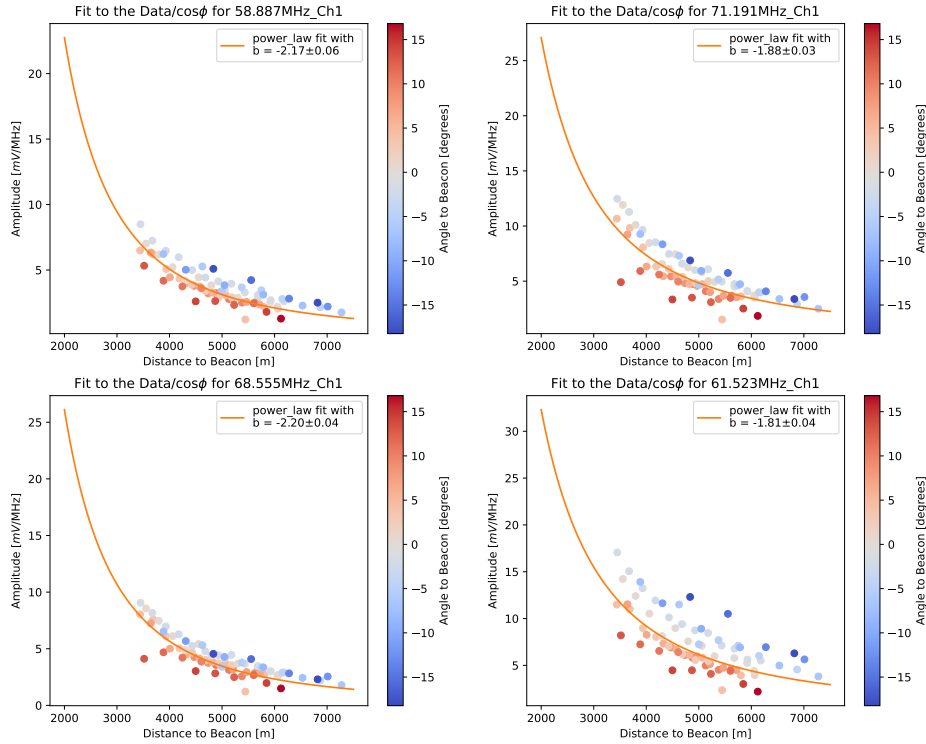


Figure 5.10: Power Law fits for all four beacon frequencies of channel 1 data corrected with $\cos \phi$ and a $|\phi|$ cut of $< 20^\circ$, day 2018-05-08.

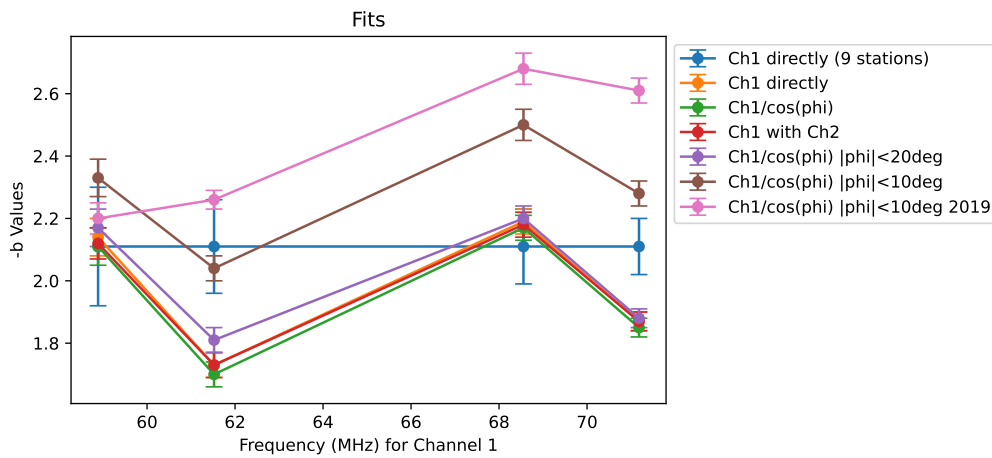


Figure 5.11: Visual compilation of all the fit results of the different methodologies tried so far. The spectral index b varies between -1.7 to -2.7.

redeveloping the fit script, we also change the visualization of the data points; to make it clearer which station has which angle to the beacon, we color code the points, see Fig. 5.10.

Initially only allowing absolute off-axis angles $|\phi| < 20^\circ$, we indeed notice that the data points located furthest away from the fit function are excluded, resulting in a narrower distribution of points around the function. This effect is even greater when imposing a more restrictive cut with $|\phi| < 10^\circ$. The resulting values for b changed noticeably, when cutting antennas this way. Since this seemed promising, we also checked the fit results of the same date, but one year later in 2019, see Fig. 5.11.

Another puzzling observation from our fit plot Fig. 5.10 concerns the amplitude dependence on the angular positions relative to the beacon. Specifically, stations positioned with positive angles to the beacon (northward) tend to measure smaller amplitudes, while those with negative angles (southward) record larger amplitudes; although they have the same distance from the beacon. However the attempt to correct the orientation of the AERA antennas using the factor of $1/\cos\phi$ is not sufficient to neutralize these angle dependent effects. This suggests that other factors are at play, necessitating further investigation.

5.2.6 Observed angle dependence of the signal amplitudes

Two possible explanations warrant consideration: First, the beacon transmitter antenna's orientation might not be strictly east-bound. A slight orientation to the south might explain the observed effect. To study this, we introduce another parameter we will call α . It describes the potential misalignment of the beacon antenna from the ideal east-bound orientation (North-South polarization) and redefines the axis from which ϕ for the cosine correction is measured. A helpful illustration for α is given in Fig. 5.12. By varying α and observing the effect it has on the colored data points – and thus crucially the statistical error on the fit – we determined a best value of $\alpha = -3^\circ$, see Fig. 5.13. With this choice of α the angle dependence seems to vanish the most, although not entirely for all frequencies. This outcome could also potentially be related to the orientation of the AERA antennas, which are aligned with geomagnetic north rather than geographic north. When the Butterfly antenna stations were deployed in 2013, the geomagnetic declination at AERA was at about 2.4°E , and at initial deployment of AERA in 2011 it was 2.7°E – values calculated with [58] utilizing the International Geomagnetic Reference Field (IGRF)[59] model. This aligns almost exactly with $\alpha = -3^\circ$.

The second possible explanation for the observed angle dependence of the amplitudes is, that the terrain's topography could be influencing the signal propagation. For instance, if a portion of the array is situated at a significantly lower elevation, one could experience reduced ground absorption even with an equivalent distance from the beacon. Looking at Fig. 5.3 the elevations northbound are indeed higher and could thus contribute to the observed higher signal attenuation for the northward antennas. To scrutinize this further, we analyzed the behavior of the b parameter depending on the ϕ position of the antennas, as compiled in Fig. 5.14. However, we found no consistent linear trend across varying angles; in fact, for larger angles above $\phi = 5 \pm 5^\circ$ (represented in orange and blue in Fig. 5.14) the b fit values actually decrease again.

Ultimately it is likely that both antenna alignment and terrain topography are contributing factors that need to be considered in a more integrated manner to fully understand their total effects on signal propagation. Additionally, there could be other external variables at play, which may require further investigation to comprehensively understand the observed behavior.

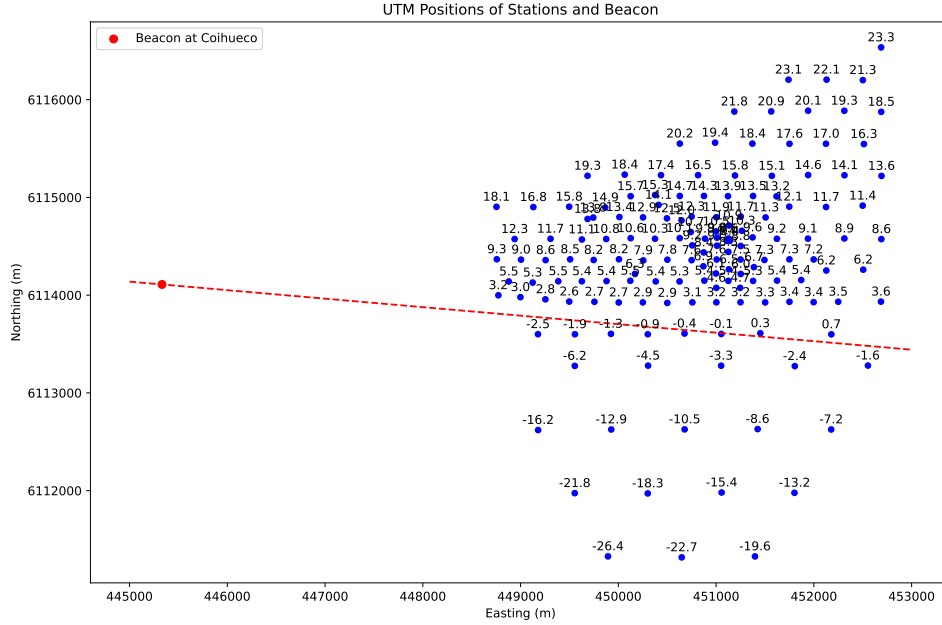


Figure 5.12: AERA Station Map illustrating $\alpha = -5^\circ$ and the resulting ϕ in degrees.

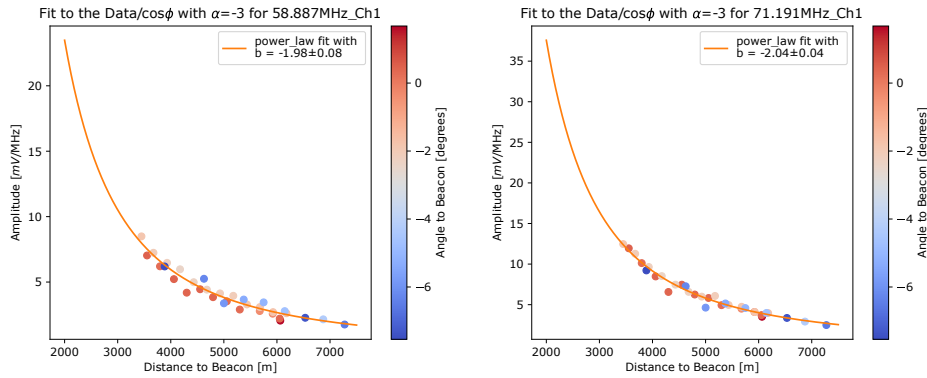


Figure 5.13: Power Law fit with $\alpha = -3^\circ$ and a $|\phi| < 5^\circ$ cut, on the 2018-05-08. In this configuration the angle dependence of the amplitude seems to mostly vanish. For a variant without a ϕ based cut, see Appendix Fig. C.17

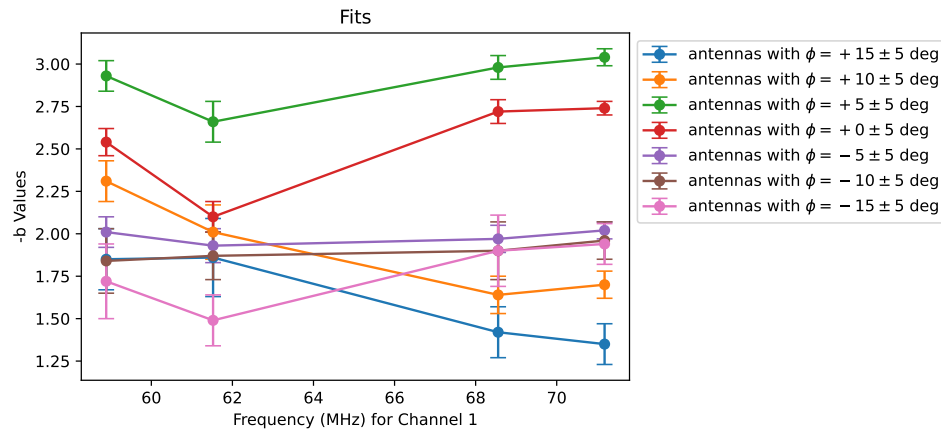


Figure 5.14: b 's behavior depending on the ϕ position of the antennas. For these fits, the cosine correction was disabled. No consistent trend – going from negative to positive ϕ 's – is visible, since the blue and orange fits have better values again.

5.2.7 Temporal variability of the spectral index

After establishing our optimal $\alpha = -3^\circ$ and our preferred cut condition $|\phi| < 10^\circ$, we extend our analysis to capture a more comprehensive view of how the spectral index b fluctuates and within what range it varies.

First, we focus on data from June 2018, with the fit results depicted in Fig. 5.15. During this month, the values vary between -1.62 and -2.67 . Second, we examined data from December 2018, half a year later. These results are illustrated in Fig. 5.16. During this month the values vary between -1.85 and -3.41 , with an anomalous value of -4.20 identified on December 4th, 2018. Upon reviewing the fit plot and average spectrum for this particular day, no obvious anomalies or errors were detected in either the fit or the data (see Appendix Fig. C.19 and C.20). This suggests that the observed value may indeed be a genuine outlier.

For December, the fit values appear notably high. It is worth mentioning that if we relax the cut condition $|\phi| < 10^\circ$, the b fit values tend to improve. Refer to Fig. C.22 in the Appendix for the December data without ϕ based cut.

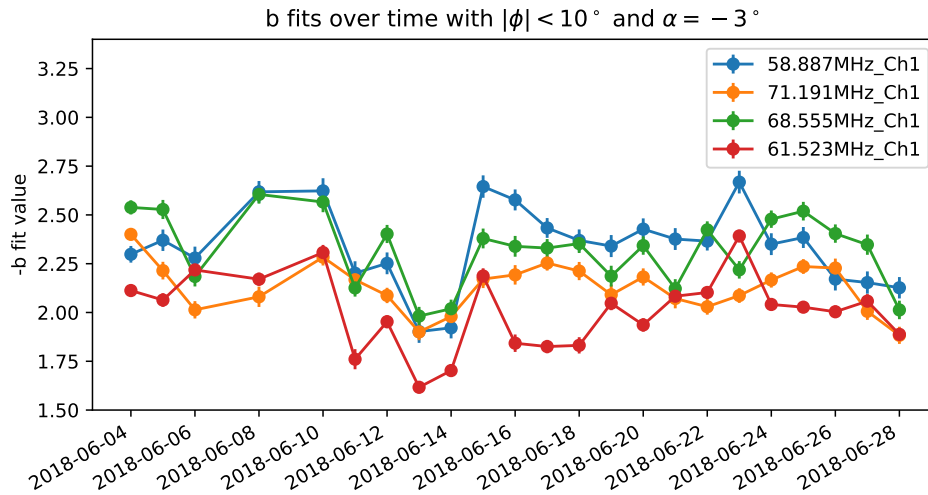


Figure 5.15: Evolution of the spectral index b over the course of June 2018.

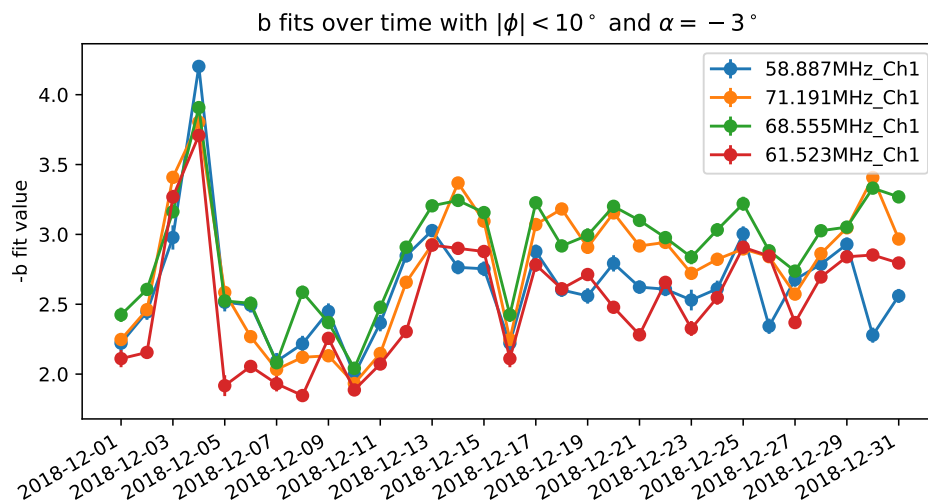


Figure 5.16: Evolution of the spectral index b over the course of December 2018.

5.3 Estimation of required RD beacon distance to array edge

To evaluate the significance of the b values, we perform a simple calculation. We start from the Power Law function

$$A(r) = a \cdot r^b \quad (5.1)$$

and aim to ensure that an RD receiver at the center of the array (approximately 30 km away from the Pierre Auger array perimeter) can receive a signal above the noise level. To be concrete, the ADC values should be 3 or 4 bits large. At the same time, the stations at the edge of the array should not saturate; meaning the ADC values must not exceed 11 or 12 bits. Depending on the chosen combination, this yields a contrast ratio k between both locations of 128 (7-bit), 256 (8-bit), or 512 (9-bit). Let us consider the equation

$$\frac{A(r_0)}{k} = A(r_1), \quad (5.2)$$

where the beacon is at $r = 0$, the edge of the array is at $r = r_0$, and the center of the array is at $r = r_1$. Please refer to Fig. 5.17 for an illustration.

After simple manipulations of Eq. 5.2 utilizing 5.1 and $d = r_1 - r_0$, we find

$$r_0 = \frac{d}{k^{-1/b} - 1}, \quad (5.3)$$

where d is the distance between array center and array edge, k is the considered contrast, and b is the spectral index which characterizes the signal amplitude decay. Equation 5.3 is visualized in Fig. 5.18. Alternatively, Eq. 5.2 can be rearranged for the contrast as

$$k = \left(\frac{d}{r_0} + 1 \right)^{-b}, \quad (5.4)$$

see Fig. 5.19 for its depiction.

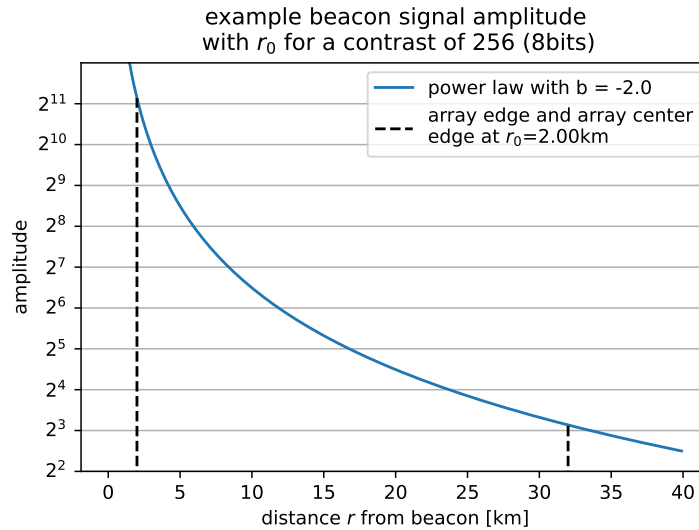


Figure 5.17: Illustration showing the locations of r_0 and r_1 . Both points are marked with vertical dashed lines and represent the array edge and array center respectively. The beacon is located at $r = 0$. The amplitude profile for $b = -2.0$ is also shown on a logarithmic scale. For this example, the difference between r_1 and r_0 is assumed to be 30 km. This leads to a beacon located 2.0 km away from the array edge. A contrast of $2^8 = 256$ between edge and center is observed.

Using these equations, we can make specific estimates. For example, with $b = -2.75$ and a desired contrast of $k = 256$ (8-bit), an RD beacon would need to be $r_0 = 4.6$ km away from the array edge, to avoid saturation of the closest stations while still being detectable at the center. This result does not seriously undermine the feasibility of RD beacons. For comparison, the AERA beacon is located 3.5 km away from the closest AERA station. However, with $b = -3.0$ and a more limiting contrast $k = 128$ (7-bit), the required distance would increase to $r_0 = 7.4$ km. While this result lies at a markedly greater distance than the existing beacon, the topography around the Pierre Auger Observatory suggests it is not entirely unattainable, see Fig. 2.4. Additional combinations can be readily inferred from the Fig. 5.18 and 5.19 or computed using Eq. 5.3 and 5.4.

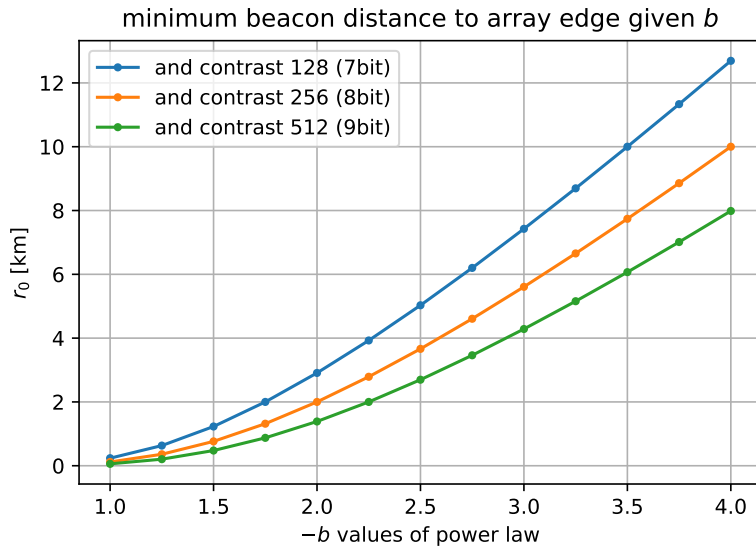


Figure 5.18: Visualization of Eq. 5.3, showing to required RD beacon distance r_0 from the array edge for different b 's and contrast scenarios. Assuming $d = 30$ km.

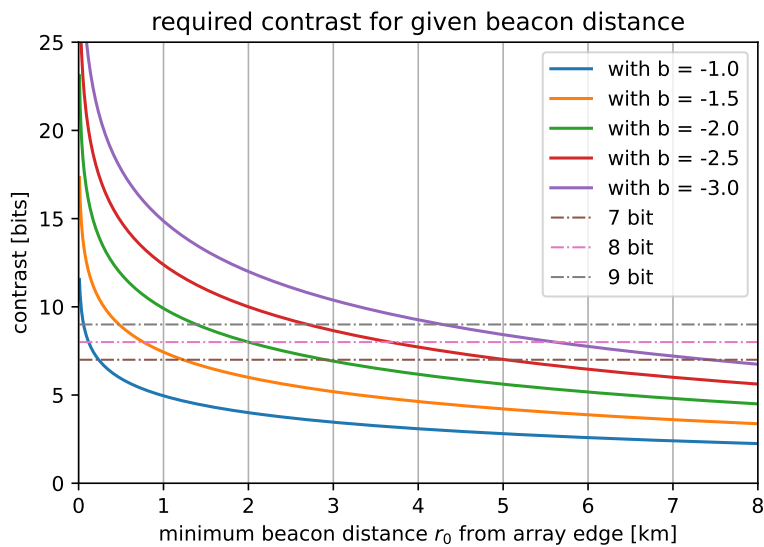


Figure 5.19: Visualization of Eq. 5.4, showing to required contrast k for different distances r_0 and b 's. Assuming $d = 30$ km.

5.4 Discussion and outlook on the beacon analysis

Our investigation into the beacons signals brings forth several key observations. On particular days or months within the dataset the beacon signal vanishes, very likely coinciding with known beacon outages. Also, the received amplitudes of the beacon are not constant. Though most variations may be explained by environmental conditions, which would impact all beacon frequencies similarly, Fig. 5.7 shows the relative amplitudes can also differ significantly. Although, between the depicted dates, there might have been a hardware reconfiguration, which resulted in these different spectra. Future studies might seek to identify the underlying causes for these variations.

Furthermore, we encountered initial challenges in obtaining good quality data suitable for fitting, depending on the choice of day and the selection of stations. We noticed outlier stations, see Fig. 5.6, with amplitude data noticeably below that of all other stations. We attributed this to them being a different station type with its detector response unaccounted for in our pre-processing *Offline* module sequence. One could also try to reincorporate these stations into our analysis, after determining the offset factor, and/or adjusting the pre-processing steps.

An alternative method to obtain the exact frequency and amplitude values from the raw data could also be considered, namely the use of the Discrete Time Fourier Transform (DTFT), rather than the standard Discrete Fourier Transform (DFT) also known as FFT. However, limitations in time prevented a thorough examination. Utilization of the DTFT method would also enable an investigation on stability of the beacon frequencies. If there is indeed an instability found, one could investigate whether this instability is a station-specific effect or a global effect. In the latter case potentially pointing to issues with the beacon hardware itself.

To quantify the relationship between signal amplitude and the distance to the beacon, we explored multiple fitting methodologies. Our results seem most reliable when we incorporate the offset angle ϕ between a station and the beacon's direction into our analysis, while also selectively excluding stations based on this parameter. Additionally, we observe that amplitude values are dependent on the angle ϕ , despite attempting to mitigate this through the use of a $1/\cos\phi$ correction factor. This led us to introduce α , representing the potential misalignment of the beacon antenna relative to geographic east. Our analysis revealed that the phenomenon is somewhat reduced with $\alpha = -3^\circ$. However, other factors, such as terrain topography and the associated signal attenuation, likely play a more significant role. Preliminary investigation into this hypothesis lead to inconclusive results, indicating the need for further studies.

Crucially, our fit results reveal considerable deviations from the ideal inverse square law. In the most favorable fit, characterized by $b = -1.60$, the signal power declines following $P \propto 1/r^{3.2}$. However, the value of b typically falls within the range of -2 to -3 , as shown in Fig. 5.15. In these cases, the power decrease corresponds to $P \propto 1/r^4$ to $P \propto 1/r^6$. Especially in the latter case, this higher-than-expected attenuation poses a challenge for any prospective expansion of radio reference beacons across the entire Pierre Auger array as part of RD. This is because caution should be exercised when placing high-power radio beacons too close to detectors, as their electronics might get saturated due to the strong signals intended for more distant stations. Estimates for the required minimum distance for beacon placement vary: they range from 1.5 km (with favorable $b = -2$ and a 9-bit contrast) to about 7.5 km (with $b = -3$ and a lower bit contrast of 7-bits), as illustrated in Fig. 5.19.

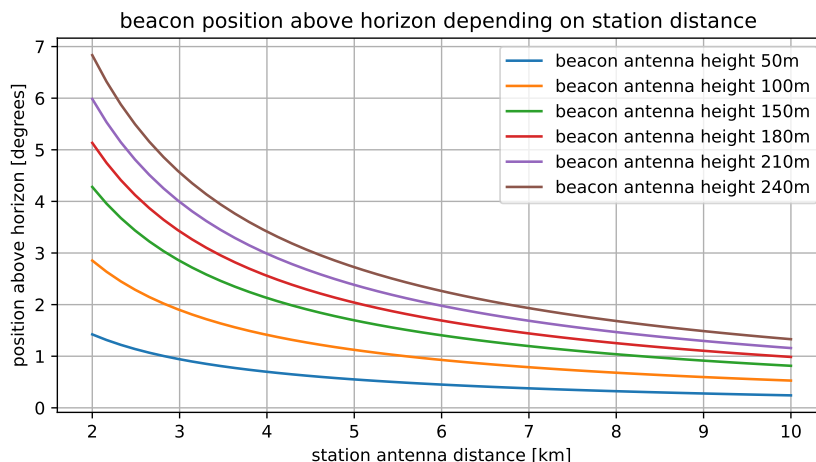


Figure 5.20: Plots of the angular elevation at which a beacon antenna appears above the horizon, as viewed from a radio station at varying distances. Curves depict how this angle changes for beacon antennas at different heights relative to a common ground level.

These constraints on minimum distance between the beacon and the closest station could conceivably be relaxed through beam forming or some other adjustments to the beacon’s radiation pattern. This would ensure that nearby stations are not exposed to the full power of the signal, while the more distant stations receive the expected signal strength. To better assess this possibility, we make a quick estimate of the required angles: Assuming a beacon height of 180 m (similar to the AERA beacon) and a distance of 5 km to the nearest detector at the array edge (for a balanced case of b and k), the detector would perceive the beacon at approximately 2.06° above the horizon (calculating on a flat-earth yields 2.04°). For stations located 30 km away from the edge, the beacon would appear at 0.13° above the horizon (0.29° with flat earth calculation). In these calculations, we assumed the Earth’s surface to be at a distance of 6371 km from the core. More of the parameter space is depicted Fig. 5.20. Considering this angular analysis, the radiation pattern would need to be designed to show a significant drop-off at a scale of 1° , for example by a factor of 2 in order to gain 1 bit of headroom in Fig. 5.18. In the worst case scenario with $b = -4$ this could knock down the required distance by around 2 km (vertical separation of the different contrast curves in Fig. 5.18). While this is likely achievable, it would probably necessitate the use of large dishes, given the 30 to 80 MHz frequency band monitored by RD. Subsequent research is warranted to more thoroughly assess the viability of this approach.

Examining Figures 5.15 and 5.16, we notice similar trends for the spectral index b of each frequency. This suggests the possibility that the observed behaviors may be correlated with specific soil characteristics, including moisture levels and vegetation. While we cannot explore this further in this study, it is also an area worth looking into for future research.

Finally, another promising avenue for further investigation is the carrier wave of a local TV station, which operates at approximately 67.25 MHz. This signal was also evident in our data, as indicated in Fig. 5.7. If this radio transmitter’s signal is detectable across the entire Pierre Auger array, it could present an intriguing opportunity to use it as a free beacon transmitter for correcting GPS time drifts.

6 Summary

In this thesis we have explored various methods for wireless time synchronization, a technology that is crucial for large-scale scientific experiments like the Pierre Auger Observatory. Achieving time synchronization with an accuracy on the order of 1 ns or less would prove invaluable, especially for radio detectors in the field of cosmic ray physics. Such a precision would enable the use of radio interferometric analysis techniques, resulting in unprecedented measurements of critical cosmic ray shower parameters, especially those of inclined showers.

The first phase of the work focused on the capabilities of modern commercially available multi-band GNSS receivers, employing newly available correction techniques such as Real-Time Kinematic positioning (RTK). These receivers promise significant enhancements in both position and time synchronization accuracy. We conducted a measurement campaign that investigated different configurations and operational modes of a GNSS RTK kit, and measured the corresponding relative time synchronization of the two GNSS modules deployed. Notably, the findings revealed that employing RTK corrections did not improve time synchronization beyond 3.4 ns. Although this performance is impressive for GNSS receivers, it does not suffice for our purpose. With the observed cm accuracy, we had expected sub-ns-accuracy, given the speed of light of approximately 30 cm/ns. We speculated that the observed time pulse accuracy was dominated by the clock jitter of the on-chip timing oscillator.

In the second phase of the work we conducted a data analysis of the AERA radio beacon reference transmitter, which is deployed at the Pierre Auger Observatory. This beacon transmitter offers an alternative method for correcting the clock drift experienced by the GNSS receivers deployed at the detectors. It is, as currently understood, the most promising approach for enabling radio interferometry. While exploring the dataset, we gained a better understanding of the system's performance. We explored the feasibility of potential future expansions by quantifying, based on empirical data, how the beacon signal strength decreases as a function of distance. We found that the received power drops very quickly, within a typical range of $P \propto 1/r^4$ and $P \propto 1/r^6$, deviating a lot from the ideal $P \propto 1/r^2$. Deploying a similar system for Pierre Auger Observatory's upcoming Radio Detector (RD), would necessitate that a similar beacon be located at around 2 to 8 km distance to the observatory's array perimeter – depending on the specific requirements. Although this appears not easily realizable, it could be within the realm of possibility. This condition might also be relaxed by using a different beacon antenna design. If these

challenges can be overcome, the 1 ns time synchronization of the radio detectors could be realized, even on the scale of the entire Pierre Auger Observatory.

Overall, this thesis has contributed to an evolving field by examining not yet fully established technologies for ultra-high-precision wireless time synchronization. Although we could not identify definitive solutions and pathways, the research has highlighted areas where limitations exist and opportunities may lie, aiding in the ongoing quest to unravel the mysteries of Ultra High Energy Cosmic Rays.

Acknowledgments

I am deeply grateful for all those who contributed to the shaping of this Master's thesis and those who enriched my time at the Institute for Astroparticle Physics (IAP) at KIT Campus Nord. For all the friends and acquaintances I made there and throughout my final year at KIT and in Karlsruhe – there are too many to name – know that your company has been both greatly appreciated and indispensable.

First and foremost among my acknowledgments is Tim Huege, for his role as supervisor and his consistent support, understanding and invaluable input. His expertise was pivotal in shaping the direction of this thesis. I also extend my gratitude to Ralph Engel for undertaking the role of first reviewer for this thesis.

I am thankful for all the stimulating discussions I partook in our regular meetings and events, whether it was with the Radio Group, the Auger Group, or the IceCube Group at IAP and beyond. Additionally, I appreciate the dialogues with my colleagues from the University of Siegen concerning our GNSS-related work, and the valuable input from Frank Schröder concerning my work on the beacon transmitter.

My sincere appreciation goes to Max Büsken and Simon Strähnz for their assistance in introducing me to the *Offline* Framework. Their expertise significantly demystified an otherwise daunting task. Also special appreciation goes to Jelena Köhler, Lukas Gülzow and Asil Meidow who have been fantastic office partners.

The opportunities to present and discuss my latest work during the AERA/RD Workshop Meeting in February 2023 and at the DPG Spring Meeting Section SMuK in Dresden in March 2023 were invaluable.

Special thanks go to Bianca Keilhauer and everyone involved in the decision to enable my volunteer trips to the Pierre Auger Observatory in August and December of 2022 for the FD Shift. These hands-on experiences were vital for my professional growth and broadened my understanding of the international scope within which experimental astroparticle physicists operate.

To my cherished friends Lukas Windstetter and Elina Merkel, your friendship has been a source of joy and strength. Thank you for being wonderful friends.

On a lighter note, I owe thanks to Noah Goehlke for his timely reminder to include this Acknowledgments section – especially when it provides an opportunity to thank him as well.

Last but not least, heartfelt gratitude goes out to my father for his unconditional love and unwavering support throughout my life and for all the endeavors I've chosen to undertake. Thank you for always being there for me.

Appendix

A table of all time pulse measurement runs

duration	base-ray	constellations	distance	communication	μ (us)	σ (us)
1,9 h	250cm	all	next to	std corr	-0,35	3,55
4,0 h	45 cm	GPS/Galli	next to	std corr	-2,93	3,28
83 h	11 cm	GPS/Galli	15cm next to/metal	std corr	-1,18	3,41
55 h	11 cm	GPS/Galli	15cm next to/metal	fixed w/diff	-0,67	3,38
50 min	11 cm	GPS/Galli	4,18 m	std corr	-6,40	4,96
8 min	11 cm	GPS/Galli	4,18 cm	std corr	-3,2	3,11
2 min	11 cm	GPS/Galli	3,00 cm	std corr	-3,77	3,02
95 h	11 cm	GPS/Galli	15cm next to/metal	fixed w/diff	-2,70	3,45
50 min	11 cm	GPS/Galli	next to/metal	corr w/diff	8,95	3,29
27 h	11 cm	GPS/Galli	4,17 m	std corr	-2,01	3,35
38 h	11 cm	GPS/Galli	4,17m \leftrightarrow 1,53m	fixed w/diff	-2,64	3,37
3 min	11 cm	GPS/Galli	4,17m \leftrightarrow 3,03	fixed w/diff	1,38	3,13
6 min	11 cm	GPS/Galli	4,17m \leftrightarrow 3,03	fixed w/diff	1,04	3,3
4 min	11 cm	GPS/Galli	4,17m \leftrightarrow 3,03	fixed w/diff	4,74	3,1
10 min	11 cm	GPS/Galli	4,17m \leftrightarrow 82cm	fixed w/diff	33,88	5,29
-	11 cm	GPS/Galli	\leftrightarrow 812cm	fixed w/diff	-	-
3 cm	11 cm	GPS/Galli	4,17 cm	fixed w/diff	-1,24	3,35
2 h	11 cm	GPS/Galli	4,17cm \uparrow 10cm	fixed w/diff	-3,10	3,36
-	11 cm	GPS/Galli	\uparrow 100cm	fixed w/diff	-	-
51 h	11 cm	all	4,17cm	std corr	-0,53	3,50
16 h	11 cm	all	4,17cm \uparrow 10cm	fixed w/diff	26,07	3,68
129 h	11 cm	all	~4,17cm \uparrow 20cm	fixed w/diff	45,16	7,26
95 h	11 cm	all	4,2 cm \rightarrow 10cm	fixed w/diff	4,82	13,42
					\hookrightarrow -13,76	5,59
					\hookrightarrow 12,86	5,59
45 h	11 cm	all	~4,2 m	std corr	-0,70	3,41

Figure A.1: Handwritten table with fit results for all time pulse measurement runs, including short runs.

B all time pulse measurement plots

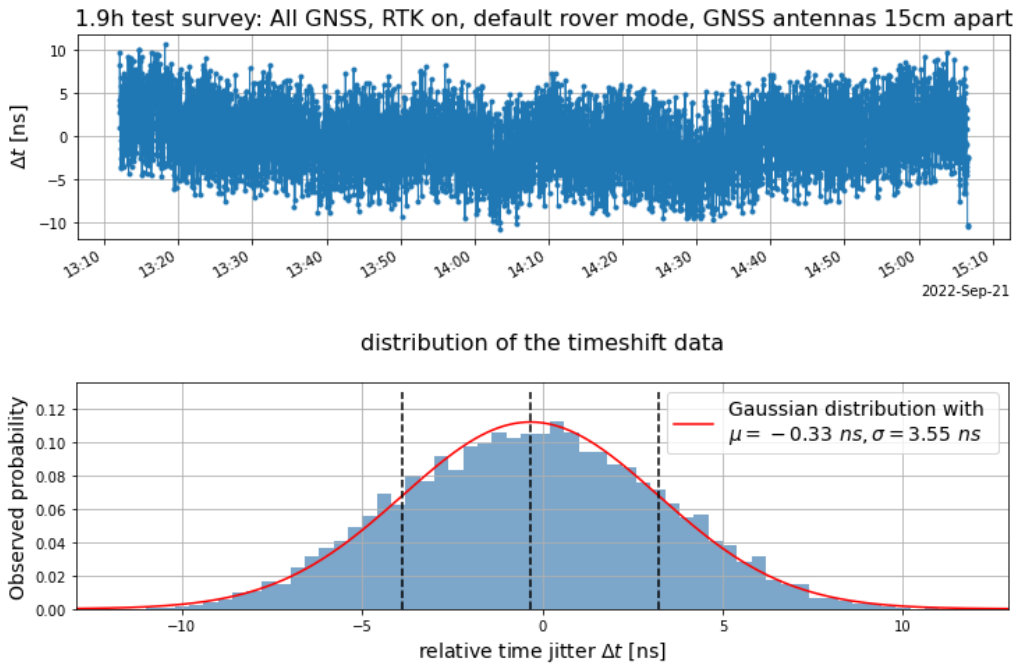


Figure B.2: Time pulse measurement results for the 2h test run.

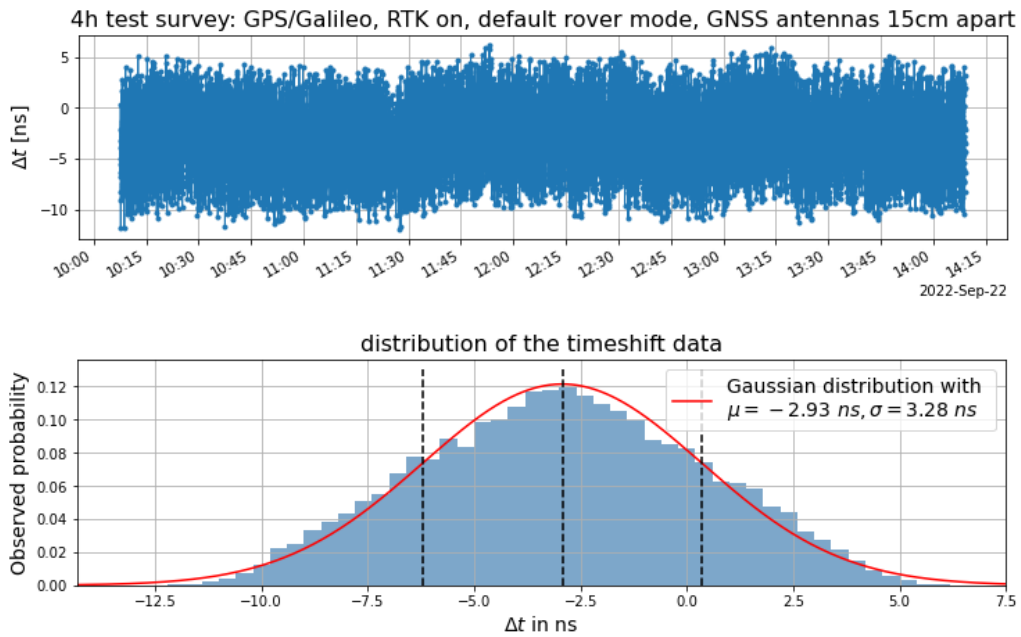


Figure B.3: Time pulse measurement results for the 4h test run.

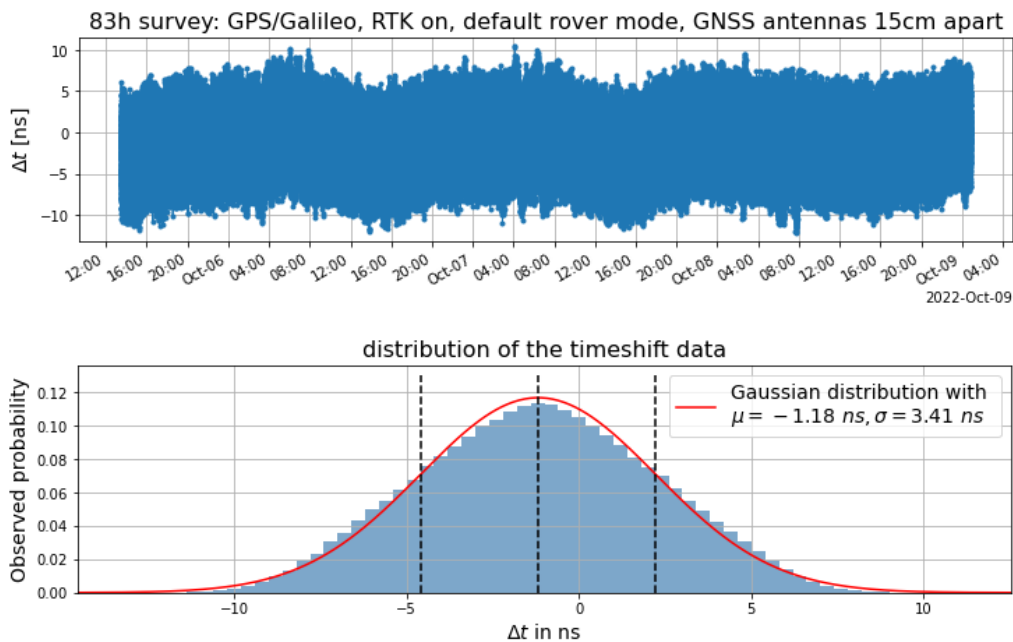


Figure B.4: Time pulse measurement results for the 83h run.

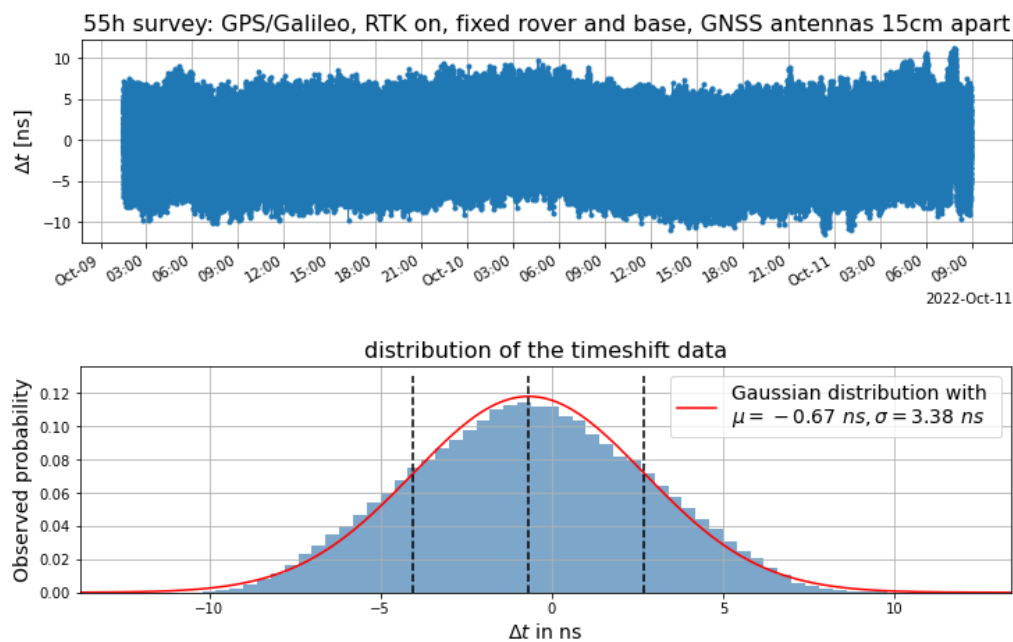


Figure B.5: Time pulse measurement results for the 55h run.

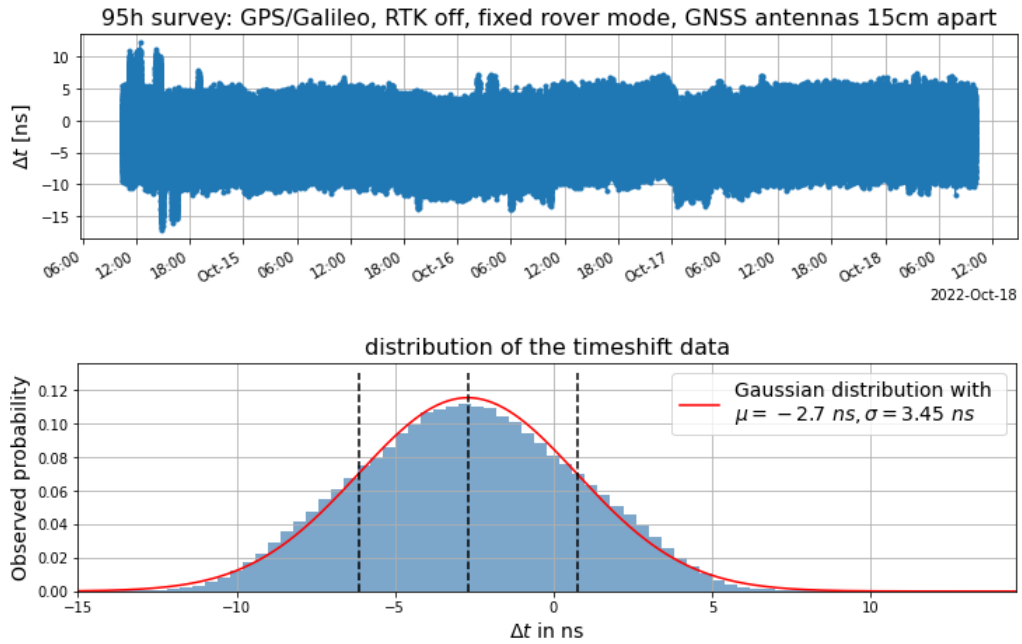


Figure B.6: Time pulse measurement results for first 95h run.

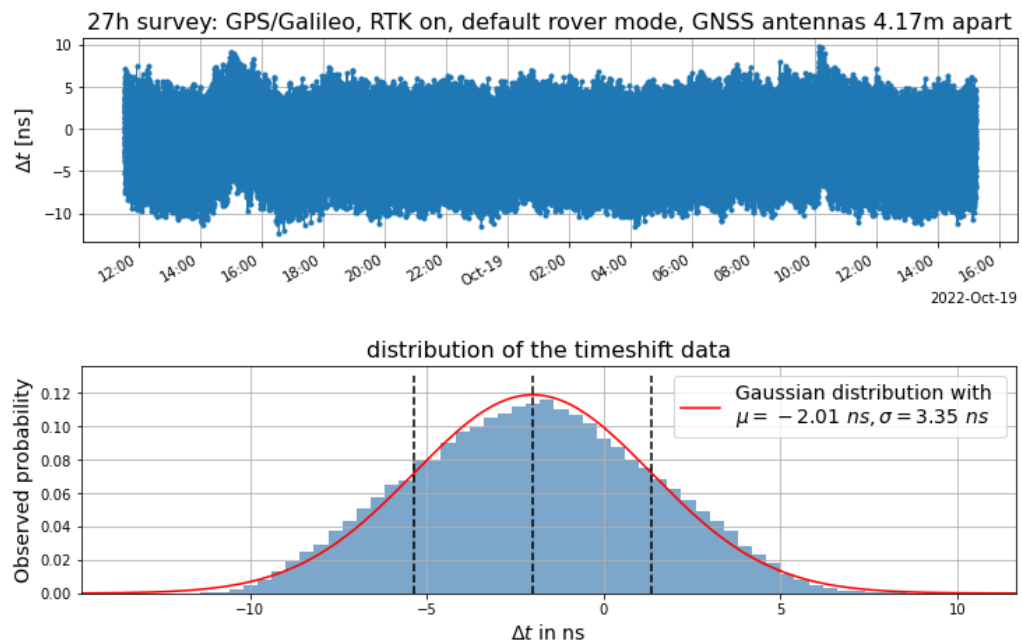


Figure B.7: Time pulse measurement results for the 27h run.

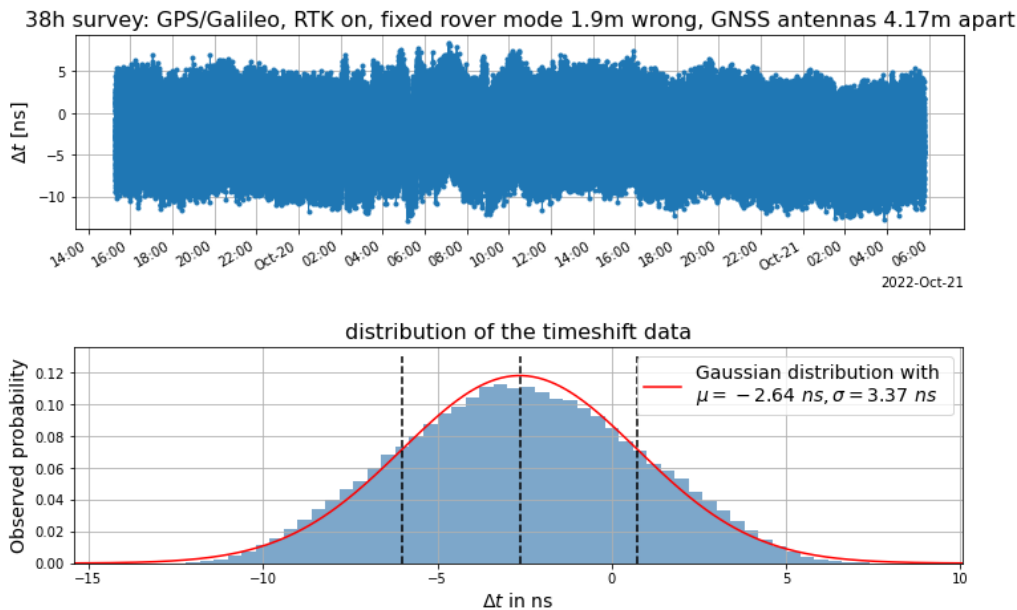


Figure B.8: Time pulse measurement results for the 38h run.

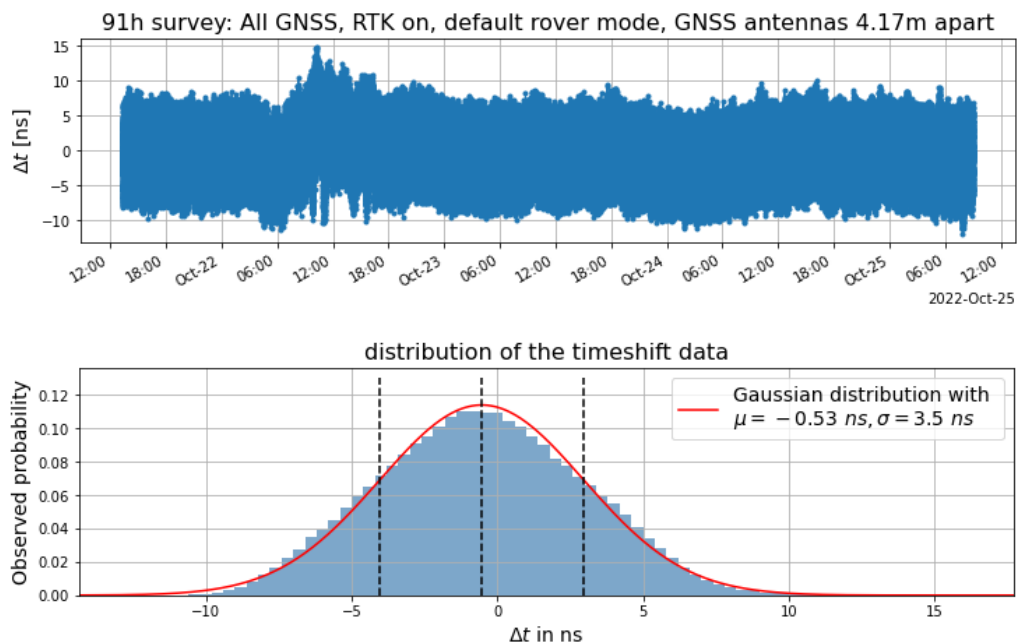


Figure B.9: Time pulse measurement results for the 91h run.

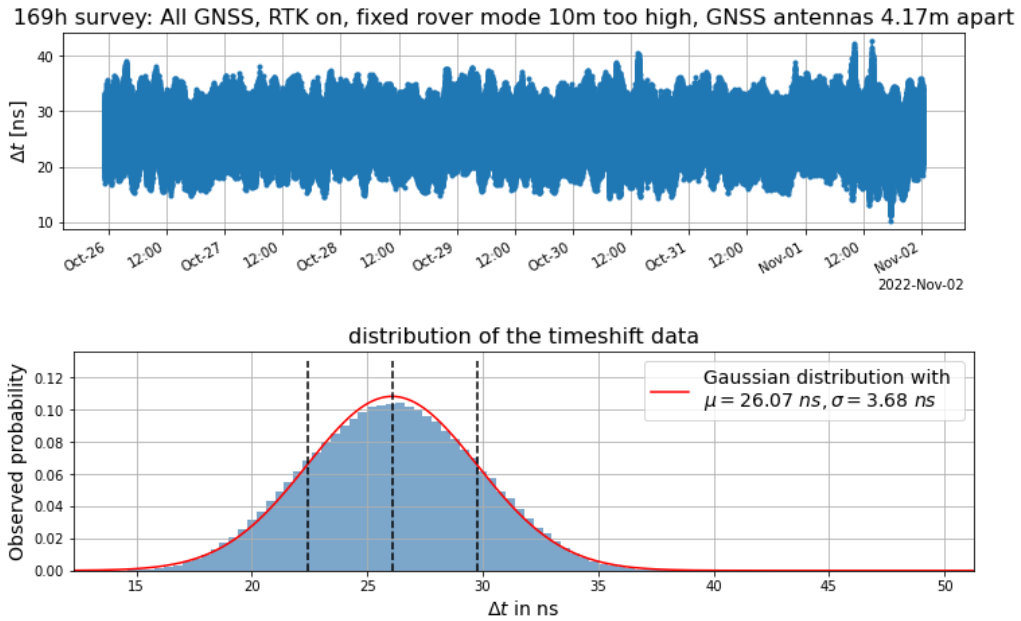


Figure B.10: Time pulse measurement results for the 169h run.

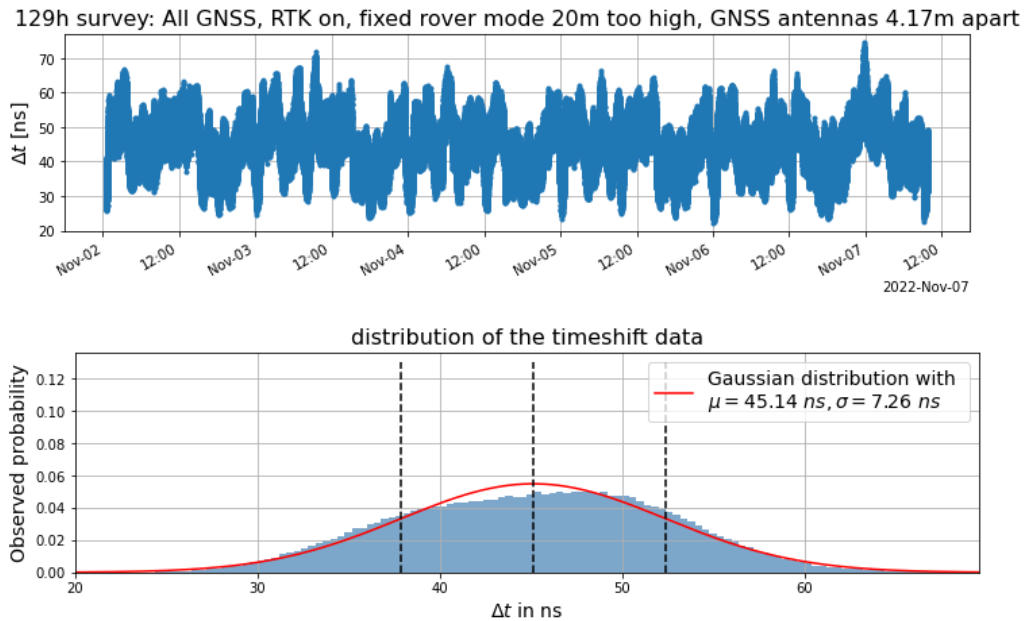


Figure B.11: Time pulse measurement results for the 129h run.

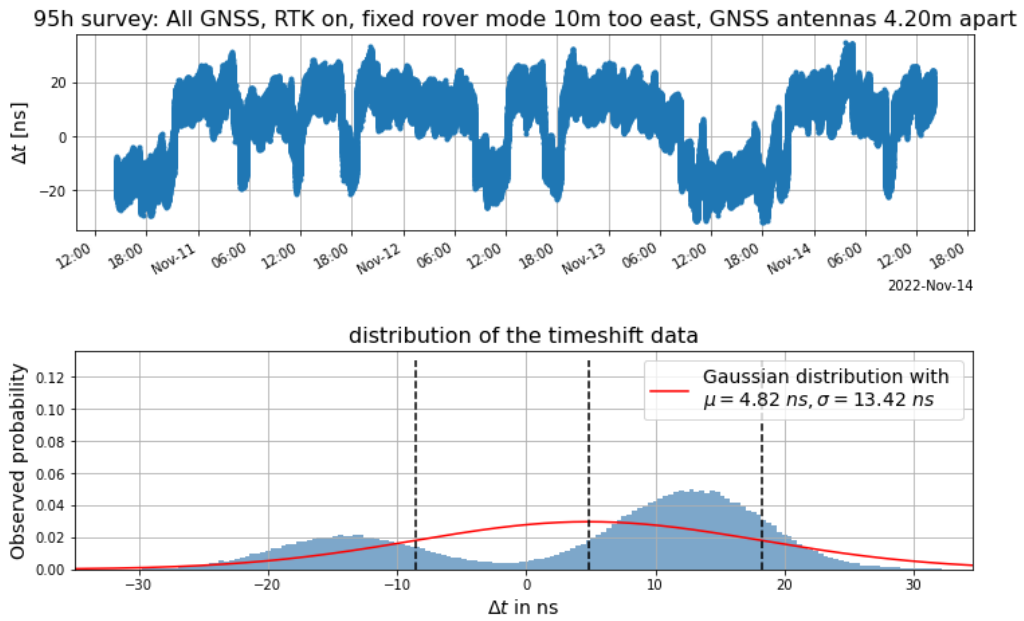


Figure B.12: Time pulse measurement results for the second 95h run.

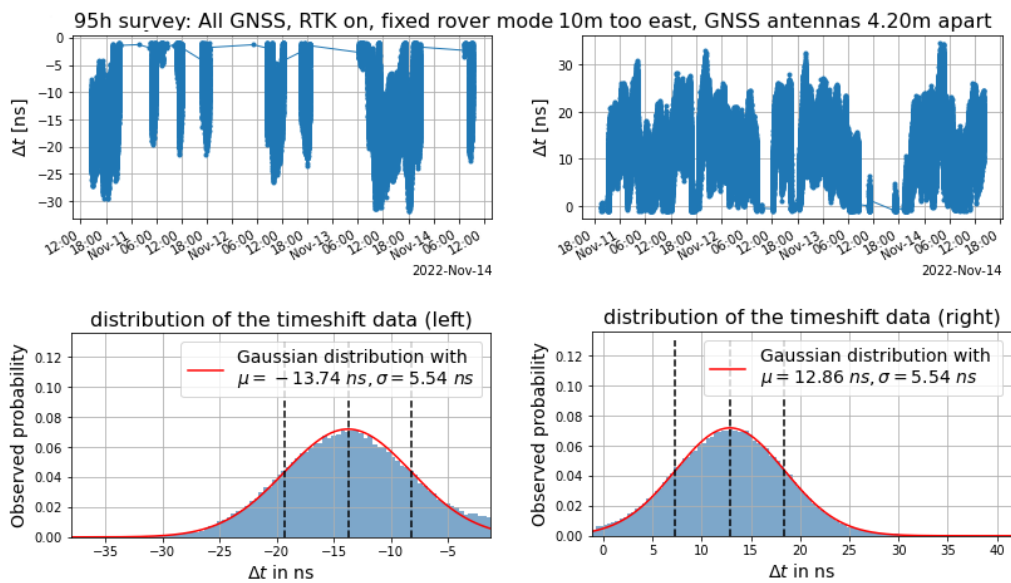


Figure B.13: Time pulse measurement results for the second 95h run, with two fits.

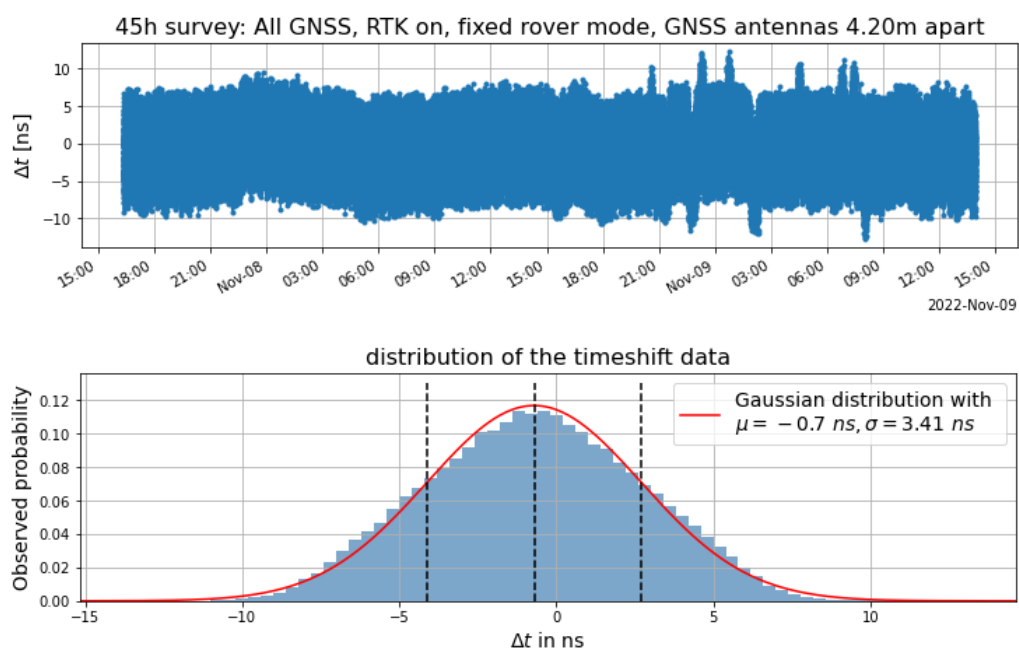


Figure B.14: Time pulse measurement results for the 45h run.

C additional beacon analysis plots

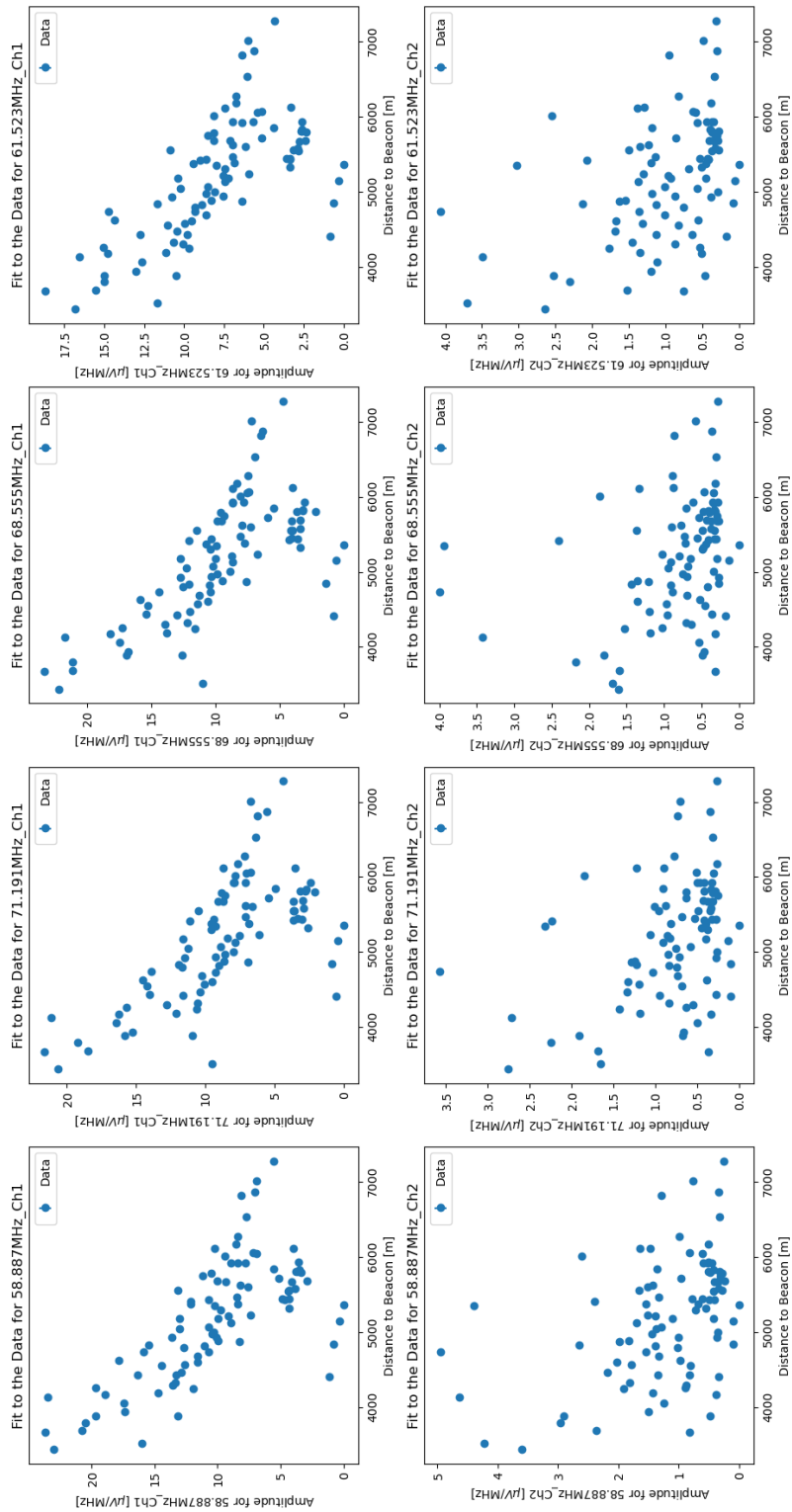


Figure C.15: Scatter plot of the pre-processed data for path channel 1 and 2, day 2015-10-01. We notice that the beacon amplitudes in channel 2 are barely there

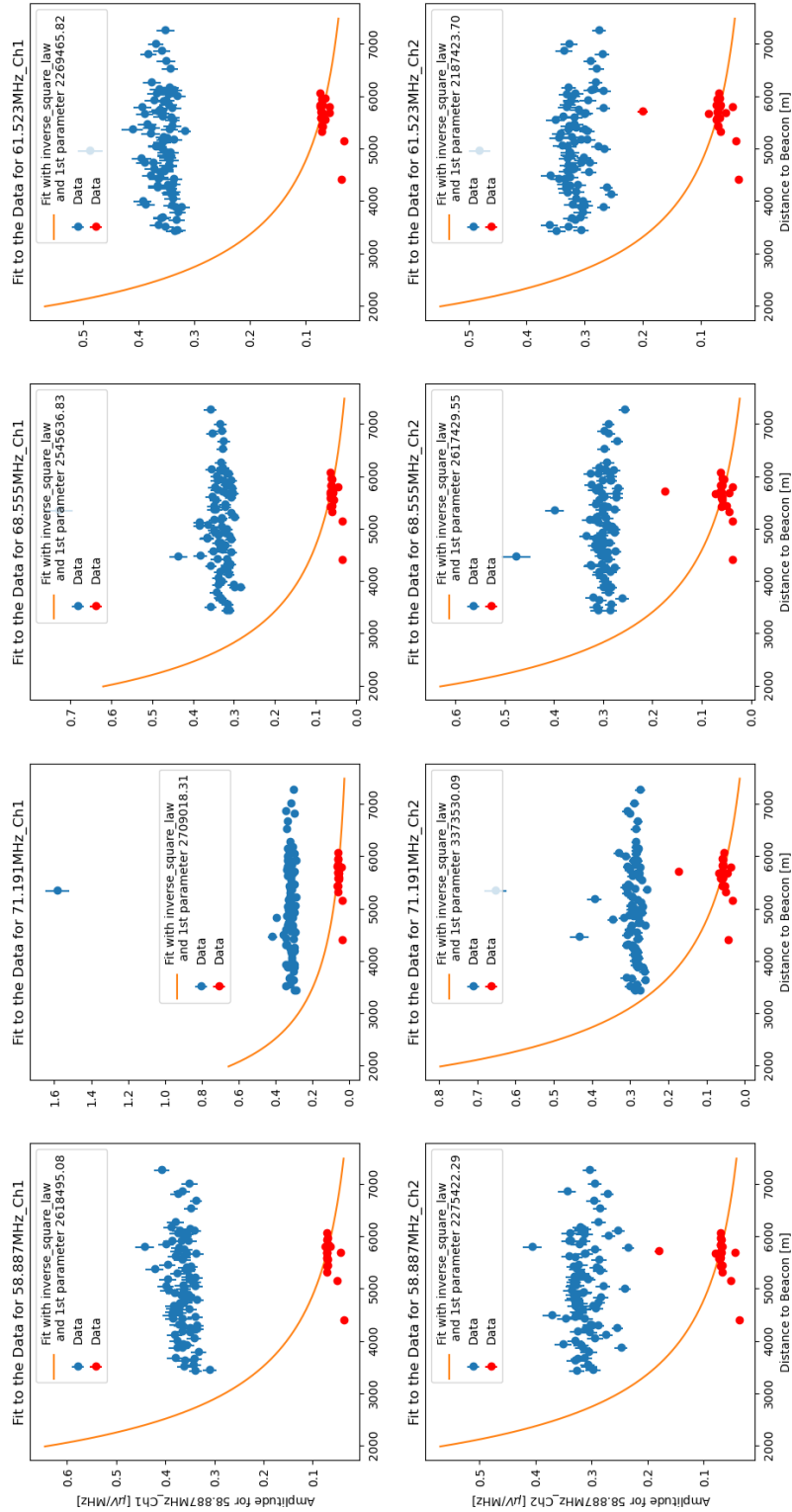


Figure C.16: Scatter plot of the pre-processed data for both channel 1 and 2 with outliers marked red, on day 2017-05-08 when the beacon was not operating. The outliers here coincide with those from Fig. 5.6, pointing to the LPDA antennas

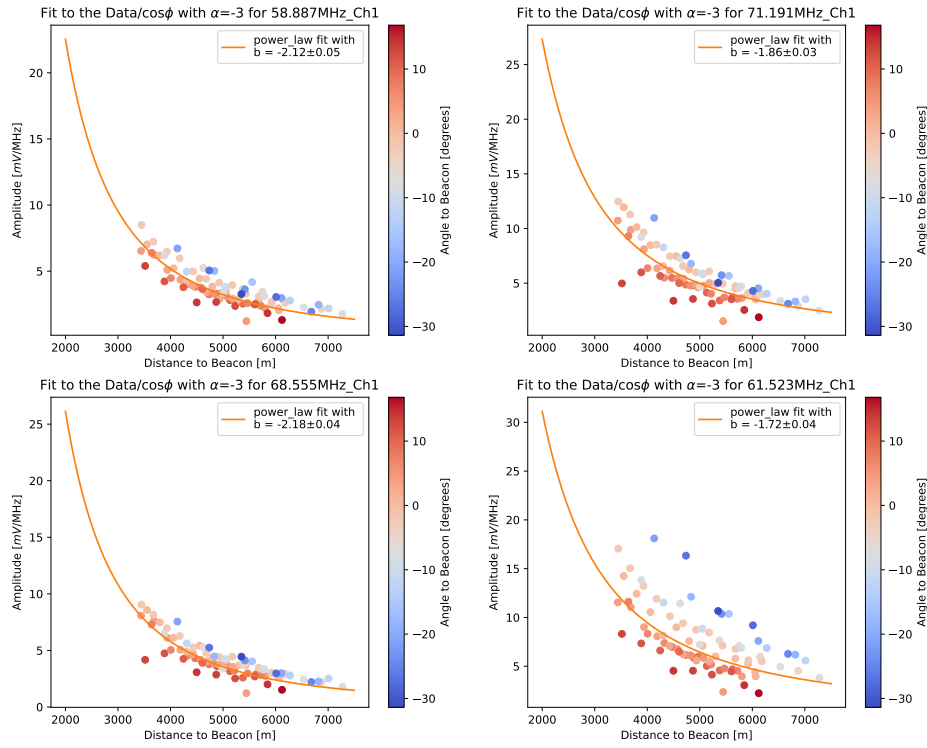


Figure C.17: Power Law fit with $\alpha = -3^\circ$ on all stations. For the variant with a ϕ based cut see Fig. 5.13. For a variant with $\alpha = 0^\circ$, see Fig. C.18

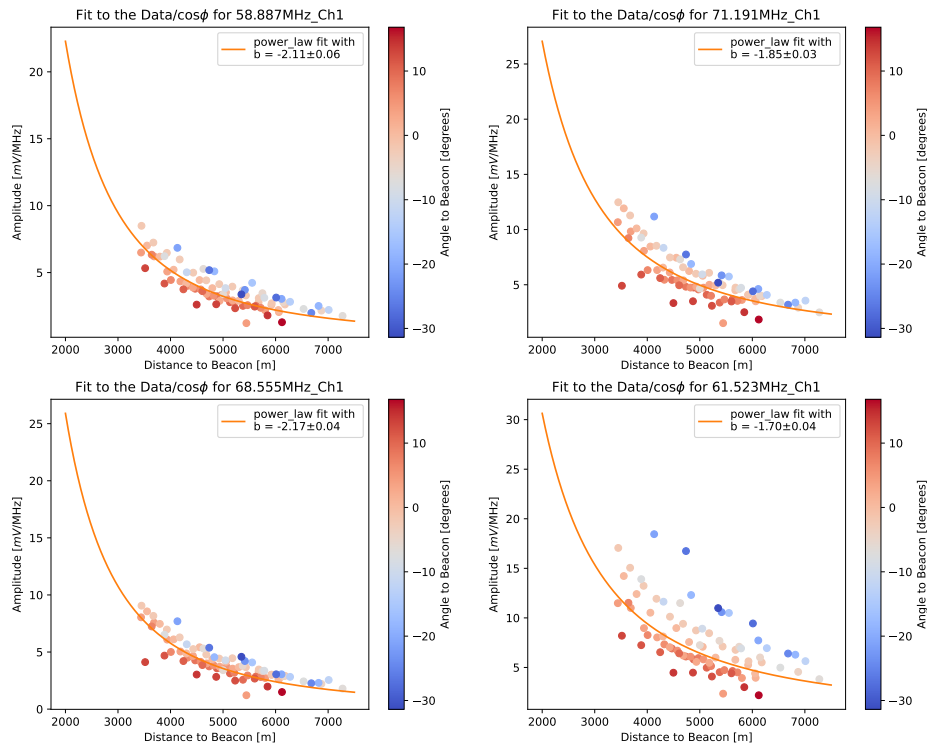


Figure C.18: Power Law fit with $\alpha = 0^\circ$ on all stations. For the variant with a ϕ based cut see Fig. 5.13

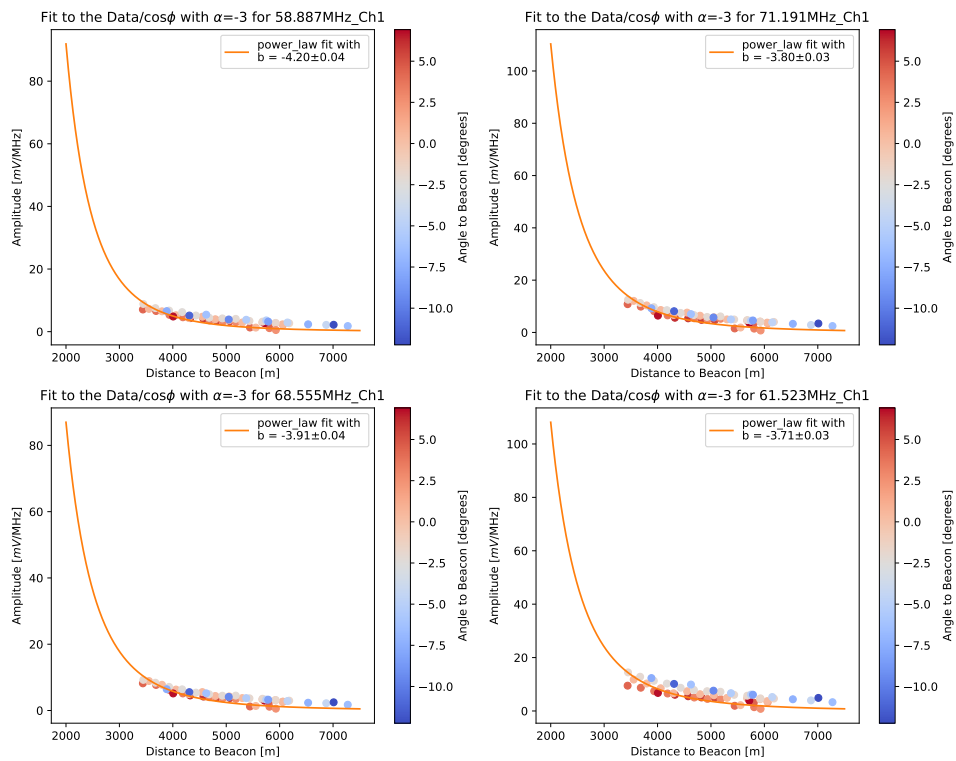


Figure C.19: Fit plot of the anomalously high b value on the 2018-12-04.

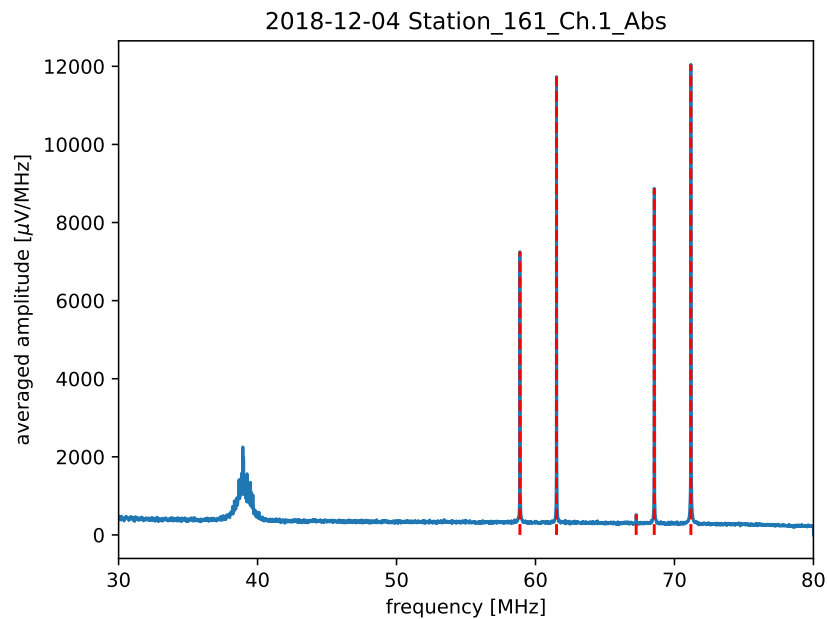


Figure C.20: Average spectrum of station 161 on the 2018-12-04, when the anomalously high b value occurred.

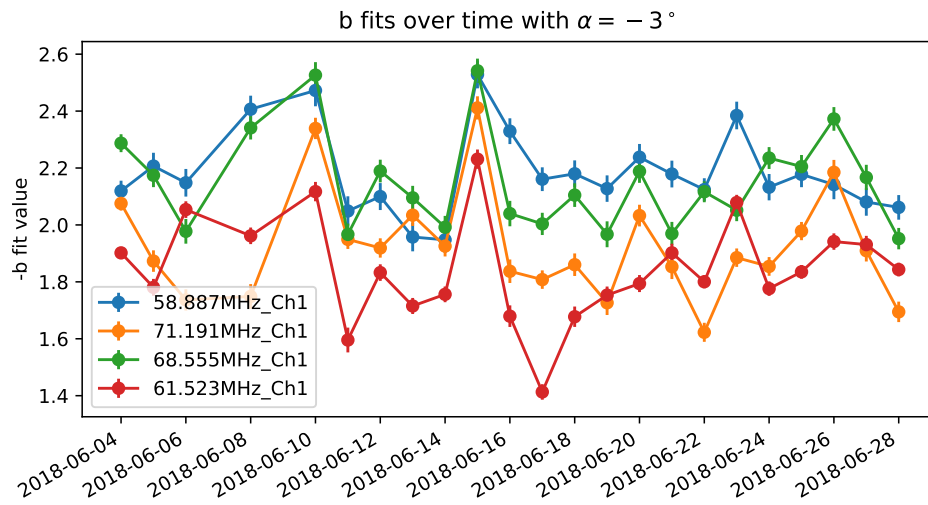


Figure C.21: Evolution of the spectral index b over the course of June 2018, no station cut based on ϕ .

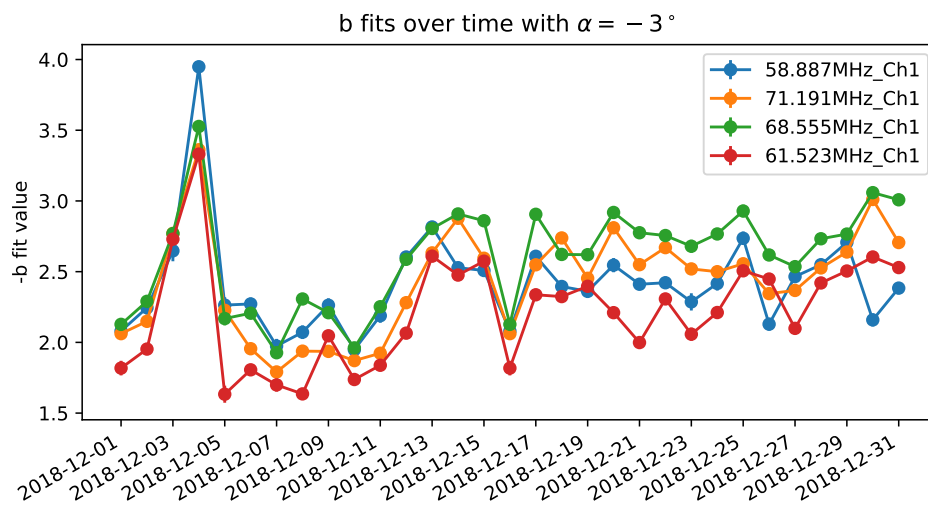


Figure C.22: Evolution of the spectral index b over the course of December 2018, no station cut based on ϕ . Values shift a bit down, when compared to Fig. 5.16.

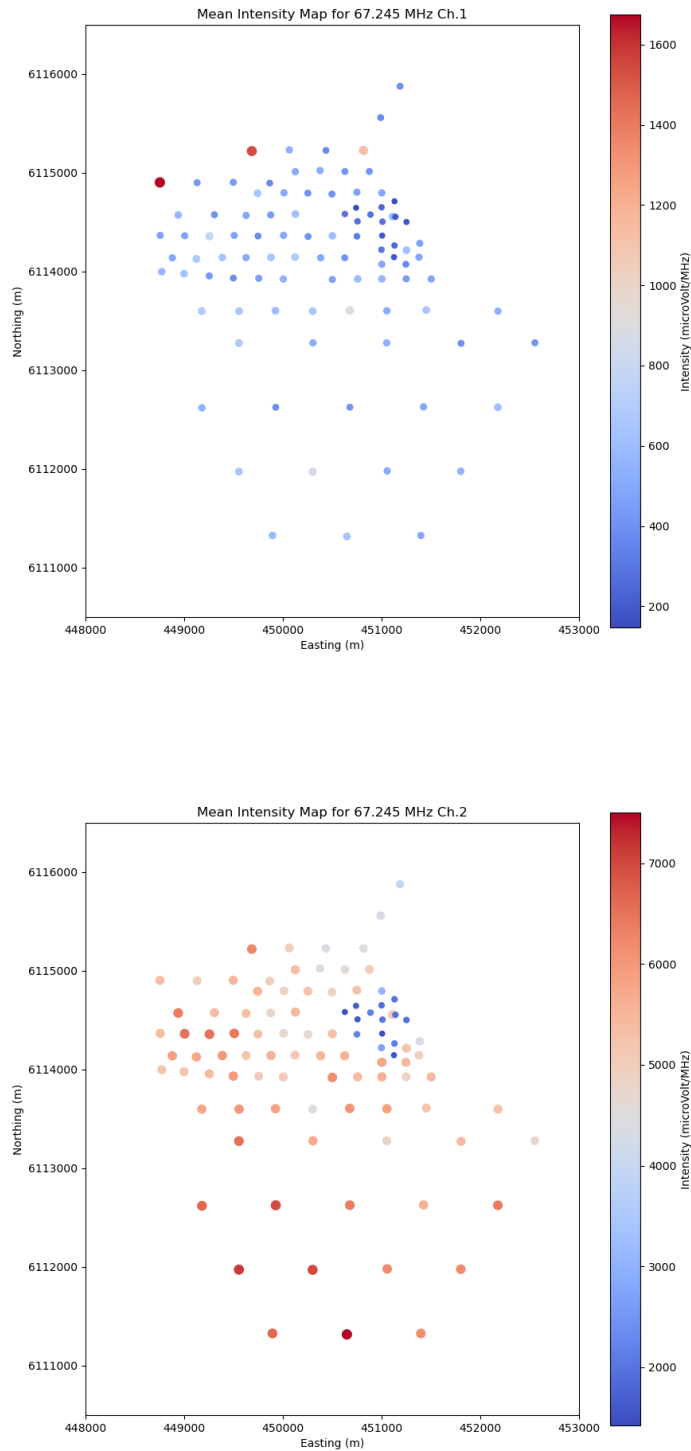


Figure C.23: Intensity maps of the TV station carrier frequency at 67.25 MHz, on 8th of May 2019. We can guess that the TV station transmitter is located towards or in Malargüe.

Acronyms

- ADC** analog to digital converter. 39, 52
- ADS-B** Automatic Dependent Surveillance Broadcast. 22
- AERA** Auger Engineering Radio Array. ix, x, 8, 10, 11, 15, 20–22, 37–42, 49, 50, 53, 55, 57
- BLS** Balloon Launching Station. 8
- CDAS** Central Data Acquisition System. 8
- CDMA** code-division multiple access. 16
- CERN** European Organization for Nuclear Research. 15, 37
- CLF** Central Laser Facility. 8
- CMB** Cosmic Microwave Background. 5
- CS** Commercial Service. 19
- DAQ** data acquisition. ix, 24, 28, 29, 31, 32
- DFT** Discrete Fourier Transform. 54
- DGPS** Differential GPS. 18
- DoD** United States Department of Defense. 17
- DTFT** Discrete Time Fourier Transform. 54
- EAS** Extensive Air Shower. ix, 1, 3, 5, 6, 9, 11, 12, 20
- EGNOS** European Geostationary Navigation Overlay Service. 18
- ETRS89** European Terrestrial Reference System 1989. 20, 35
- FD** Fluorescence Detector. 8, 9, 20, 21
- FFT** Fast Fourier Transform. 54
- FOV** field of view. 9
- GDOP** Geometric Dilution of Precision. 18, 24, 30
- GNSS** Global Navigation Satellite Systems. ix, 1, 15–20, 22–27, 29, 31, 35, 36, 57
- GPS** Global Positioning System. 1, 11, 16–20, 24–26, 29–36

- HAS** Galileo High Accuracy Service. 19, 20
- HEAT** High Elevation Auger Telescope. 8
- IGRF** International Geomagnetic Reference Field. 49
- ITRF** International Terrestrial Reference Frame. 20
- KIT** Karlsruhe Institute of Technology. 24, 35
- LOPES** Low-Frequency Array (LOFAR) Prototype Station. 11
- LPDA** Logarithmic Periodic Dipole Antenna. ix, 10, 42, 70
- MEO** Medium Earth Orbit. 16
- MSAS** Multi-functional Satellite Augmentation System. 18
- NMEA** National Marine Electronics Association. 24
- NTRIP** Networked Transport of RTCM via Internet Protocol. 19, 20
- OS** Operating System. 24
- PMT** Photomultiplier tube. 8, 9
- pps** pulse-per-second. 26, 28–30
- PRN** pseudo-random noise. 16
- RD** Radio Detector. 10, 11, 36–38, 52–55, 57
- RIT** radio interferometric technique. 11, 12
- RTK** Real-Time Kinematic positioning. ix, 19, 23–26, 29–33, 35, 36, 57
- SA** Selective Availability. 17
- SALLA** Short Aperiodic Loaded Loop. 10, 21
- SBAS** Satellite-Based Augmentation Systems. 18, 19
- SD** Surface Detector. ix, 8–11
- SDK** Software Development Kit. 24
- SNR** supernova remnant. 4, 5
- SSD** surface scintillator detector. 9
- TTFF** time to first fix. 25
- UHECR** Ultra High Energy Cosmic Ray. 1, 5, 10, 12, 58
- UTC** Coordinated Universal Time. 15–18
- UTM** Universal Transverse Mercator. 39, 40, 46

WAAS Wide Area Augmentation System. 18

WCD water Cherenkov detector. 8, 9, 11

WGS84 World Geodetic System 1984. 20, 25, 35

WR PTP White Rabbit Precision Time Protocol. 15

XLF eXtreme Laser Facility. 8

Bibliography

- [1] R. Alves Batista et al. “Open Questions in Cosmic-Ray Research at Ultrahigh Energies”. In: *Front. Astron. Space Sci.* 6 (2019), p. 23. DOI: 10.3389/fspas.2019.00023. arXiv: 1903.06714 [astro-ph.HE].
- [2] P. Auger et al. “Extensive Cosmic-Ray Showers”. In: *Rev. Mod. Phys.* 11 (3-4 July 1939), pp. 288–291. DOI: 10.1103/RevModPhys.11.288. URL: <https://link.aps.org/doi/10.1103/RevModPhys.11.288>.
- [3] Pierre Auger Collaboration. “The Pierre Auger Cosmic Ray Observatory”. In: *Nuclear Instruments and Methods in Physics Research Section A: Accelerators, Spectrometers, Detectors and Associated Equipment* 798 (Oct. 2015), pp. 172–213. DOI: 10.1016/j.nima.2015.06.058. URL: <https://doi.org/10.1016%2Fj.nima.2015.06.058>.
- [4] P. Allison et al. “Timing Calibration and Synchronization of Surface and Fluorescence Detectors of the Pierre Auger Observatory”. In: *29th International Cosmic Ray Conference (ICRC29)*. Vol. 8. International Cosmic Ray Conference. Jan. 2005, p. 307. URL: <https://ui.adsabs.harvard.edu/abs/2005ICRC...8..307A>.
- [5] H. Schoorlemmer and W. R. Carvalho. “Radio interferometry applied to the observation of cosmic-ray induced extensive air showers”. In: *The European Physical Journal C* 81.12 (Dec. 2021). DOI: 10.1140/epjc/s10052-021-09925-9. URL: <https://doi.org/10.1140%2Fepjc%2Fs10052-021-09925-9>.
- [6] F. Schlüter and T. Huege. “Expected performance of air-shower measurements with the radio-interferometric technique”. In: *Journal of Instrumentation* 16.07 (July 2021), P07048. DOI: 10.1088/1748-0221/16/07/p07048. URL: <https://doi.org/10.1088%2F1748-0221%2F16%2F07%2Fp07048>.
- [7] F. Schröder et al. “New method for the time calibration of an interferometric radio antenna array”. In: *Nuclear Instruments and Methods in Physics Research Section A: Accelerators, Spectrometers, Detectors and Associated Equipment* 615.3 (Apr. 2010), pp. 277–284. DOI: 10.1016/j.nima.2010.01.072. URL: <https://doi.org/10.1016%2Fj.nima.2010.01.072>.
- [8] A. Aab et al. “Nanosecond-level time synchronization of autonomous radio detector stations for extensive air showers”. In: *JINST* 11.01 (2016), P01018. DOI: 10.1088/1748-0221/11/01/P01018. arXiv: 1512.02216 [physics.ins-det].
- [9] T. Wulf et al. “Observations on the radiation of high penetration power on the Eiffel tower”. In: *Physikalische Zeitschrift* 11.811 (1910), pp. 2155–304.
- [10] V. Hess. *On the Observations of the Penetrating Radiation during Seven Balloon Flights*. 2018. arXiv: 1808.02927 [physics.hist-ph].
- [11] W. Bothe and W. Kolhörster. “Das Wesen der Höhenstrahlung”. In: *Zeitschrift für Physik* 56.11-12 (1929), pp. 751–777. DOI: 10.1007/BF01340137.

- [12] M. Ackermann et al. “Detection of the Characteristic Pion-Decay Signature in Supernova Remnants”. In: *Science* 339.6121 (2013), pp. 807–811. DOI: 10.1126/science.1231160. eprint: <https://www.science.org/doi/pdf/10.1126/science.1231160>. URL: <https://www.science.org/doi/abs/10.1126/science.1231160>.
- [13] IceCube Collaboration et al. “Neutrino emission from the direction of the blazar TXS 0506+056 prior to the IceCube-170922A alert”. In: *Science* 361.6398 (July 2018), pp. 147–151. DOI: 10.1126/science.aat2890.
- [14] W. Bietenholz. “The Most Powerful Particles in the Universe: A Cosmic Smash”. In: *Revista Cubana de Física* 31.1 (2014), pp. 45–50. ISSN: 2224-7939. arXiv: 1305.1346 [physics.hist-ph].
- [15] A. Haungs. “Cosmic Rays from the Knee to the Ankle”. In: *Phys. Procedia* 61 (2015). Ed. by F. Avignone and W. Haxton, pp. 425–434. DOI: 10.1016/j.phpro.2014.12.094. arXiv: 1504.01859 [astro-ph.HE].
- [16] K. Greisen. “End to the Cosmic-Ray Spectrum?” In: *Phys. Rev. Lett.* 16 (17 Apr. 1966), pp. 748–750. DOI: 10.1103/PhysRevLett.16.748. URL: <https://link.aps.org/doi/10.1103/PhysRevLett.16.748>.
- [17] G. T. Zatsepin and V. A. Kuz’min. “Upper limit of the spectrum of cosmic rays”. In: *Soviet Journal of Experimental and Theoretical Physics Letters* 4 (1966), p. 78. URL: http://www.jetpletters.ru/ps/1624/article_24846.pdf.
- [18] A. M. Hillas. “The Origin of Ultra-High-Energy Cosmic Rays”. In: *Annual Review of Astronomy and Astrophysics* 22.1 (1984), pp. 425–444. DOI: 10.1146/annurev.aa.22.090184.002233. eprint: <https://doi.org/10.1146/annurev.aa.22.090184.002233>. URL: <https://doi.org/10.1146/annurev.aa.22.090184.002233>.
- [19] S. Paredes Saenz. *2019 CERN Latin-American School of HEP: Student Project Presentation: Cosmic Ray Studies at the Pierre Auger Observatory*. [online]. [Last access: 07.09.2023]. URL: <https://indico.cern.ch/event/763013/contributions/3358878/>.
- [20] T. Huege. “Radio detection of cosmic ray air showers in the digital era”. In: *Phys. Rept.* 620 (2016), pp. 1–52. DOI: 10.1016/j.physrep.2016.02.001. arXiv: 1601.07426 [astro-ph.IM].
- [21] F. G. Schröder. “Radio detection of cosmic-ray air showers and high-energy neutrinos”. In: *Progress in Particle and Nuclear Physics* 93 (Mar. 2017), pp. 1–68. DOI: 10.1016/j.pnpnp.2016.12.002. URL: <https://doi.org/10.1016%2Fj.pnpnp.2016.12.002>.
- [22] I. Allekotte et al. “The surface detector system of the Pierre Auger Observatory”. In: *Nuclear Instruments and Methods in Physics Research Section A: Accelerators, Spectrometers, Detectors and Associated Equipment* 586.3 (Mar. 2008), pp. 409–420. DOI: 10.1016/j.nima.2007.12.016. URL: <https://doi.org/10.1016%2Fj.nima.2007.12.016>.
- [23] J. Abraham et al. “The fluorescence detector of the Pierre Auger Observatory”. In: *Nuclear Instruments and Methods in Physics Research Section A: Accelerators, Spectrometers, Detectors and Associated Equipment* 620.2-3 (Aug. 2010), pp. 227–251. DOI: 10.1016/j.nima.2010.04.023. URL: <https://doi.org/10.1016%2Fj.nima.2010.04.023>.
- [24] C. Meurer and N. Scharf. “HEAT – a low energy enhancement of the Pierre Auger Observatory”. In: *Astrophysics and Space Sciences Transactions* 7.2 (May 2011), pp. 183–186. DOI: 10.5194/astra-7-183-2011. URL: <https://doi.org/10.5194%2Fastra-7-183-2011>.

- [25] B. Fuchs. “The Auger Engineering Radio Array”. In: *Nuclear Instruments and Methods in Physics Research Section A: Accelerators, Spectrometers, Detectors and Associated Equipment* 692 (2012). 3rd Roma International Conference on Astroparticle Physics, pp. 93–97. ISSN: 0168-9002. DOI: <https://doi.org/10.1016/j.nima.2012.01.058>. URL: <https://www.sciencedirect.com/science/article/pii/S0168900212001155>.
- [26] D. Veberič. *Auger Array*. [online]. [Last access: 07.09.2023]. URL: https://www-f9.ijs.si/~darko/auger/auger-array/auger_array-jpg/.
- [27] A. A. Watson. “The Discovery of Cherenkov Radiation and its use in the detection of extensive air showers”. In: *Nucl. Phys. B Proc. Suppl.* 212-213 (2011). Ed. by R. Caruso et al., pp. 13–19. DOI: 10.1016/j.nuclphysbps.2011.03.003. arXiv: 1101.4535 [physics.hist-ph].
- [28] A. Castellina. “AugerPrime: the Pierre Auger Observatory Upgrade”. In: *EPJ Web of Conferences* 210 (2019). Ed. by I. Lhenry-Yvon et al., p. 06002. DOI: 10.1051/epjconf/201921006002. URL: <https://doi.org/10.1051%2Fepjconf%2F201921006002>.
- [29] C. Glaser. *ARENA 2016 Overview Talk Presentation: Results and Perspectives of the Auger Engineering Radio Array*. [online]. [Last access: 07.09.2023]. URL: <https://indico.cern.ch/event/461474/contributions/2152645>.
- [30] P. Abreu et al. “Antennas for the Detection of Radio Emission Pulses from Cosmic-Ray”. In: *JINST* 7 (2012), P10011. DOI: 10.1088/1748-0221/7/10/P10011. arXiv: 1209.3840 [astro-ph.IM].
- [31] T. Huege. “The Radio Detector of the Pierre Auger Observatory – status and expected performance”. In: *EPJ Web Conf.* 283 (2023), p. 06002. DOI: 10.1051/epjconf/202328306002. arXiv: 2305.10104 [astro-ph.IM].
- [32] H. Falcke et al. “Detection and imaging of atmospheric radio flashes from cosmic ray air showers”. In: *Nature* 435.7040 (May 2005), pp. 313–316. DOI: 10.1038/nature03614. URL: <https://doi.org/10.1038%2Fnature03614>.
- [33] H. Schoorlemmer. “Radio Interferometry applied to air showers recorded by the Auger Engineering Radio Array”. In: *38th International Cosmic Ray Conference (ICRC2023)*. International Cosmic Ray Conference. July 2023, p. 380. DOI: 10.22323/1.444.0380.
- [34] CERN. *The White Rabbit Project*. [online]. [Last access: 09.09.2023]. URL: <http://white-rabbit.web.cern.ch/>.
- [35] J. Serrano et al. “The White Rabbit project”. In: *IBIC2013* (2013). URL: <https://cds.cern.ch/record/1743073>.
- [36] J. E. Gilligan et al. “White Rabbit Time and Frequency Transfer Over Wireless Millimeter-Wave Carriers”. In: *IEEE Transactions on Ultrasonics, Ferroelectrics, and Frequency Control* 67.9 (2020), pp. 1946–1952. DOI: 10.1109/TUFFC.2020.2989667.
- [37] European Union Agency for the Space Programme (EUSPA). *Constellation Information*. [online]. [Last access: 09.09.2023]. URL: <https://www.gsc-europa.eu/system-service-status/constellation-information>.
- [38] J. Van Sickle. *GPS Modernization and GNSS*. [online]. [Last access: 09.09.2023]. URL: <https://janvansickle.com/gps-modernization-and-gnss/>.
- [39] United States Government. *GPS Accuracy*. [online]. [Last access: 09.09.2023]. URL: <https://www.gps.gov/systems/gps/performance/accuracy/>.

- [40] u-blox Blog. *Real-Time Kinematic (RTK)*. [online]. [Last access: 08.05.2023]. Nov. 2022. URL: <https://www.u-blox.com/en/technologies/rtk-real-time-kinematic>.
- [41] European Union Agency for the Space Programme (EUSPA). *Galileo High Accuracy Service (HAS)*. [online]. [Last access: 09.09.2023]. URL: <https://www.euspa.europa.eu/european-space/galileo/services/galileo-high-accuracy-service-has>.
- [42] Eos Positioning Systems, Inc. *Galileo High Accuracy Service Early Observations*. [online]. [Last access: 12.09.2023]. URL: <https://eos-gnss.com/knowledge-base/galileo-high-accuracy-service-early-observations>.
- [43] R. Stanaway. *GDA94, ITRF & WGS84. What's the difference? Working with Dynamic Datums*. [online]. [Last access: 09.09.2023]. URL: <http://www.quickclose.com.au/stanaway07pres.pdf>.
- [44] ArduSimple Store. *simpleRTK2B – Starter Kit LR*. [online]. [Last access: 08.05.2023]. URL: <https://www.ardusimple.com/product/simplertk2b-starter-kit-lr-ip65/>.
- [45] ArduSimple. *MR/LR/XLR XBee Radio*. [online]. [Last access: 08.05.2023]. URL: <https://www.ardusimple.com/xbee-antenna-installation-guide/>.
- [46] Pico Technology. *picosdk-python-wrappers, PicoSDK for Python*. [online]. [Last access: 08.05.2023]. URL: <https://github.com/picotech/picosdk-python-wrappers>.
- [47] Geoscience Australia, Australian Government. *Geodetic Calculators, Vincenty's Inverse*. [online]. [Last access: 08.05.2023]. URL: <https://geodesyapps.ga.gov.au/vincenty-inverse>.
- [48] ArduSimple. *GPS/GNSS Antenna Installation Guide*. [online]. [Last access: 15.04.2023]. URL: <https://www.ardusimple.com/gps-gnss-antenna-installation-guide/>.
- [49] u-blox. *ZED-F9P-02B data sheet*. [online]. [Last access: 10.09.2023]. Mar. 2023. URL: https://content.u-blox.com/sites/default/files/documents/ZED-F9P-02B_DataSheet_UBX-21023276.pdf.
- [50] A. Bogovič. *Use Of Global Positioning Systems As Time Reference in Astrophysics Experiments And Its Accuracy*. Diploma Thesis, University of Nova Gorica. 2013. URL: <https://www2.ung.si/~library/diplome/FIZIKA/6Bogovic.pdf>.
- [51] Landesamt für Geoinformation und Landentwicklung, Baden-Württemberg. *Kontrollpunkt: Bruchsal, Untergrombach*. [online]. [Last access: 02.05.2023]. URL: <https://www.lgl-bw.de/unsere-themen/Geoinformation/Kontrollpunkte/kontrollpunkt-bruchsal-untergrombach/>.
- [52] u-blox. *ZED-F9T-10B data sheet*. [online]. [Last access: 10.09.2023]. June 2023. URL: https://content.u-blox.com/sites/default/files/ZED-F9T-10B_DataSheet_UBX-20033635.pdf.
- [53] M. Cristinziani, Q. Dorosti, S. Heidbrink, N. Siegmund, J. Winter, and M. Ziolkowski. *Nanosecond time synchronisation with GNSS antennas for application in autonomous astroparticle physics detectors*. DPG SMuK 2023. URL: <https://www.dpg-verhandlungen.de/year/2023/conference/smuK/part/t/session/145/contribution/6>.
- [54] N. Siegmund. *Zeitsynchronisation im Nanosekundenbereich mit GNSS-Antennen zur Anwendung in autonomen Astroteilchenphysik-Detektoren*. Bachelor Thesis, University Siegen. 2023. URL: <https://www.hep.physik.uni-siegen.de/pubs/bachelor/siegmund-bachelor.pdf>.

- [55] R. Brun and F. Rademakers. “ROOT – An object oriented data analysis framework”. Version v5.34/38 from 12/03/2018. In: *Nuclear instruments and methods in physics research section A: accelerators, spectrometers, detectors and associated equipment* 389.1-2 (Sept. 1997), pp. 81–86. DOI: 10.1016/S0168-9002(97)00048-X. URL: <https://root.cern/releases/release-53438/>.
- [56] S. Argirò et al. “The offline software framework of the Pierre Auger Observatory”. In: *Nuclear Instruments and Methods in Physics Research Section A: Accelerators, Spectrometers, Detectors and Associated Equipment* 580.3 (Oct. 2007), pp. 1485–1496. DOI: 10.1016/j.nima.2007.07.010. URL: <https://doi.org/10.1016%2Fj.nima.2007.07.010>.
- [57] P. Abreu et al. “Advanced Functionality for Radio Analysis in the Offline Software Framework of the Pierre Auger Observatory”. In: *Nucl. Instrum. Meth. A* 635 (2011), pp. 92–102. DOI: 10.1016/j.nima.2011.01.049. arXiv: 1101.4473 [astro-ph.IM].
- [58] National Oceanic and Atmospheric Administration (NOAA). *International Geomagnetic Reference Field (IGRF) 13 Calculator*. [online]. [Last access: 12.09.2023]. URL: <https://www.ngdc.noaa.gov/geomag/calculators/magcalc.shtml?useFullSite=true>.
- [59] P. Alken et al. “International geomagnetic reference field: the thirteenth generation”. In: *Earth, Planets and Space* 73.1 (2021), pp. 1–25. DOI: 10.1186/s40623-020-01288-x.